Technische Universität Dresden

Fakultät Naturwissenschaften und Mathematik

Institut für Angewandte Photophysik

Architectural Approaches for the Absorption Layer and their Impact on Organic Solar Cells

Dissertation
zur Erlangung des akademischen Grades
Doktor der Naturwissenschaften
(Dr. rer. nat.)

vorgelegt von
Beatrice Beyer
geboren am 13. Juni 1984 in Ilmenau

Dresden 2013

Eingereicht am 05.09.2013
Verteidigt am 13.12.2013

Erstgutachter: Prof. Dr. Karl Leo
Zweitgutachter: Prof. Dr. Dieter Wöhrle

Abstract

This study focuses on the architectural modification of pin-type small-molecule organic solar cells, in particular on the absorption layer and its influence on the key solar cell parameters, such as short circuit current density, fill factor and open circuit voltage. Three different approaches have been applied to improve the match between the solar spectrum and the spectral sensitivity of organic solar cells.

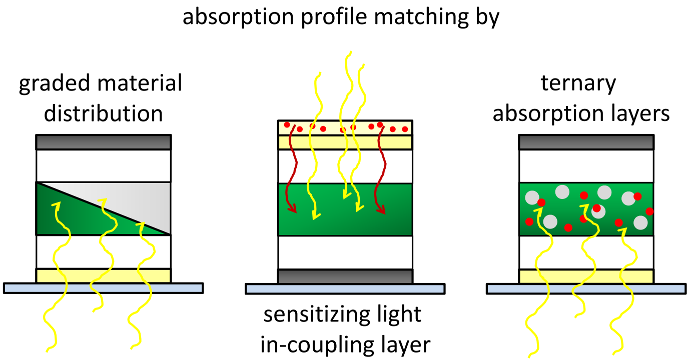

In the first part, deposition parameters such as substrate temperature, gradient strength and (graded) absorption layer thickness are evaluated and compared to organic solar cells with homogeneously deposited absorption layers. Moreover, the gradient-like distribution of the absorption layer is characterized optically and morphological effects have been extensively studied. In order to isolate the origin of the efficiency improvement due to the graded architecture, voltage-dependent spectral response measurements have been performed and gave new insights.

The second part concentrates on the efficient in-coupling of converted UV light, which is usually lost because of the cut off properties of organic light in-coupling layers. Via Förster resonance energy transfer, the absorbed UV light is re-emitted as red light and contributes significantly to higher short circuit current densities. The correlation between doping concentration, simple stack architecture modifications and the performance improvement is duly presented.

In the third and last part, the impact of tri-component bulk heterojunction absorption layers is investigated, as these have potential offers to broaden the sensitivity spectrum of organic solar cells without chemical modification of designated absorber molecules. Along with the possibility to easily increase the photocurrent, an interesting behavior of the open circuit voltage has been observed.

Knowledge about the impact of slight modifications within the solar stack architecture is important in order to be able to improve the device efficiency for the production of cheap and clean energy.

Kurzfassung

In dieser Arbeit wird der Schwerpunkt auf die strukturelle Anpassung des Schichtstapels von pin-artigen organischen Solarzellen auf Basis kleiner Moleküle gesetzt, im Besonderen dessen Auswirkungen auf die Solarzellenparameter wie die Kurzschlussstromdichte, Füllfaktor and Leerlaufspannung. Drei unterschiedliche Ansätze wurden hierbei verfolgt, um den Überlapp zwischen spektraler Empfindlichkeit der Zelle und dem Sonnenspektrum zu vergrößern.

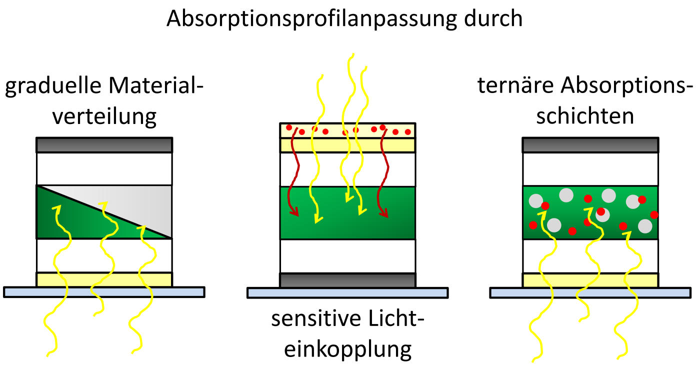

Im ersten Teil werden Beschichtungsbedingungen wie Substrattemperatur, Gradiententiefe und die Dicke der (graduellen) Absorptionsschicht untersucht und mit Referenzproben mit homogener Materialverteilung verglichen. Darüber hinaus wurde diese Verteilung optisch charakterisiert und Effekte auf die morphologischen Eigenschaften ausgiebig untersucht. Um den Ursprung der daraus resultierenden Effizienzsteigerung isolieren zu können, wurden spannungsabhängige spektrale Empfindlichkeitsmessungen durchgeführt, die neue Einblicke in die Thematik erlauben. Der zweite Teil widmet sich der effizienten Einkopplung von umgewandeltem UV-Licht, welches gewöhnlicherweise aufgrund der optischen Eigenschaften von organischen Materialien weggefiltert wird und damit der Energiegewinnung verloren geht. Über den Förster Resonanzenergietransfer wurde das abgetrennte UV-Licht als rotes Licht wieder freigegeben, so dass ein signifikanter Beitrag zur Kurzschlussstromsteigerung erzielt werden konnte. Der Zusammenhang zwischen Dotierkonzentration, einfacher Schichtstapelanpassung und der Effizienzsteigerung wird ausgiebig präsentiert. Im dritten Teil werden die Auswirkungen von dreikomponentigen, mischphasigen Absorptionsschichten untersucht, da dieser Ansatz die Erweiterung der spektralen Empfindlichkeit einfach ermöglicht ohne die Absorbermaterialien chemisch modifizieren zu müssen. Darüer hinaus wurde ein interessantes Verhalten der Leerlaufspannung beobachtet.

Die Kenntnis über die Auswirkungen kleiner Schichtstapelveränderungen ist wichtig, um die Solarzelleneffizienz weiter zu erhöhen, welches die Grundlage für die Produktion von sauberer und billiger Energie darstellt.

Contents

List of abbreviations

α	absorption coefficient
ϵ	extinction coefficient
ϵ_r	dielectric constant
η	power conversion efficiency
λ	wavelength
μ	charge carrier mobility
ν	frequency
π	double bond or constant (3.1416)
ρ	charge carrier density
σ	single bond or conductivity
τ	relaxation time, life time
ϑ	degree celcius-temperature
E_g	energy gap
E	electric field
e	elementary charge
FF	fill factor
I_{SC}	short circuit current
J_{SC}	short circuit current density
J_S	saturation current density
k_B	Boltzmann constant
k	absorption constant, rate constant
L_A	absorption / attenuation length
L_D	diffusion length
n	refractive index or diode ideality factor
P_{inc}	incident power conversion efficiency
R_P	shunt resistance
R_S	series resistance
S	saturation
T_g	glass transition temperature
T	Kelvin-temperature
V_{OC}	open circuit voltage
A	(electron) acceptor

AL	absorption layer
Alq$_3$	*tris*(quinolinato)aluminium
B	ambipolar material
BHJ	bulk heterojunction
BPAPF	9,9-*bis*4-[di-(p-biphenyl)aminophenyl]fluorine
C6	3-(2'-benzothiazolyl)-7-diethylaminocoumarin (coumarin 6)
CT	charge-transfer
CuPc	copper phthalocyanine
D	diffusion constant, (electron) donor
DCM	4-(dicyanomethylene)-2-methyl-6-(*p*-dimethylaminostyryl)-4*H*-pyran
DCV5T	α, α'-*bis*(2,2 dicyanovinyl)-quinoquethiophene
DFT	density function theory
DSSC	dye-sensitized solar cell
EBL	exciton blocking layer
EET	electronic energy transfer
ETL	electron transporting layer
FRET	Förster resonance energy transfer
FWHM	full width at half maximum
HJ	heterojunction
HOMO	highest occupied molecular orbital
HTL	hole transporting layer
IC	internal conversion
INL	injection layer
ISC	intersystem crossing
LIL	light-incoupling layer
LUMO	lowest occupied molecular orbital
MEH-PPV	*poly*[2-methoxy-5-(2-ethylhexyloxy)-1,4-phenylenevinylene]
MeO-TPD	*N,N,N',N'*-tetrakis(4-methoxyphenyl)-benzidine
MLCT	metal-to-ligand charge transfer
MSE	mean squared error
MW	microwave
NA	not available
NPB	4,4'-bis[*N*-(1-naphthyl)-*N*-phenylamino]biphenyl
OFET	organic field-effect transistor
OLED	organic light-emitting diode
OSC	organic solar cell
P3HT	poly(3-hexylthiophene-2,5-diyl)
PCBM	[6,6]-phenyl-C$_{61}$ butyric acid methyl ester
PHJ	planar heterojunction

ppm	parts per million
PTCBi	3,4,9,10-perylenetetracarboxylic bisbenzimidazole
RET	resonance energy transfer
rt	room temperature
S	singlet
SCLC	space-charge limited current
spiro-TTB	2,2',7,7'-tetra(m-tolyl-phenylamino)-9,9'-spiro-bifluorene
SR	spectral response
T	triplet
TOF	time of flight
UV	ultraviolet light
vis	visible
ZnPc	zinc phthalocyanine

Chapter 1

Introduction

In March 1999, the balloonists Bertrand Piccard and Brian Jones started from Switzerland for one of the last and greatest adventures of the world - the first uninterrupted circumnavigation of the world with a balloon. After exactly 19 days, 21 hours and 47 minutes they successfully landed in Egypt.

Even though they did not fully realize during this undertaking, the project was very close to failure - the remaining propane could have only served to keep the balloon in the air for a few hours more.[1] After the first excitement was over, Bertrand Piccard became aware of his strong and all mankind's dependence on fossil fuels and he envisioned the challange to fly around the world only powered by solar energy: the project idea *'Solar Impulse'* was born. By using around 12,000 silicon-based solar cells covering an area of 200 m^2, global circumnavigation with an aircraft is envisaged in a few years. Even though its realization is incomplete, the idea has already inspired millions of humans to face the global energy problem. One approach will without any doubt be solar power conversion, which also motivates this thesis.

The photovoltaic effect can be tracked back to Becquerel in 1839 and has been studied since then for a variety of materials.[4] In modern times, the break-through

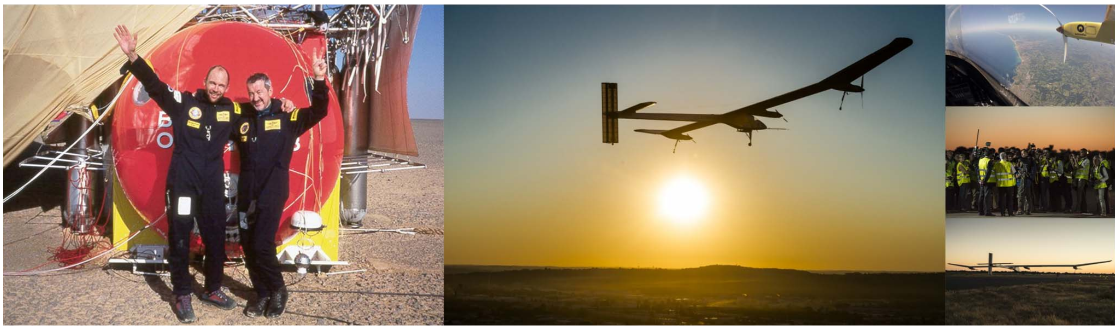

Figure 1.1: Bertrand Piccard and Brian Jones after their successful circumnavigation of the world with a ballon in 1999. The limitation of fossil fuels initiated the present project *Solar Impulse* running since 2003. The images are taken from references[2,3].

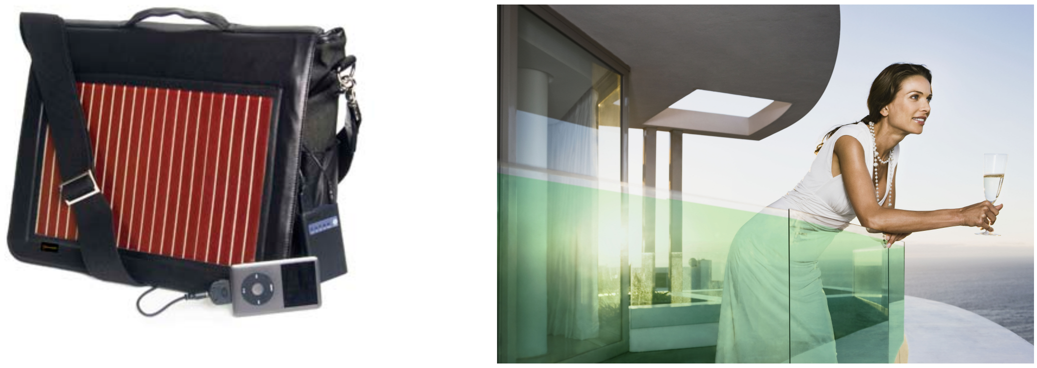

(a) (b)

Figure 1.2: Flexible organic solar modules from Konarka integrated in a bag (a) and semitransparent organic solar cells that can be used for cladding of buildings (b), as proposed by Heliatek.

that transformed photovoltaics to a serious energy sourcing technology was reported by Chapin *et al.* with a silicon based single p-n junction device achieving a power conversion efficiency of 6%.[4] Initially used as a long-term power source for geostationary satellites, photovoltaic cells have gained in efficiency and have entered the consumer market.[4]

At the present time, solar technologies are dominated by wafer-size single junction solar cells based on crystalline silicon mounted into large area modules. Since a further cost reduction is necessary for the routine large-scale production of electricity, much effort has been invested in increasing the power conversion efficiency, the reduction of the absorber material amount and the lowering of the assembly cost of modules. Thin-film photovoltaic technologies, also known as second-generation photovoltaics, are based on inorganic semiconductor materials which absorb more strongly than silicon and can be processed on large area substrates. Such semiconductors include amorphous silicon, II-VI semiconductors and chalcogenides. Simultaneously, over the past two decades, the science and engineering technology of organic semiconductors have progressed rapidly, leading to a diversity of efficient organic based solid-state devices such as organic light emitting diodes (OLEDs), organic field-effect transistors (OFETs), organic photodetectors (OPDs) and solar cells (OSCs).

The possibility of low-temperature processing of either organic small molecules *via* vapor phase deposition or polymers from solution gives organic semiconductors an essential advantage over their inorganic analogs, since the high-temperature processing requirements of the latter exclude the utilization of flexible plastic substrates enabling highly flexible form factors and light weight. It is estimated that modules on plastic foil will not exceed 0.5 to 0.7 kg/m^2.[5]

Furthermore, low-temperature processing reduces the energy consumption during manufacturing and reduces further the energy payback time[1]. Currently, energy payback times of 3 months are reachable, but a decrease towards one day is possible with further efficiency improvements and mass production.[6] Another significant aspect is the low angle-dependency of organic photovoltaics. For example, changing the angle of the incident light up to 60° has almost no influence on solar cell performance. Just the short circuit current density decreases by 2.5% as described by Dennler and co-workers.[7]

Furthermore, organic solar cells exhibit better performance at low illumination intensities or at higher temperatures. Examples where organic solar cells show extraordinary efficiencies even at illumination intensities of 3 $\mathrm{mWcm^{-2}}$ have been published.[8] Additionally, because of the improvement of the charge carrier mobility at higher temperature, the loss in the open circuit voltage can be compensated with the increasing fill factor and the rising short circuit current.[8,9] Modules fabricated by the company Konarka have been specified with a maximum power increase of 0.05%/°C.[5] These features, combined with the possibility to tune the physical properties of organic molecules by adjusting their chemical structure, and low-cost production have boosted the interest both in academia and in industry.[10]

Photovoltaic cells are optimized for maximum electrical power generation under standard illumination conditions (AM1.5 spectral illumination). The power conversion efficiency depends on the following parameters:

- the current density under zero bias, the short-circuit current density J_{SC}
- the photovoltage under open circuit conditions, the open circuit voltage V_{OC}
- the fill factor FF, which characterizes the shape of the J-V curve in the power-generating fourth quadrant.

Organic-based approaches and those that do not rely on conventional single p-n junction are often called third-generation technologies. They include:[10,11]

- the dye-sensitized solar cells invented by Grätzel which are electrochemical cells that mimic the light harvesting complex of photosynthesis
- multijunction cells fabricated from group IV and III-V semiconductors
- hybrid approaches in which inorganic quantum dots are doped into a semiconducting polymer matrix or the combination of nanostructured inorganic semiconductors (*e.g.* TiO_2) with organic materials
- all-organic solid state approaches.

---

[1] defined as the operating time of a power-generating device needed to produce the amount of energy invested during fabrication, installation and maintenance.

This thesis will focus on the latter approach, in particular fabrication using organic optoelectronic molecular solids.

The aim of this thesis is to contribute to this exciting field with regard to the stack architecture of organic solar cells, in particular in terms of the absorption layer which is the active layer where the relevant photophysical processes occur that define the efficiency of a solar cell. The chapter 2 *Fundamentals and Theories* gives an overview of the photophysical principles of organic semiconductors, especially for their utilization in organic photovoltaics. Afterwards, theories will be presented to explain the working principles of these devices. In chapter 3 *Gradient C_{60}-ZnPc Absorption Layers in Small Molecule Solar Cells*, the vertical blend composition of the absorption layer is gradually modified. It will be shown that both optical and electrical effects improve the solar cell performance. After the absorption layer architecture has been addressed, two concepts have been proven in chapter 4 *Flourescent Emitters and their Application in OSCs* to integrate highly efficient fluorescence emitters. For the first approach, a fluorescent emitter will act as classical electron donor material in the D:A blend and for the second one as sensitizer molecule in the light incoupling layer of top-absorbing solar cells. In order to further broaden the spectral sensitivity of organic solar cells, the concept of tri-component absorption layers will be investigated in chapter 5 *Organic Solar Cells with Ternary Absorption Layers* for various aspects such as energy level mismatch, morphology effects and optical behavior. Summarizing, the *Conclusions* of this thesis are drawn in chapter 6. The method, materials and instrumentation used for the execution of this thesis are presented in chapter 7 *Materials and Instrumentation*.

Chapter 2

Fundamentals and Theories

2.1 Materials and Device Structure

2.1.1 Organic semiconductors

While 24 million organic molecules have already been isolated and characterized in the last two hundred years,[12] less than a thousandth of them have been investigated for organic semiconductor applications. Depending on the function of the material, it has to be characterized by either a high luminescent quantum efficiency, high absorption strength, good capability for charge carrier injection, high electron and/ or hole transport conductivity, appropriate morphology properties or several of them at the same time. Independently of their use, all these organic semiconductors have in common that they are formed by aromatic hydrocarbon compounds with alternating single and double bonds between the (mostly carbon) atoms.

Carbon possesses four valence electrons to bond with other atoms, resulting in a tremendous variety of complex molecular structures. The molecular structure is defined by a backbone along which the carbon (or sequentially nitrogen, sulfur, phosphor, oxygen) atoms are sp^2-hybridized to form three σ-bonds. Additionally, these carbon atoms possess p$_z$-orbitals, which are perpendicular to the plane spanned by the sp^2-orbitals and form the so-called π-bonds. This results in electron clouds above and below the molecular plane. The overlap of these π-orbitals determines the formation of delocalized π molecular orbitals, which define the frontier electronic levels, such as the highest occupied molecular orbital (HOMO) and the lowest unoccupied molecular orbital (LUMO). They have an enormous impact on the optical and electrical properties of the molecules. The HOMO and LUMO level are separated by an energy gap typically between one and three eV, which makes these materials to semiconductors. A transition between these two levels can be induced by illumination with visible to UV light, making them very interesting candidates for photovoltaic applications.[13] The HOMO and LUMO level

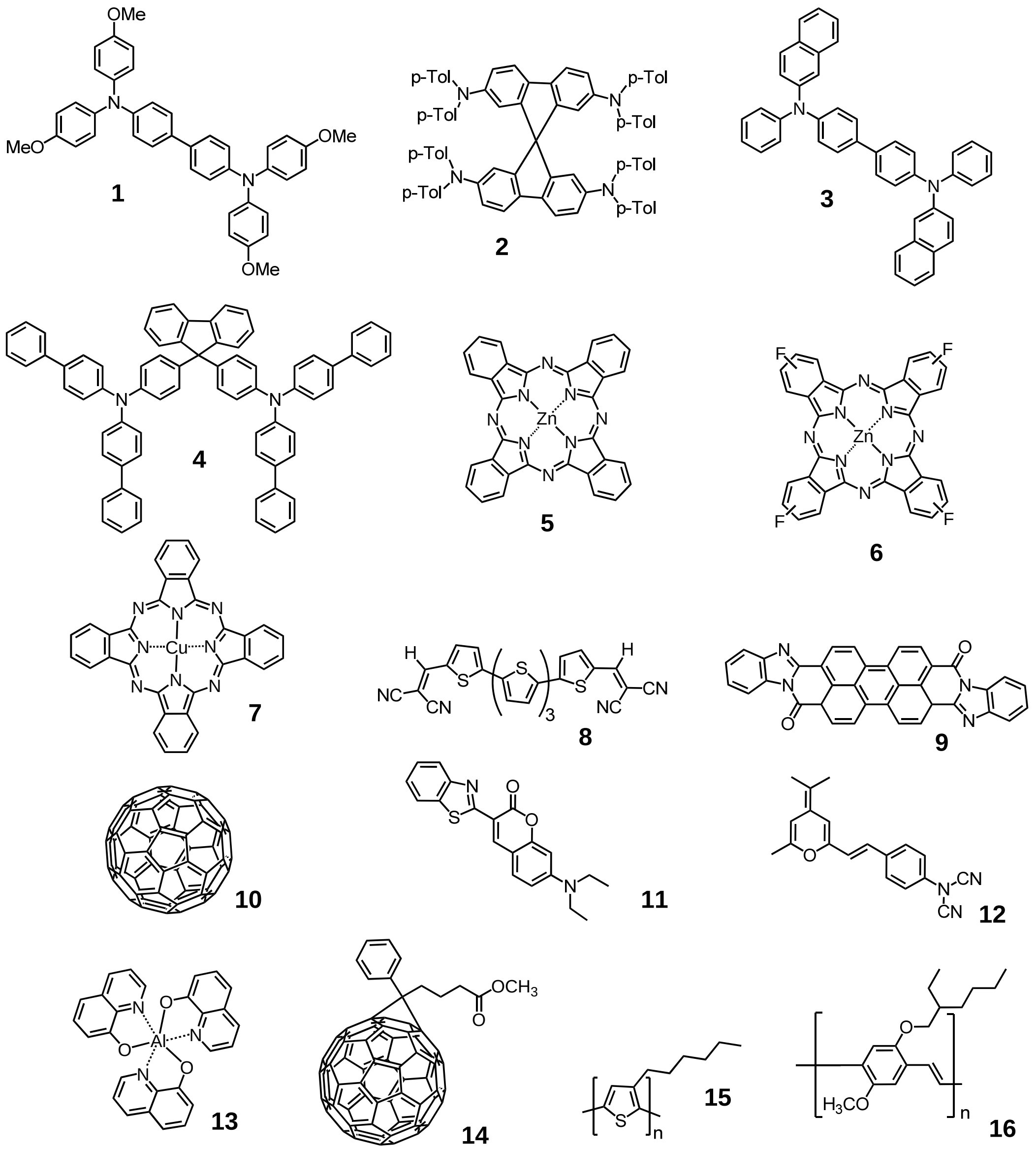

Figure 2.1: Chemical structures of various organic semiconductor compounds. The names of the compounds are given in table 2.1.

can be considered as analogs to the valence or conduction band, respectively of classical inorganic semiconductors. When an organic solid is formed, the molecules interact only by weak van der Waals forces resulting in narrow intermolecular band widths of <0.1 eV for ordered systems. Thus, for disordered molecules the HOMO and LUMO is completely localized on the individual molecules.[14] Because of this circumstance, the electronic structure of an organic solid can be described by the single molecule itself.

Table 2.1 gives an overview of selected organic semiconductors. Their corresponding chemical structures are presented in figure 2.1. Most of them play also a major role in this thesis and the following paragraphs will be used to present them in more detail.

Table 2.1: Overview of several typical molecules used for organic electronics.

name	abbreviation	structure	usage	HOMO / eV	LUMO / eV
N,N,N',N'-tetrakis(4-methoxyphenyl)-benzidine	MeO-TPD	1	hole transporter	5.1 [15,16]	1.85 ± 0.5 [16]
2,2',7,7'-tetra(m-tolyl-phenylamino)-9,9'-spiro-bifluorene	spiro-TTB	2	hole transporter	5.1 ± 0.2 [17,18]	NA
4,4'-bis[N-(1-naphthyl)-N-phenylamino]biphenyl	NPB	3	hole transporter	5.35 ± 0.25 [15,16]	1.95 ± 0.25 [19]
9,9-bis4-[di-(p-biphenyl)aminophenyl]fluorene	BPAPF	4	hole transporter	5.6 [15]	2.2
zinc phthalocyanine	ZnPc	5	donor	5.1 ± 0.1 [15,20–22]	3.6 ± 0.3 [20–22]
meta-tetrafluoro zinc phthalocyanine	ZnF_4Pc	6	donor		
copper phthalocyanine	CuPc	7	donor	5.3 ± 0.1 [19,20,23–25]	3.5 ± 0.3 [20,26]
α,α'-bis(2,2 dicyanovinyl)-quinoquethiophene	DCV5T	8	donor	5.3 [27]	3.4 [27]
3,4,9,10-perylenetetracarboxylic bisbenzimidazole	PTCBi	9	acceptor	6.2 [19,28–30]	4.0 ± 0.6 [19,28,29]
fullerene C_{60}	C_{60}	10	acceptor	6.25 ± 0.15 [16,22,31]	4.0 ± 0.4 [16,22,31–33]
3-(2'-benzothiazolyl)-7-diethylaminocoumarin	C6	11	emitter, donor	5.4 [22,34]	2.9 ± 0.3 [22,34]
4-(dicyanomethylene)-2-methyl-6-(*p*-dimethylaminostyryl)-4*H*-pyran	DCM	12	emitter, donor	5.5 [22,35]	3.2 ± 0.3 [22,35]
trisquinolinatoaluminium	Alq_3	13	electron transporter	6.0 [36]	3.3 [36]
[6,6]-phenyl-C_{61} butyric acid methyl ester	PCBM	14	acceptor	6.1 [37]	4.3 [38]
poly(3-hexylthiophene-2,5-diyl)	P3HT	15	donor	5.1 [38]	3.0 [37]
poly[2-methoxy-5-(2-ethylhexyloxy)-1,4-phenylenevinylene]	MEH-PPV	16	donor	5.1 [39]	2.9 [39]

Hole Transport Materials

This material class consists mainly of aminoaryl derivatives, which are typically transparent in the visible spectrum. Because of spherical repulsion and freely rotatable σ-bonds, these compounds are often non-planar. Hence, they often form amorphous glassy films, which have already successfully been applied for OLEDs, since they form smooth layers and do not degrade as long as they are kept below the glass transition temperature (T_g).[40] In order to prevent unwanted crystallization during storage, experience shows that T_g should be higher than 100 ℃.

Zinc Phthalocyanines

Planar molecules such as zinc phthalocyanine[1] (ZnPc), which is an aromatic macrocyclic compound, are known to crystallize in various structural forms (polymorphs). Depending on the preparation conditions, ZnPc films have been reported with different lattice structures and hence, morphologies resulting in several modifications such as α-ZnPc, β-ZnPc and more.[41] It has been reported that ZnPc films with a thickness greater than 250 nm start to crystallize, and phase transformations to the more stable β-modification can be induced at higher substrate temperatures.[42]

Although it is hard to achieve crystalline ZnPc grains in C_{60}:ZnPc blends, the ZnPc macrocycle consists of four isoindole units which enables a two-dimensional conjugated 18-π electron system. Due to the planarity, the π orbitals can overlap allowing the formation of larger aggregates. The packing has a direct influence on the intermolecular coupling of transition dipoles and can be probed by optical transmission spectroscopy. This allows the analysis of the microstructure by determining the intensities of the Q and Q^+ bands.[43]

It has been shown in the literature that direct fluorination of the macrocycle shifts the HOMO and LUMO levels to lower energies, however, the energy gap is not modified resulting in similar optical constants. With respect to electrical conductivity it has been reported that F_4ZnPc (3.3×10^{-5} Scm^{-1}, 50 nm) possesses better characteristics after a ripening has occured, compared to the non-fluorinated analog ZnPc (1.0×10^{-6} Scm^{-1}, 50 nm).[43]

Fullerene C_{60}

Structurally similar to a football, the molecular group which has been named after the US-American architect Buckminster Fuller represents the third allotrope of carbon. C_{60} as their most famous representative was discovered in 1985 by Kroto *et al.*[44] and has been used in various fields since it can be fabricated in larger amounts (since around 1990[45]). The spherical molecule has a diameter of approximately

---

[1] zinc tetrabenzotatraazaporphyrine.

7.1 Å and in the pure solid an inter-molecular distance of 10.02 Å.[46].

All carbon atoms are sp^2 hybridized, that is the whole inner and outer surface is covered by a delocalized π system. Furthermore, C_{60} has a very strong electron affinity and is used as powerful electron acceptor since it is able to gather at least six electrons.[47,48] The pure material has a low conductivity with 10^{-7} Scm^{-1}, but can be dramatically enhanced by n-doping. The molecule absorbs predominantly in the UV to blue region of light and thus its use as an absorber material is limited.

2.1.2 Device Architectures and Fabrication

A characteristic property used to classify OSC is the molecule size used for their fabrication. Conductive polymers, such as P3HT, MEH-PPV or PEDOT:PSS[2] are typical polymeric materials for organic electronics and are applied by wet-processing techniques such as spin-coating, inkjet printing, screen printing or rotogravure printing. The so-called small molecules comprise all molecules, which can be vaporized before they degrade. A definition by the molecule size is often undetermined, though oligomers such as DCV5T with a molecular mass of 474.55 $gmol^{-1}$ can still be deposited by high-vacuum technology while having high molecular weights.

Due to the poor solubility of common small molecules, they are either fabricated by vacuum based technologies or are modified by alkyl-side chains in order to facilitate the solvation process. Vacuum-based techniques enable defined layer architectures, allow the use of materials in high purity grades and exclude any influence of water or oxygen in the device during fabrication. On the other hand, high vacuum technology needs additional energy due to pumping and an evaporator heating system. Solution based processes are mainly carried out at room temperature, thus the costs at lab scale are very low. For mass production conditions, however, solvents must be recycled and substrates must be cured, which also leads to significant energy consumption. Solvent-free deposition also facilitates the fabrication of multiple layers, because previously deposited films are not affected by the deposition of subsequent layers.

Another classifiaction category represents the device architecture. The field of OPVs can be separated into planar-heterojunction (PHJ) and bulk-heterojunction (BHJ) devices (*cf.* figure 2.2 a). In the former case, the electron donor (D) and electron acceptor (A) materials are deposited one after another[3]. In the latter case, two organic materials are deposited as a single layer[4], either applied as a two component solution or via co-deposition of two materials. The advantage of the BHJ structure is the large size of the interfacial area allowing most of the generated

---

[2] poly(3,4-ethylenedioxythiophene) poly(styrenesulfonate).

[3] hereafter this will be expressed as D/A.

[4] hereafter this will be indicated with D:A.

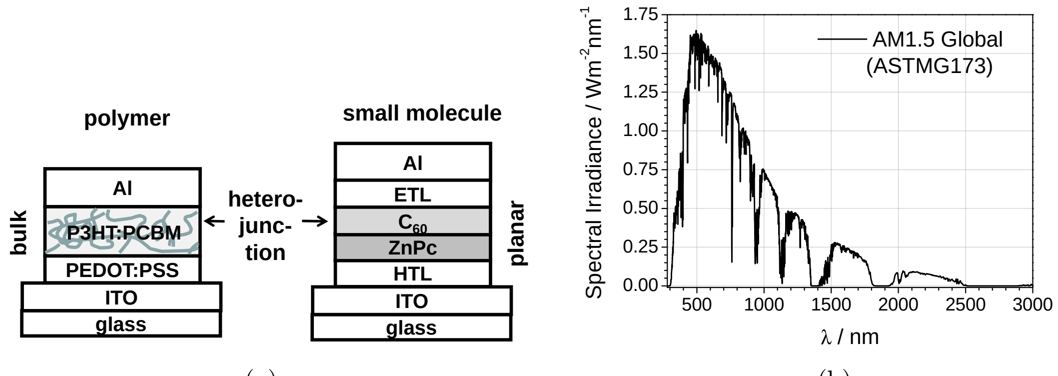

(a) (b)

Figure 2.2: (a) Classification types of organic solar cells. (b) Standard terrestrial solar spectral irradiance distribution of the sun according to the definitions of AM1.5 G[49].

excitons to reach the interface where they can dissociate into free charge carriers. This efficient exciton harvesting can lead to high power conversion efficiencies. However, the performance has been found to be very sensitive to the morphology of the active layer composite. An ideal BHJ active layer is supposed to consist of a bi-continuous interpenetrating network of the components D and A with a maximum interfacial area in which the mean domain size should be similar to the exciton diffusion length.

Along with the preparation method of the D/A heterojunction interface architecture, the performance of an OSC is also defined by the surrounding layers such as transport and exciton blocking layers. Since the controlled insertion of dopants in organic semiconductors has been developed in the last years (*vide infra* section 2.2.4), charge carrier transport layers can be applied in the pure or doped form. Whereas undoped transport layers are limited in thickness because of the low charge carrier mobility, doped transport layers could be applied in larger thickness if the parasitic absorption can be neglected. If doped hole transport layers (HTL) and electron transport layers (ETL) exist within the stack, this architecture is called '*pin*'. Another stack concept, the 'mip' architecture, involves only a p-doped transport layer and is also defined by the metal layer.

In order to achieve highly efficient solar modules, the single solar cells (subcell) can be linked together to achieve power conversion over a large area. Depending on the need for high voltages or high currents, the subcells can be connected in parallel or in series. However, this linkage can not only be executed in the plane dimension, it can also be applied vertically. The construction of several single unit cells results in multi-stacked tandem-cells. The serial connection of such sub-units has become the common tandem architecture because it does not require further electrodes on the substrates. Along with the increase in the current, the spectral match with the solar spectrum can be optimized by the appropriate choice of different absorbing materials.[50,51]

2.2 Device Operation

While the physics of inorganic p-n junctions are well understood and solar cell characteristics can be deduced from material parameters and the kind of electrical contacts, the understanding of organic solar cells is far less well developed. A key difference between organic solar cells and their inorganic counterparts is the nature of the optical excited states. After organic materials absorb a photon, an exciton, *i.e.* a strongly Coulombically bound electron-hole pair, is formed. This electrically neutral and spatially localized electron-hole pair is a Frenkel-type exciton with a total spin of zero, which is more strongly bound than the Wannier-Mott exciton in inorganics.[13,52] Weak, non-covalent, van-der-Waals interactions between the molecules, a low intermolecular overlap and thus low dielectric constants for the solid ($\approx$ 3 to 6 for organic solids, 11.7 for Si[53]) lead to high exciton binding energies.[10] These energies are typically large, with around 500 meV or even larger,[13,48,52] and hence, twenty times or more higher than the thermal energy at room temperature (26 meV). This energy has to be overcome to finally separate the excitons for charge generation. Thus, optical absorption does not lead directly to free positive and negative charge carriers. For the generation of a current, the excitons must first dissociate in external electric fields or at specific dissociation sites, such as a heterojuction between an electron donor material and an electron acceptor material, or others.[54] The excitonic character of their optical properties is a special feature of organic semiconductors. This characteristic is the reason why organic solar cells are often referred to as excitonic solar cells.[52,55]

2.2.1 Optical Absorption

Due to the molecular structure of organic compounds their spectra are featured by structured bands. The photophysical processes are schematically summarized in figure 2.3 and can be classified into two groups: radiative and non-radiative ones. The radiative processes comprise the excitation by absorption (10^{-15} s) of a photon (integer spin) keeping the total spin unmodified during transition as well as the luminescent emission. If the total spin is not changing, the radiative decay will be achieved by fluorescence, which is spin-allowed. Hence, this transition occurs very quickly in the range of 10^{-9} to 10^{-7} s. However, in systems with heavy atoms or with a structure far from planarity, *e.g.* metal phthalocyanines or fullerenes, intersystem crossing (ISC) to triplet states can be efficient. Thus, the spin is flipped and the total spin is 1. This process is spin-forbidden and the associated radiative decay, the phosphorescence, takes place over a broad time regime (10^{-6} s

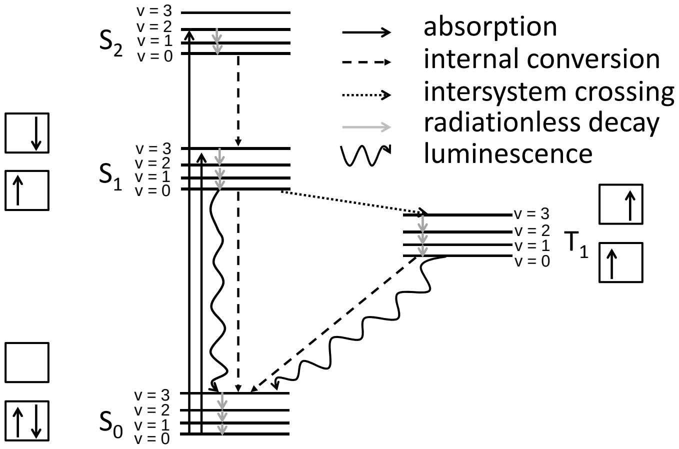

Figure 2.3: Simplified Jablonski diagram for molecules in high dilution comprising absorption, internal conversion, intersystem crossing, radiationless decay and luminescent emission in terms of fluorescence (originating from an excited singlet state S_1 to S_0) and phosphorescence (originating from an excited triplet state T_1 to S_0).

to hours). Since each electronic state is subdivided into several vibronic states (v = 0, 1, 2 ...), because of the very high number of degrees of freedom (3N-6 for non-linear molecules), the absorption and emission spectra are structured into several bands. Because every transition starts from the vibrational ground state (v = 0) reaching it *via* vibrational relaxation (10^{-12} s), all emission processes are lower in energy than the corresponding absorption / excitation transition. Yet, the radiative decay by emission always competes with radiationless decay in terms of internal conversion (IC).

The optical excitation of organic semiconductors is usually realized by $\pi^* \leftarrow \pi$ transitions. The most conjugated solids absorb in the blue and green region of light; absorption in the red or infrared is harder to achieve. Nevertheless, since the absorption bandwidth depends on the degree of conjugation, a wider spectral sensitivity can be obtained in highly conjugated dye molecules.

The absorption bands of organic semiconductors are characterized by strong intensities ($\alpha > 10^5$ cm^{-1})[10,13] due to the large wave-function overlap between the ground state and the lowest excited state.[52] Because of these high absorption coefficients, attenuation lengths[5] L_A of about 100 nm are sufficient to absorb 63% of the incident light. The absorption coefficient α of thin films can be derived from the optical constant k with

$$\alpha = \frac{4\pi k}{\lambda} \tag{2.1}$$

---

[5] defined as the length where the transmission drops to a value of 1/e according to $dT/T = -\alpha \cdot L_A$.

after recording the transmittance and reflectivity of a sample and analyzing its spectra.

The bands are broad because geometry relaxations in the excited states take place, resulting in a possible width of 1 eV.[52] The widths of the absorption bands enable a good match with the solar spectrum, as displayed in figure 2.2. Once promoted to an excited state, the π-system relaxes down to the bottom of the potential energy surface of the lowest excited state reaching its equilibrium geometry, and an exciton is formed. It has to be noted that this relaxation / thermalization process represents a first source of power loss. Due to the geometry relaxation of the exciton associated with its formation, the exciton is often referred as polaron-exciton. In order to seperate this neutral, bound electron-hole pair, a two component system comprising an electron donor and acceptor is required to promote the generation of charge carriers.[55]

Generally, the ground state of the π-conjugated system is a singlet[6] and is denoted by S_0, the lowest excited state by S_1. Pure hydrocarbons with a coplanar conformation possess a negligibly small spin-orbit coupling impeding the population of triplet states. The lowest-energy triplet exciton (T_1) often lies a few tenths of an eV below S_1. At the D/A interface an intermolecular charge transfer leads to charge transfer (CT) states. The hole is located at the donor molecule, the electron at the acceptor molecule. CT_1 is the lowest energy CT state. CT^* represents 'hot' levels of the CT/CS manifolds. The final state is the charge separated state (CS) with free holes and electrons in the donor layer and acceptor layer, respectively. The k_i terms represent various competing relaxation and electron transfer rates. Is has to be mentioned that a simple molecular orbital picture is often used in the literature, derived from HOMO-LUMO diagrams. Herein, the S_0-S_1 transition, S_1-CT_1 transition and E_{final} would correspond to the HOMO(D)-LUMO(D), LUMO(D)-LUMO(A) and HOMO(D)-LUMO(A) energy differences.[13,52] The processes described above are summarized in figure 2.4.

2.2.2 Exciton Diffusion

The generation of separated negative and positive charges makes the diffusion of the excitons to the donor-acceptor interface inevitable, so that they can dissociate. Because excitons are neutral species, their motion is not effected by the electric field. They diffuse *via* random hops. Most importantly, they need to reach the donor/acceptor interface before they decay back to the ground state. Therefore, the exciton diffusion length L_D[7] is supposed to be higher than the thickness of the organic layer providing the D/A interface. Organic semiconductors tend to

---

[6] the total spin multiplicity is zero.

[7] $L_D = \sqrt{D\tau}$, where D is the diffusion coefficient and τ is the exciton lifetime.

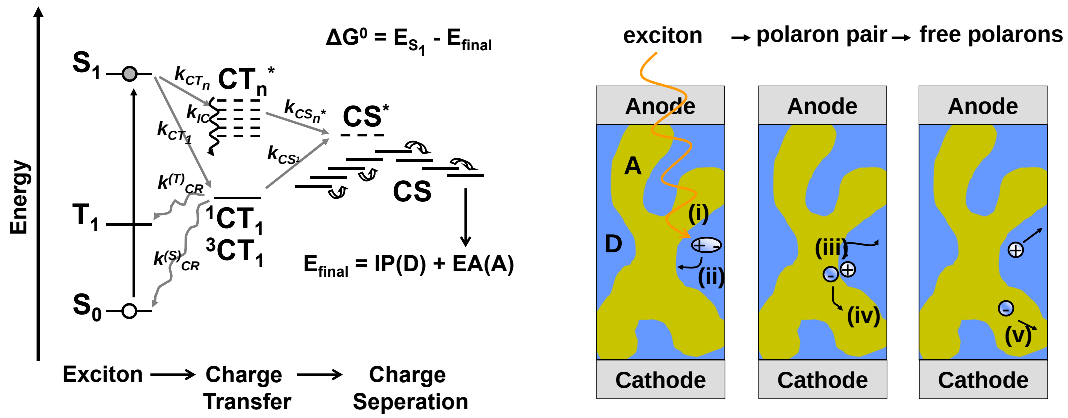

(a)

(b)

Figure 2.4: (a) Electronic state diagram: S_0 corresponds to the singlet ground state, S_1 to the first excited state after optical excitation, CT to a charge transfer state and CS to a charge separated state. (b) Electronic processes within an BHJ organic solar cell: after light absorption (i) singlet excitons are generated, which diffuse to the D/A interface (ii). Although still Coulombically bound, they dissociate *via* an electron transfer (iii). The final separation is realized by the electric field and material disorder (iv) and results in charge transport of the free carriers by hopping toward the electrodes (v). The figure is adapted from reference[13].

have rather small exciton diffusion lengths ($L_D \sim 3$ - 70 nm).[10,13,52] The exciton diffusion length is dependent on two factors: exciton mobility and lifetime.[56] Due to the opposite correlation of efficient exciton diffusion and efficient sunlight absorption with the layer thickness, the optimum has to be investigated. The probability of reaching this interface can be enhanced by establishing an intimate contact between the donor and acceptor materials by blending, codeposition or chemical linking. The main problem of these approaches is the reduction of the charge carrier mobility and the increase of the charge-trap density.[48,57]

One approach to describe the exciton transport in organic semiconductors is the utilization of the generalized Förster resonant energy-transfer (FRET) mechanism, which implicates long-range electrostatic coupling between the excitation dipoles at the initial and final sites.[48] In the case of triplet excitons, hops are restricted to adjacent sites, since they depend on a short-range exchange (Dexter) mechanism.[52] In contrast, singlet excitons can move more quickly (within ns) than triplets (within µs), but they also decay faster. Hence, the diffusion efficiency is very strongly system dependent. The classical Förster approach is based on the interaction of local point dipoles between distant molecules, where the electronic coupling relates to long-range interactions dominated by Coulombic forces (more details about the Förster transfer are given in section 2.4). However, since a short intermolecular separation has been determined between chromophores in a thin film, a more adequate description is necessary.[52] Therefore, the exact nature and contributions of these charge-transfer states are still topics of research.

2.2.3 Exciton Dissociation

At the interface of two different materials, differences in the electron affinity and the ionization potential result in electrostatic forces. If the electron affinity for the electron acceptor and the ionization potential for the electron donor is greater than its counter material, then the interfacial electric field drives the charge separation.[55] Or in other words, if the energy of the excitons is higher than that of charge transfer or charge-separated states, the excitons can dissociate. Charge-separated states will be defined as states where the hole and electron have been completely separated from each other, while in charge-transfer states a Coulombic relation between the charges still exists (for comparison *vide infra* figure 2.4), although the electron and the hole reside already on two separate materials.[13] After generating an excitonic state at the D/A interface, a CT state D^+/A^- is formed, which either recombines to the ground state S_0 or dissociates into free carriers *via* a manifold of CS states. The energy of the final CS state is defined by the (adiabatic) ionization potential (IP) of the donor and the electron affinity (EA) of the acceptor with E_{final} = IP(D) + EA(A).

In most cases, the dissociation process is presented as a transition from the exciton state S_1 to the lowest CT state. In that state, the HOMO level of the donor molecule and the LUMO level of the acceptor molecule are populated with holes or electrons, respectively and they are still Coulombically bound. Hence, the CT state is the lowest in energy. Scenarios such as the presence of disorder in organic semiconductors, dipoles at the interface or the assistance of phonons have been suggested to explain the separation of charges.[13] This relationship is also manifested in the temperature and field dependent photocurrent of organic solar cells which can positively affect the short circuit current and the fill factor.[13]

Mixing techniques increase the area of the D:A interface and ensure that all excitons are formed at a distance from the interface less than the exciton diffusion length. However, the internal field is reduced as well, which is detrimental for V_{OC}.[58] It has been reported that some interfaces between a donor and acceptor are not able to separate excitons into charge-carrier pairs because of the low HOMO offset between these two materials, *e.g.* for α, α'-bis(2,2 dicyanovinyl)-terthiophene (DCV3T) and C_{60} the offset is below 0.6 eV, which is close to the expected exciton binding energy.[59]

Another recently advanced proposition includes the efficient coupling of the exciton to higher lying CT_n states. These states are characterized by a more diffuse shape and can be delocalized over several sites. Therefore, the distance between holes and electrons increases and leads to an easier charge separation. For that scenario, the charge transfer rates k_{CT_n} and the charge separation rates k_{CS_n} have to be higher than the rates of those processes bringing the system down to the CT_1 state.

Depending on the relative time scales of internal conversion (IC) and charge separation processes, two limiting scenarios for exciton dissociation can be considered:

If $\boldsymbol{k}_{IC} \gg \boldsymbol{k}_{CS}$, the CT manifold undergoes a fast relaxation to its lowest electronic/ vibronic state. The lowest D^+/A^- (CT_1) state corresponds to the situation where the hole sits on the HOMO level and the electron on the LUMO level of an adjacent molecule and the charges are still strongly bound. The Coulomb barrier needs to be exceeded for the hole-electron dissociation. Hence, the exciton dissociation *via* this route is less efficient.[52]

In case of $\boldsymbol{k}_{IC} \ll \boldsymbol{k}_{CS}$, the exciton dissociation can be realized *via* excited 'hot' levels of the CT/CS manifolds. This intrinsic charge-carrier photogeneration from higher lying excited states is similar to an auto-ionization process. This pathway has been confirmed by several experimental results. The extremely fast formation of CT/CS states (in 100 fs regime) precludes internal relaxation processes, which are much slower than the aforementioned CT/CS rates. Furthermore, a number of spectroscopic techniques have indicated that CT states formed *via* exciton dissociation (above-gap excitation) reveal lifetimes about two orders of magnitude lower than CT states directly formed from the ground state (sub-gap excitation).[52] Additionally, these sub-gap excitations contribute less to the device photovoltaic response.

2.2.4 Charge Carrier Transport, Mobility and Doping

Charge carrier balancing between electrons and holes is crucial for efficient organic electronic devices. Therefore, the evaluation of the charge carrier mobility is important for the development of semiconductor technology. Various techniques can be used to investigate this property: time-of-flight (TOF), space-charge limited current (SCLC) measurements, or by measuring the field-effect mobility of a thin-film transistor. Time-of-flight (TOF) measurements are widely used for the mobility investigations of organic materials used in OLEDs. For this technique, the transient photocurrent is monitored as charge carriers drift to the charge-collecting electrode under an applied field after illumination by a pulsed laser.[60] Due to the low charge carrier density, the signal is very weak and the signal to noise ratio is poor. Therefore, the required thicknesses are around 2 to 8 µm, which is thicker than used in organic solar cells. Data received from TOF-measurements are thus hardly applicable for device design because of the thickness dependence, although they are by far the most accurate values.

In contrast, SCLC measurements effectively probe the intrinsic properties at a thickness of around 100 nm. Although the SCLC theory has been well established, the mobility analysis of organic semiconductors has rarely been used. This is because a good Ohmic contact (or quasi-ohmic) between the organic layer and the metal electrode is necessary.[60,61] So far, it seems to be rather difficult to explain the current-voltage behavior both at high and low voltages. In PPV devices, it was shown that the conduction of holes at low voltages was limited neither by charge-transfer effects in the bulk nor by the charge injection from the contact.[62] The dependence on thickness by the *J*-*V* characteristics was shown in several cases.[62] In a hole-only device, the work functions of both electrodes are close to the valence band of the materials preventing electron injection from the negatively biased electrode. Since the HOMO and the LUMO offsets between ZnPc and C_{60} are approximately 1 eV, transport of charge carriers in the blend layer should occur along paths consisting of only a single molecular species, *i.e.*, ZnPc for holes and C_{60} for electrons. Therefore, *J*-*V* characteristics for electron- and hole-only devices using SCLC theory[63] can be modeled following the Mott-Gurney law,[64,65]

$$J = \frac{9}{8}\epsilon_r\epsilon_0\mu(F)\theta\frac{V^2}{d^3} \tag{2.2}$$

where $\epsilon_r \approx 3$, the relative dielectric constant of the organic film, ϵ_0 is the permittivity of the free space, $\theta \leq 1$ is the shallow trapping factor[8], d is the distance between the electrodes and *μ(F)* is the charge carrier mobility. For this formula to be valid, the current should by far exceed the 'trap-filled' limit and should follow a $J \propto V^2$ relation. Therefore, the *J*-*V* dependence should regularly be recorded over a wide voltage range. Additionally, the $J \propto d^3$ dependence should be checked before relying on mobility results.[65]

However, the Mott-Gurney law assumes a perfect insulator with an electric field independent mobility, which is not the case for most organic semiconductors. By using the Poole-Frenkel like field dependence of the mobility,[60,61,64] the following equation is obtained:

$$\mu(F) = \mu_0 exp\left[\beta(F)^{\frac{1}{2}}\right]. \tag{2.3}$$

Here, μ_0 denotes the zero field mobility, F is the electric field strength and β is given by

$$\beta = \frac{1}{k_BT}\sqrt{\frac{e^3}{\pi\epsilon_r\epsilon_0}} \tag{2.4}$$

and the combination of equations 2.2-2.4 results in

---

[8] is the ratio of free charge densities to the sum of free and trapped charge densities, in the trap-free limit $\theta = 1$

$$J_{SCLC} = \frac{9}{8}\epsilon_r\epsilon_0\mu_0 exp\left(0.89\beta\sqrt{\frac{V}{d}}\right)\frac{V^2}{d^3}. \tag{2.5}$$

If the electrode contact is capable of injecting sufficient charge to sustain the SCLC given by equation 2.5, the contact is referred to as Ohmic.

After the charges are separated from each other, they drift and diffuse to their corresponding electrodes. This process is both mobility and electric field dependent.[48]

$$\vec{J_i} = e\mu_i\rho_i\vec{F} + eD_i\vec{\nabla}\rho_i \tag{2.6}$$

where e is the elementary charge, μ is the charge carrier mobility, ρ is the charge carrier density, F is the electric field, D is the diffusion constant, and i indicates here the negative or positive charge carriers. Because of a dependence on the morphology of the D/A interface, either the drift or diffusion component might dominate. At PHJ interfaces, the diffusion current is very important and photocurrent is observed even in flat band conditions.[48] At BHJ interfaces on the other hand, the net diffusion current is small and dominated by the drift current.[48] For high power efficiencies an efficient charge carrier transport is crucial as it will be in competition with interfacial recombination processes and thus, will limit the layer thicknesses of the device.

In contrast to inorganic semiconductors, where the strong covalent coupling results in broad valence and conduction bands which ensure a high charge-carrier mobility typically around 10^2-10^3 $cm^2V^{-1}s^{-1}$,[66] the mobility of amorphous organic films is around 10^{-6} to 10^{-3} $cm^2V^{-1}s^{-1}$ and is therefore very low.

The molecular structure of organic semiconductors is defined by a backbone along which the carbon (or nitrogen, sulfur, phosphor, oxygen) atoms are sp^2-hybridized, and thus possess π-atomic orbitals. The overlap of the frontier π molecular orbitals between adjacent molecules characterizes the strength of the intermolecular couplings which represents the key parameter governing charge carrier mobilities. Whereas inorganic semiconductors have high mobilities, the weak electronic coupling of organic semiconductors, the large electron-vibration couplings in π-conjugated materials and the disorder effects inhibit high mobilities. The charges are associated with a local geometry relaxation and hence, move as polarons[9] *via* hopping from molecule to molecule. As a result the charge-carrier mobility strongly depends on the morphology and can, for highly ordered organic crystals, reach mobility values of $>10^4$ $m^2V^{-1}s^{-1}$ (*e.g.* pentacene).[52,54,66] The morphology issue addresses the material properties at the nanoscale (disorder due to variations in

---

[9] In chemical terminology a radical-ion. A polaron is a charge carrier in combination with a distortion of the charge's environment. Because of the flexible matter of organic semiconductors, adjacent molecules can be deformed by the charge carrier.

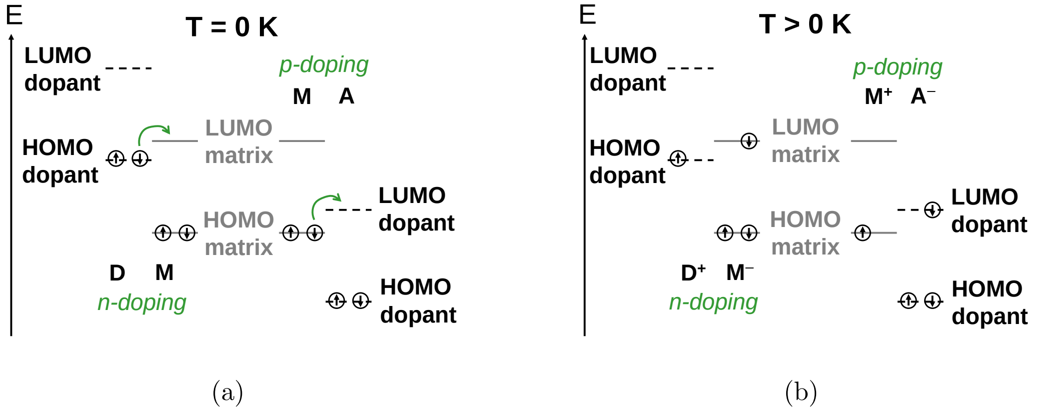

Figure 2.5: Schematic representation of the doping process both for the n- (left) and p-type (right). The population of the energy levels is given for the electron donor (D, n-dopant) and acceptor (A, p-dopant) at 0 K (a) and higher temperatures (b). The arrows in (a) indicate the destination of electrons for (b).

local molecular packing) and mesoscale (disorder because of grain boundaries). Furthermore, π-conjugated materials possess a complex charge-transport regime, where electron-vibration (phonon) coupling and electronic coupling between adjacent molecules are of the same order of magnitude and so both are significant.

As mentioned, depending on the degree of order two extreme cases are possible to describe the transport mechanism: band or hopping transport. Whereas the band transport shows a power law behavior for the temperature dependence, such as

$$\mu \propto T^{-n} \text{ with n} = 1...3, \tag{2.7}$$

the hopping transport implies for the mobility an activated behavior with respect to the temperature and depends also on the applied electric field:

$$\mu(F,T) \propto exp(-\Delta E_A/k_BT) \cdot exp(\beta\sqrt{F}/k_BT) \tag{2.8}$$

i.e., the charge carriers have to overcome an activated energy barrier which is defined by the activation energy E_A and the temperature. In this simple picture, a carrier is initially localized at an energy site i, confined within a deep or shallow potential well. After receiving sufficient thermal energy, the carrier can overcome the potential barrier and hop over to a neighboring site, j. The two different processes that can occur between two localized states are the aforementioned phonon-assisted hopping or direct tunneling. If the electronic wavefunctions of two states overlap effectively, tunneling can take place. Thermally assisted hopping arises when carriers trapped in localized states absorb a phonon. Typically they jump afterwards to the next available site.

Since the conductivity σ is influenced by the state density n and the charge carrier mobility μ,

$$\sigma = \mu \cdot n \cdot e \tag{2.9}$$

the conductivity of pure thin films is not sufficient to fabricate them thicker than 100 nm. The intrinsic carrier density n in a semiconductor is given by

$$n_i = N_0 \cdot exp(-E_g/2k_BT) \tag{2.10}$$

and leads to an hypothetical carrier density of $n_i = 1$ cm^{-3} at room temperature when using $E_g = 2.5$ eV and $N_0 = 10^{21}$ cm^{-3}. The corresponding value for Si would be higher by 10 magnitudes, which demonstrates the extremely low conductivity of organic semiconductors.[67]

(Electrochemical) doping of the transport layer became an inevitable step to overcome the limitations posed by the low intrinsic carrier density. Once high purity organic compounds could be produced, stable and controlled doping could be performed. The introduction of a dopant in transport layers leads to (i) thin space-charge layers at the contacts and consequently efficient tunneling injection despite barriers, and (ii) to lower voltage drops in the transport layers due to their high conductivity. That is, a high-carrier injection level can be achieved without needing to match electrode work functions. The conductivity of doped layers ranges from 10^{-6} to 10^{-4} S/cm, *i.e.* orders of magnitudes higher than those of undoped films ($\leq 10^{-9}$ S/cm).[10,34,40] Because of this high conductivity, the electric field in doped transport layers is relatively low resulting in device operation close to the flat band condition.[66]

The basic principle of doping in organic semiconductors is rather similar to that in inorganic semiconductors. The addition of an impurity is necessary which either transfers an electron to electron conducting states (n-doping) or removes an electron from the hole conducting state (p-doping). The general principle for both types is illustrated in figure 2.5. In order to describe the operation of doped transport layers, energy diagrams are used where the valence and conduction band energies are replaced by the HOMO and LUMO (polaron level), respectively.[67]

Very high conductivities have been realized with phthalocyanines (weak donor character) by exposing them to molecular oxygen or iodine. The drawback of using such small dopants is their size, because it allows an easy diffusion through the layers. Similar considerations are also appropriate for small atoms such as lithium or small Lewis acids.[66] Therefore, larger aromatic molecules which are strong π-acceptors or donors are essential to assure a long lifetime of the device. For the system ZnPc:F_4-TCNQ[10] it has been shown that the conductivity could be increased by more than six orders of magnitude.[66]

---

[10] 7,7,8,8-tetracyano-2,3,5,6-tetrafluoroquinodimethane.

p-doping

Due to the energy level positions p-doped transport layers are more stable in air and so, a lot of investigations have been done on this type of film. For instance, phthalocyanines have been doped with *ortho*-chloranil, TCNQ or dicyano-dichloroquinone (DDQ), ZnPc doped by F_4-TCNQ or oligothiophenes doped by DDQ.[66]

With increasing doping concentration, the Fermi level moves towards the transport states. With increasing temperature on the other hand, it moves towards the center of the band gap. The conductivity increase by doping is for amorphous materials much lower than for polycrystalline compounds because of the stronger localization of the charge carriers.[66]

For efficient p-type doping, it is necessary that the orbital overlap of the acceptor LUMO and matrix HOMO states is effective. The more the charge carriers are localized in the amorphous material, the lower is the conductivity.[66] Moreover, it is stated that p-doping can increase the HTL material's workfunction.[59]

n-doping

For efficient n-doping, the HOMO level of the dopant has to lie higher than the LUMO level of the matrix material. Therefore, most n-dopant materials are unstable against oxygen.

Due to the insertion of another material component in the matrix system, the charge carrier mobility is lowered due to disorder effects. Nevertheless, the charge carrier density increases several orders of magnitude, so that this mobility decline is more than compensated for and the conductivity increases. Additionally, because the hopping transport mechanism is strongly temperature dependent, variations of the solar cell temperature can influence the photocurrent.[55]

2.3 Device Performance and Modeling

In the following section the electrical characteristics of organic solar cells will be reviewed. A schematic presentation of a typical cell's composition is presented in figure 2.6 a. In the dark, solar cells work like diodes. As for conventional p-n solar cells, an organic photovoltaic device can be described by an equivalent circuit diagram, as presented in figure 2.6 b, including:[13]

- a diode with a reverse saturation current density J_0 and an ideality factor n
- a current source J_{ph} corresponding to the photocurrent during illumination
- a series resistance R_S which is supposed to be minimal and accounts for the conductivity of the semiconducting material, the contact resistance between

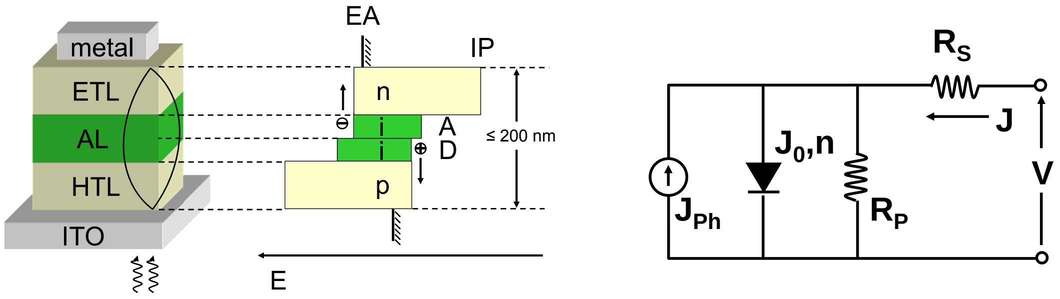

(a) (b)

Figure 2.6: (a) Standard structure of an organic pin-OSC with their respect energy levels including the n-doped electron transport layer, the intrinsic absorption layer consisting of the donor and acceptor material as well as the p-doped hole transport layer. (b) Equivalent circuit diagram for the modelling of solar cells.

the semiconductors and the electrodes (injection barriers), and the sheet resistance correlated to electrodes and interconnections

- a shunt resistance R_P which needs to be maximal and considers the loss of carriers *via* leakage paths including structural defects like pinholes in the film or recombination centers originated from impurities.

The analytical expression for the aforementioned current-voltage characteristics is referred as the Shockley equation:

$$J = \frac{1}{1+\frac{R_S}{R_P}} \left[J_0 \left\{ exp\left(\frac{V - JR_SA}{nk_BT/e} \right) - 1 \right\} - \left(J_{Ph} - \frac{V}{R_PA} \right) \right] \tag{2.11}$$

where e denotes the elementary charge, k_BT the thermal energy, n the diode ideality factor and A the area of the cell. The analysis of equation 2.11 in different regimes of the photocurrent shows that R_S is a critical factor, in particular in regimes of high photocurrent, J_{Ph}. From equation 2.11, expressions for V_{OC} and J_{SC} can be derived:

$$V_{OC} = n\frac{k_BT}{e} ln\left\{ 1 + \frac{J_{Ph}}{J_0}\left(1 - \frac{V_{OC}}{J_{Ph}R_PA} \right) \right\} \approx n\frac{k_BT}{e} ln\left\{ 1 + \frac{J_{Ph}}{J_0} \right\} \tag{2.12}$$

$$J_{SC} = -\frac{1}{1 + R_S/R_P} \left\{ J_{Ph} - J_0 \left(exp\left(\frac{|J_{SC}|\, R_SA}{nk_BT/e} \right) - 1 \right) \right\} \approx -J_{Ph} \tag{2.13}$$

The equations 2.11 - 2.13 normally require a numerical solution, except for the cases where R_S is very small and/ or R_P is sufficiently large enabling the effects occuring from R_S and R_P to be negligible. In these cases the right hand expressions of the equations can be applied. However, apart from non-zero R_S and finite R_P, some common deviations from an ideal diode are observed for organic heterojunctions, such as:

- R_P dependency on light intensity such as $R_P \propto P_0^{-1}$; an increase of free charge carriers in the bulk is suggested to originate from exciton annihilation and its energy transfer to trapped charges or due to photoconductive gain (both processes are exciton density dependent)
- R_S decreases with increasing light intensity resulting in a crossing of the dark and light curve because of the photoconductivity properties of the material
- $n > 2$
- a "kink" in the J-V curve near the open-circuit[48,68]
- a voltage-dependent current.

The current-voltage characteristics of bulk heterojunction organic solar cells, however, can hardly be described by the Shockley equation. The strongly field-dependent photocurrent often does not reach its maximum under short circuit conditions, but at negative bias corresponding to a higher internal field. Furthermore, a crossing point of the dark and illuminated curve is observed which can not be predicted by the diode equation.[13] Applying the Shockley equation to experimental data leads to defining a voltage and light intensity dependent parallel and serial resistance without any physical justification. Hence, organic solar cells are quite different from their inorganic analogs.

Two quantities can easily be determined experimentally under illumination: the intersections between the graph and the vertical and horizontal axes, which correlates to J_{SC} and V_{OC}, as depicted in figure 2.7 a. At any point in the fourth quadrant (J_{SC} is negative, V_{OC} is positive), the cell produces a power density given by the product of the voltage and current density. This product is at one point maximized at V_{max} and J_{max}. The power conversion efficiency η is defined as

$$\eta = \frac{J_{max} V_{max}}{P_{inc}} = FF \frac{J_{SC} V_{OC}}{P_{inc}}, \tag{2.14}$$

where P_{inc} is the incident power density and FF corresponds to the fill factor[11]. The parasitic resistances influence the shape of the current density/ voltage characteristic. Their effects are illustrated in figure 2.7 b. A finite series resistance R_S limits the current in forward bias, while a finite shunt resistance causes a dark current increase in reverse bias.

---

[11] $FF = P_{max}/(J_{SC} \times V_{OC})$.

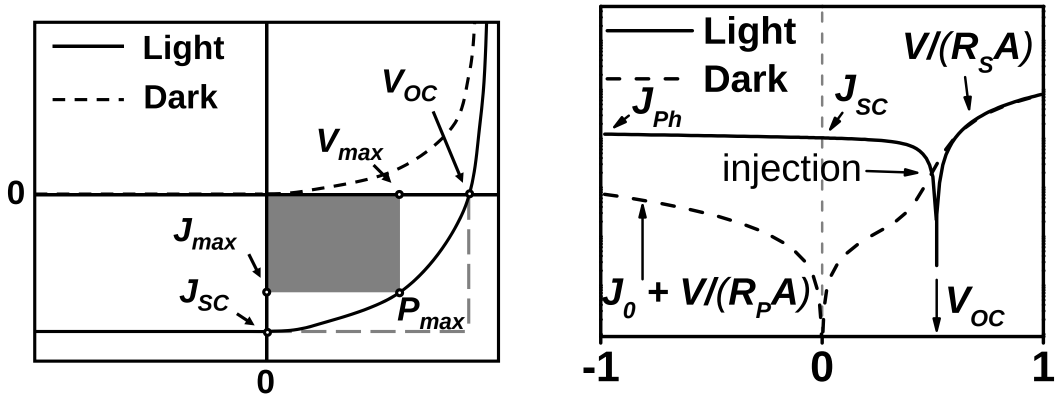

(a) (b)

Figure 2.7: A typical J-V curve of a solar cell in the dark and under illumination in a linear (a) and a logarithmic plot (b).

For the quantitative characterization of the solar cell performance related to terrestrial applications, standardized illumination conditions are used, in which the solar spectrum is simulated (AM1.5G) with an intensity of 100 mWcm^{-2}. Importantly, according to equation 2.14 the power conversion efficiency of a solar cell is determined by three parameters: the fill factor, the short-circuit current density and the open-circuit voltage. In the following sections the limitations of these parameters will be examined together with a discussion of how they relate to material and contact properties.

2.3.1 Fill Factor

The fill factor is given by the quotient of the maximum power efficieny (P_{MPP}) and the product of the short circuit current and the open circuit voltage (*cf.* figure 2.7 a). Thus, the FF describes the quality of the current-voltage characteristic.[13] The maximum fill factor is a function of V_{OC} and the ideality factor n. In organic solar cells with V_{OC} = 0.5 - 1.0 V, the ideality factors are in the range of n = 1.5 - 2.0. Recombination processes are responsible for the reduction of FF, however, little is known about the specific mechanism. It is assumed that the HJ bulk layer can influence the FF in two ways. The first is due to a strong field-dependent exciton dissociation rate. Here, the photocurrent J_{Ph} switches near V_{OC} from the linear to the saturation regime. The J-V curvature tends to become concave. Besides this field-dependency, an unbalanced charge carrier transport plays a major role as well. The S-shape hints at a counter-injecting diode which occurs due to charge carrier accumulation near one of the electrode.[69]

Furthermore, FF is strongly affected by the resistances as shown in equation 2.15.

$$FF(R_S, R_P) \approx FF(0,\infty)\left(1 - \frac{J_{SC}R_S}{V_{OC}} - \frac{V_{OC}}{J_{SC}R_P}\right)^{[10]} \qquad (2.15)$$

R_S increases because of defects at the D/A interface, significant losses from recombination or due to poor conductivity of the molecular film.[48,58] Therefore, it can be lowered by decreasing the film thickness to improve the carrier collection efficiency.

2.3.2 Short-Circuit Current Density

The maximum J_{SC} is given by

$$J_{SC} = \int_{AM1.5} e\eta_{EQE}(\lambda)N_{Ph}(\lambda)d\lambda \tag{2.16}$$

where $N_{Ph}(\lambda)$ is the photon flux density in the incident AM1.5G spectrum at a wavelength λ and a total intensity of 100 mWcm^{-2}. The external quantum efficiency $\eta_{EQE}(\lambda)$ describes how efficiently incident photons give rise to an electron in the external circuit. Assuming an EQE of 1 and an absorption profile (bandgap of around 1.8 eV) which overlaps well with the AM1.5 spectrum, a maximum J_{SC} value of 20 mAcm^{-2} is possible.[48] In organic solar cells, η_{EQE} can be broken down into efficiencies associated with steps which have previously been discussed: absorption, exciton diffusion, exciton dissociation into free carriers, charge transport and charge collection.

- The *photon absorption efficiency* depends on the absorption coefficient α of the absorbing material and where this absorbing layer is located in the organic device since the layer thicknesses range in the coherence length of sun light.

- The *exciton diffusion efficiency* depends on the exciton diffusion length L_D of the corresponding material system.

- The *charge transfer efficiency* is known to be very efficient and requires a proper offset between the LUMO (HOMO) levels for electron (hole) transfer between the donor and acceptor material. This offset must be larger than the exciton binding energy.

- The *dissociation efficiency* of electron-hole pairs which is considered to be the decisive step in an organic solar cell. It is still under extensive discussion whether this process occurs *via* an CT state or hot excitons.

- The *charge transport efficiency* depends on the charge carrier mobility and lifetime, their product should be greater than the distance to layers where it can be extracted.

- The *charge collection efficency* is smaller than 1 if the contacts are not selective and the charge carriers reach the wrong contact resulting in recombination losses.

2.3.3 Open-Circuit Voltage

The physical origin and the accurate description of the open-circuit voltage in organic photodiodes is still challenging. Solar cells consisting of an organic semiconductor between two electrodes have been described with the metal-insulator-metal model (MIM), in which the so-called built-in potential is defined by the difference of the work functions between the cathode and anode. According to the MIM model the V_{OC} is reached when the Fermi levels are balanced to each other. After using donor-acceptor heterojunctions the description of the built-in voltage in the MIM model was modified, *i.e.* the charge carrier separation takes place at the heterojunction inside of the device. The dependence on the incident light intensity of V_{OC}, which was found in bilayer devices, has been explained by including the drift and diffusion current, which have also been considered according to the MIM model. A distinctive dependency on the open circuit voltage with respect to the processing conditions has been found for BHJs, where a three-dimensional interface network is formed by the donor and acceptor material. With variation of the acceptor material, a correlation between the LUMO level of the acceptor material and the V_{OC} has been observed.[70] Here, the term 'Fermi level pinning' has been introduced, where the Fermi level of the semiconductor is adjusted to the work function of the electrode in the thermodynamic equilibrium. In those HJ layers the relationship between the V_{OC} and the work functions of the cathodes is less distinct and can mainly be attributed to non-ohmic contacts between the semiconductor-metal interface rising from transition barriers.

Increasing the device open circuit voltage has been the subject of significant research efforts due to the fact that state of the art C_{60}:ZnPc based PV cells have an $V_{OC} \approx 0.5$ V, although the absorption maximum of the single absorber materials is at photon energies ≥ 2.0 eV. By solving the generalized Shockley equation[12] at $J = 0$ for $V = V_{OC}$, the factors that contribute to V_{OC} can be highlighted as

$$V_{OC} = \frac{nk_BT}{e} ln \left[\frac{J_{ph}(V_{OC})}{J_s} + 1 - \frac{V_{OC}}{J_s R_p} \right]. \tag{2.17}$$

The open circuit voltage is approximated by

$$V_{OC} = \frac{nk_BT}{e} ln \frac{J_{SC}}{J_S} \tag{2.18}$$

---

[12] $J = \frac{R_P}{R_S+R_P} \left[J_s \left\{ exp(\frac{q(V-JR_s)}{nk_BT})/1 \right\} + \frac{V}{R_p}/J_{ph}(V) \right]$.

where n is the diode ideality factor, k_B is the Boltzmann's constant, T is the temperature, e the fundamental charge, J_{SC} is the short circuit current density and J_S is the saturation dark current density.

Assuming η_{EQE} is not a function of the incident light intensity and the product $J_sR_p >> V_{OC}$, then $V_{OC} \propto ln(P_0)$. These conditions are normally satisfied at P_0 less than a few sun intensities.[10] A variety of experimental results suggest that V_{OC} originates from the difference between the HOMO of the donor and the LUMO of the acceptor material as opposed to the work function difference between the metal electrodes. Consequently, there is a consensus that the *maximum* achievable value of V_{OC} is given by

$$qV_{OC} = IP_D - EA_A - \frac{e^2}{4\pi\epsilon_0\epsilon_r r_{DA}} \tag{2.19}$$

where ϵ_0 is the vacuum permittivity, ϵ_r is the relative dielectric constant of the bulk organic layer, and r_{DA} is the initial separation distance of the electron-hole pair, which needs to be fully separated to contribute to photocurrent. The third term on the right-hand side of equation 2.19 is the attractive Coulomb interaction between the charge carriers and corresponds to the binding energy of the dissociated, geminate electron-hole pair created as a result of electron transfer.[71] The linear dependence of the HOMO$_D$-LUMO$_A$ gap on V_{OC} has been observed in several material combinations and is used as a "rule of thumbs".[72] In an ideal solar cell, the splitting between the hole and electron quasi-Fermi levels at the D/A interface equals $e{\cdot}V_{OC}$. Additionally, several examples have been reported where a dependence on the open circuit voltage has been attributed to morphology effects. This has been inferred from the variation of the deposition parameters, such as substrate temperature, velocity of deposition, post-processing steps such as annealing[37] or the modification of the D:A acceptor fraction.[73]

Because of the high number of empirical observations, a generalized equation to describe the origin for all organic solar cells is challenging and is still under development. Recently, a review has been published by Tress and co-workers highlighting the consideration of the charge carrier mobility for the investigation of the V_{OC} behavior.[74] They used drift diffusion simulations to explain various observations found by experiments. For their simulations they assumed for the blended absorption layer an intimate intermixing of the D and A material with closed pathways, so that it can be considered as an effective medium. Furthermore, blending does not result in polarization effects, thus the energy levels are defined by the pristine material properties. Because charge carrier transport in amorphous molecular solids is realized by hopping, the mobility μ can be considered as a relatively macroscopic, effective parameter, which defines the effective charge carrier drift velocity ν by $\nu = \mu E$. The mobility is very important for the charge carrier extraction and represents a competing mechanism to recombination. Generally, the V_{OC} is defined as the quasi-Fermi level splitting that a solar cell can achieve under illumination without load

$$e \cdot V_{OC} = E_g^{DA} - k_B T ln \frac{N_C \cdot N_V}{n \cdot p}. \tag{2.20}$$

Depending on the applied theory, alternative expressions for the product $n{\cdot}p$ result. One loss mechanism is apparent at the D/A interface, which is often referred as bulk recombination. This direct electron-hole recombination R_0 is influenced by the charge carrier densities n (electrons) and p (holes) with

$$R_0 = \beta(np - n_i^2) \tag{2.21}$$

with β as the recombination constant and n_i as the instrinsic charge carrier density. R_0 is also called the bimolecular recombination due to the requirement of two free charges. The Langevin theory on the other hand does not consider β as mobility-independent resulting in the following expression

$$\beta_L = \frac{e(\mu_n + \mu_p)}{\epsilon_0 \cdot \epsilon_r}. \tag{2.22}$$

In experiments with BHJ architecture, often a lower β than predicted has been observed which has been attributed to the circumstance that the free charge carriers need to travel back to the heterointerface before they recombine. So far, no evidence for a mobility dependent Langevin recombination has been found for small molecule based OSC.

Another theory includes the CT state as bound electron-hole pair with a binding energy E_B. Excitons are supposed to pass through this state when they dissociate or as charge carriers when they recombine. Using the effective generation rate G with $G = G_0{\cdot}P$ the effective recombination rate R with $R = R_0(1\text{-}P)$, where P[13] is the probability of dissociation and

$$k_{dis} = \beta e^{-\frac{E_B}{k_B T}} f(E, E_B) \tag{2.23}$$

gives finally

$$e \cdot V_{OC} = E_g^{DA} - k_B T ln \frac{N_C N_V k_{relax}}{G_0 f(E, E_B)} \tag{2.24}$$

which has been also proposed by Kirchartz et al. using a detailed balance approach.[75] This relation shows a mobility independent V_{OC} and connects V_{OC} with the CT energy of the state (E_g^{DA} – E_B). However, this V_{OC} independence of the mobility has been claimed to be incorrect.[74]

---

[13] $P = \frac{k_{dis}}{k_{dis} + k_{relax}}$

Nevertheless, various examples for small molecule based devices show that V_{OC} depends strongly on the cell architecture, such as the planar or bulk heterojunction concept.[15] For BHJ photovoltaics, a relation between the built-in potential and the V_{OC} has been investigated and discussed in detail.[16] Here, the built-in potential $e{\cdot}\mathrm{V}_{bi}$ has been defined as the difference in the work functions of the ITO contact and the p-doped HTL. With variation of the HTL material and therefore, a changing level of the HOMO, the value of V_{OC} can be tuned.

In BHJs the holes and electrons are not spatially separated in the active absorbing material, so that there is no diffusion gradient for photogenerated holes to the anode and electrons to the cathode. For positive electric fields, a large current of injected charges from the electrodes is flowing in forward direction. According to simulated current profiles no hole injection over the barrier is then necessary, because the current throughout the blended layer is dominated by electrons that recombine with holes at the HTL/blend interface.[15]

The difference between BHJ and PHJ originates in principle from the device structure. When preventing the possibility that electrons and holes meet at other interfaces except the D/A interface, the J-V curve of the BHJ devices will show the characteristics of a PHJ diode. This can be achieved by introduction of pure layers of D and A molecules around the blend. On the other hand, experimental data exist where the V_{OC} is independent of the HTL material, but to vary with the doping concentration.[59]

2.3.4 Effect of Temperature on the Electrical Characteristics of Bulk-Heterojunction Solar Cells

Another special property of organic bulk heterojuction solar cells is the temperature dependency of their efficiency which increases with enhancement of the temperature in contrast to inorganic solar cells. The temperature dependence has been attributed to either the temperature dependent mobility or to the steady state charge carrier concentration.[67] Without any mono- or bimolecular recombination, J_{SC} is expected to be almost temperature independent. The influence of the temperature on the J_{SC} can be related to the electronic transport properties of the absorber and transport materials. Riedel *et al.* related the rise with higher temperature to the increased charge carrier mobility which resulted in higher J_{SC}, FF and therefore higher efficiency.[72,76] In the absorber layer the conductivity is very low and charge carrier transport is realized by a hopping mechanism, which is thermally assisted. Accompanied by this, the probability for charge carrier recombination will be higher at low temperature. If a model of monomolecular recombination for photogenerated charges is assumed, the equation 2.25 can be used.[9,10,76]

$$J_{SC}(T) = J_{00} \times exp(-\frac{\Delta}{k_B T}) \tag{2.25}$$

Δ corresponds to the activation energy and can be associated with the energy required to dissociate the bound electron-hole pairs. These pairs are supposed to be involved as an intermediate step between the excitonic state and the free charge carriers. For instance, it was also observed that the positive temperature effect was more significant at higher light intensities. This has been explained by a limitation of the carrier transport due to the low mobility of holes in the donor and electrons in the acceptor molecule, which is more evident than for lower carrier densities at low light intensities. Activation energy values of Δ = 44.7 meV have been reported for PPV:PCBM samples.

In terms of V_{OC}, it shows an inverse linear behavior with for temperatures >200 K with

$$V_{OC} \propto T^{-1}.^{[10]} \tag{2.26}$$

Riedel and coworkers found an optimum temperature of 175 K for their polymer-fullerene[14] solar cell, whereas the V_{OC} was linearly decreasing for high temperatures at higher intensities. The variation of the temperature results in a maximum of this parameter for an illumination intensity of 10.4 mW/cm^2. Katz *et al.* also found a linear correlation for a temperature range from 295 to 333 K for a polymer-fullerene solar cell[15] and determined a temperature coefficient dV_{OC}/dT = –(1.40 to 1.65) mV/K. This dependency has been attributed to the temperature dependence of the quasi-Fermi levels of the components of the active layer under illumination,[9] which has also been pointed out by Thakur et al.[72] Assuming a Gaussian density of states (DOS) of both donor HOMO and acceptor LUMO, manifolds enable the determination of the Fermi level positions from which V_{OC} results proportional to the logarithmic function of the carrier density and the effective energy band gap E_g as

$$qV_{OC} \propto E_g - k_B T ln(\frac{N_n N_p}{np}).^{[72]} \tag{2.27}$$

Regarding the fill factor *FF*, it could be noted that the series resistance R_S decreases with higher temperaure as well, whereas the parallel resistance R_P remaines the same. Therefore, the *FF* increases.

---

[14] OC$_1$C$_{10}$-PPV:PCBM, OC$_1$C$_{10}$-PPV = poly[2-methoxy-5-(3,7-dimethyl octyloxy)-1,4-phenylene vinylene], PCBM = phenyl-C$_{61}$ butyric acid methyl ester.

[15] MDMO-PPV:PCBM, MDMO-PPV = poly[2-methoxy, 5-(3',7'-dimethyl-octyloxy)]-*p*-phenylene-vinylene.

2.3.5 Optical Simulation

The simulation of OPV devices can be separated into two parts: the in-coupling of the light into the multistructure and the extraction of charge carriers. The absorption of light within the multilayer structure is crucial and has therefore given rise to a large field of numerical simulations. OPV cells consist of a multilayer structure with layer thicknesses of the order of the wavelength of sunlight. The materials used have different optical properties causing a mismatch of the refractive index at multiple interfaces, which leads to multiple reflections that produce optical interference effects. Thus, an OPV cell is an optically coherent device. As result, the light distribution inside the solar cell is highly inhomogenous and determined by a complicated interplay of the relative optical constants of the materials and their thicknesses. Nevertheless, this circumstance can be utilized to model the light and steady-state exciton distribution inside of the solar cell and thus, to increase the maximum photocurrent by tuning the thickness of each layer. With the calculation of the electromagnetic field inside the multilayer stack using a transfer matrix formalism, the optimum layer thickness can be determined.[77,78]

In oder to determine the squared amplitude of the optical field penetration profile in an absorbing device, the commercially available simulation software Setfos 3.2 has been used. Here, the field amplitudes and the energy fluxes for each wavelength, at each position within the stack are calculated by using a transfer matrix formalism. With this formalism the normalized optical electric field E_{norm} is evaluated throughout the multilayered stack. For plane waves, the optical field intensity is given by

$$I = \frac{1}{2}\epsilon_0 cn \left|E\right|^2 . \tag{2.28}$$

with the speed of light c, the refractive index n and the electric field E of light. In the transfer matrix formalism the incident electric field is normalized so that the incoming electric field amplitude is 1. Thus, the field strength is given relative to the surrounding medium E_0. Using the ratio

$$\frac{I}{I_0} = \frac{\frac{1}{2}\epsilon_0 cn \left|E\right|^2}{\frac{1}{2}\epsilon_0 cn_0 \left|E_0\right|^2} \tag{2.29}$$

of the illumination intensity I_0 in the surrounding medium and the device internally I,

$$I(z, \lambda) = \frac{n}{n_0} \left|E_{norm}\right|^2 I_0 \tag{2.30}$$

the energy flux can be calculated. This optical field gets partially absorbed and therefore (excitons and) charges are generated. The photon absorption rate profile *G(z)* is calculated for different spectra and the position z inside the device with

$$G(z) = \int_{\lambda} \frac{\alpha(\lambda) I(z, \lambda)}{h \cdot \nu} d\lambda \tag{2.31}$$

where $\alpha(\lambda)$ is the absorption coefficient, which correlates to the complex part of the refractive index k ($\alpha = 4\pi k/\lambda$), λ the wavelength, I the intensity of the illumination source and the photon energy $h\nu$. Furthermore, the intensity inside the stack is referred to the unpolarized light coming from the illumination source. Assuming a 100% exciton generation after photon absorption and dissociation without any losses, I_{SC} can be calculated *via*

$$I_{SC} = \int_{Layer} e \cdot G(z) dz \tag{2.32}$$

where e is the elementary charge.[77,78]

2.4 Förster Energy Transfer

Resonance energy transfer (RET), often known as electronic energy transfer (EET) is an omnipresent photophysical process where an electronically excited 'donor' molecule transfers its excitation energy to an 'acceptor' molecule

$$D^* + A \xrightarrow{\text{RET}} D + A^*. \tag{2.33}$$

These molecules are coupled through the electric field by dipole-dipole interaction. A typical schematic illustration is shown in figure 2.8, which depicts a minimal model of a coupled two-state system. Through light absorption the donor becomes excited. Before the donor can decay to the ground state, its excitation energy is transferred to the nearby acceptor molecule, which is excitable with lower energy than the donor molecule. Thus, a virtual photon is exchanged. An elegant theory which explains the relation between the experimental observables and the mechanism of FET was first suggested by Förster, therefore this phenomenon is often referred to as Förster resonance energy transfer (FRET). FRET is a very interesting phenomenon since it requires neither a charge exchange nor physical contact.

The FRET efficiency depends on many parameters, but can roughly be allocated to following variables:[79]

- the distance R between the donor and acceptor molecule
- the spectral overlap between the donor emission and acceptor absorption spectrum

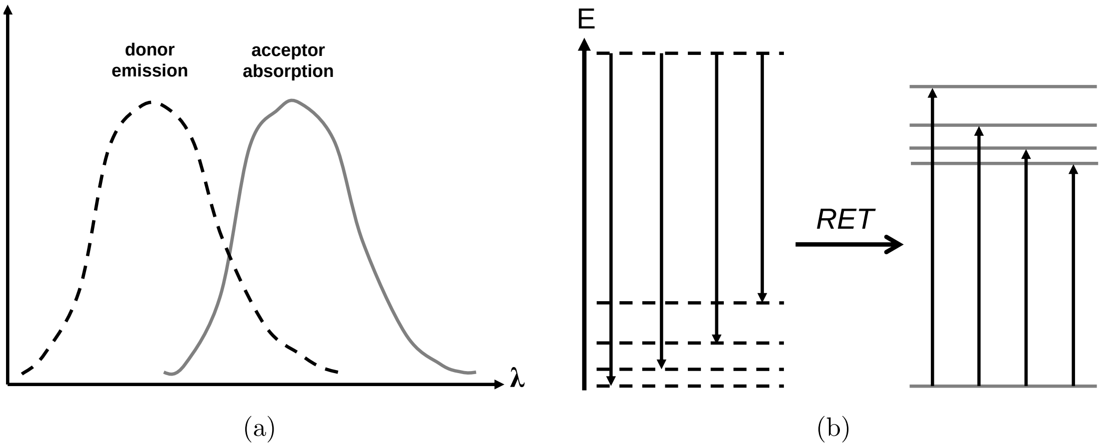

(a) (b)

Figure 2.8: Schematic representation of resonance energy transfer with the spectra of the donor and acceptor (a) and the corresponding energy level diagram (b).

- the relative orientation between the dipole moments of the donor and acceptor molecule.

The Förster theory is based on the established theory for the coupling of a state to a quasi continuum of secondary states. This model enables the explanation of dynamic processes including the decay of a 'stationary' state. In respect thereof, Förster wrote a Fermi Golden Rule expression for the RET rate with a matrix element considering the interaction of the excited donor and ground-state acceptor as a purely electronic coupling V. The coupling of the transition moments of the donor and acceptor is realized by Coulombic interaction, conceptually analogous to coupled oscillators. Energy conservation and nuclear overlap factors were separated from the electronic coupling by the Born-Oppenheimer approximation and the Franck-Condon principle and (to) determine the emission and absorption events of the donor and the acceptor molecules, respectively,

$$k = \frac{2\pi}{\hbar} d\epsilon \sum_k \sum_l P(k)P(l) \left| u(\epsilon_d^{-k}, \epsilon_a^{-l}, \epsilon) \right|^2 \tag{2.34}$$

where ϵ_d^{-k} is the energy gap of the donor molecule with an adjustment to *P(k)* for thermal population of the mode k in the excited state and similarly ϵ_a^{-l} regarding to the ground state of the acceptor. Due to normalization the matrix element u is a dimensionless quantity. If the electronic coupling is independent, u can be expressed to:

$$u = \sum_k \sum_l P(k)P(l) \left| u(\epsilon_d^{-k}, \epsilon_a^{-l}, \epsilon) \right|^2 = |V|^2 J(\epsilon), \tag{2.35}$$

in the abscence of static disorder, the spectral overlap *J(ϵ)* (ensures the energy conversation) takes the simple form of an overlap between donor emission ($f(\epsilon)$) and acceptor absorption ($a(\epsilon)$) spectra. For normalization the unit area is referred to on the energy scale, that is $J(\epsilon) = f(\epsilon)a(\epsilon)$. Thus, equation 2.34 can be rewritten as

$$k = \frac{2\pi}{\hbar}|V|^2 \int_0^\infty d\epsilon J(\epsilon) = \frac{1}{h^2 c}\left|\tilde{V}\right|^2 \int_0^\infty d\tilde{\nu} J(\tilde{\nu}) \tag{2.36}$$

with V as the electronic coupling between donor and acceptor, which is for $\tilde{V}$ expressed in units of cm^{-1} and $\tilde{\nu} = \epsilon/2\pi\hbar c$. Any dielectric shielding of the electronic interaction due to the surrounding medium is considered in V.

Förster continued and expressed the rate of EET from donor to acceptor as

$$k^{Förster} = \frac{1}{\tau_D}\frac{9000(ln10)\kappa^2\phi_D I}{128\pi^2 N_A n^4}\frac{1}{R^6} = \frac{\phi_D}{\tau_D}\left(\frac{R_0}{R}\right)^6 = \frac{\phi_D}{\tau_D}\left(\frac{8.785\times 10^{-25} I}{n^4 R^6}\right), \tag{2.37}$$

where κ[16] is the orientation factor associated with the dipole-dipole interaction between donor and acceptor, R is their center-to-center distance in units of cm, n is the refractive index of the medium, N_A is the Avogadro constant (6.023×10^{23}), ϕ_D is the fluorescence quantum yield in absence of the acceptor, and τ_D is the lifetime of the donor. The Förster radius R_0 defines the distance at which the energy-transfer efficiency is 50%.[80,81] It can be determined by the following equation

$$R_0^6 = \frac{9000(ln10)\kappa^2\phi_D}{128\pi^2 N_A n^4}\left[\int_0^\infty F_D(\lambda)\epsilon_A(\lambda)\lambda^4 d\lambda\right], \tag{2.38}$$

with the overlap between the fluorescence of the donor, normalized to unity area, $F_D(\lambda)$, and the molar absorption spectrum of the acceptor, $\epsilon_A(\lambda)$, scaled by the wavelength to the fourth power. The stronger this resonance term is, the more efficient will be the energy transfer.

The Förster theory was originally developed to account for resonant energy-transfer phenomena in dilute solutions. Hence, significant deviations are to be expected when the distance between the donor molecule (D*) and the acceptor (A) becomes similar to the size of the chromophore.[81]

Excitation of a dye can be accomplished by either energy transfer or charge transfer from one material class to the other. In the case of energy transfer, an exciton is formed at a donor molecule, which is then transferred to the acceptor by either resonant coupling or by coherent charge exchange (Förster or Dexter transfer, respectively).[46] For excitation by charge transfer, electrons and holes from the donor are sequentially trapped by the acceptor resulting in exciton formation on the acceptor.

---

[16] for random orientation κ^2 is equal to 2/3.[80]

Chapter 3

Gradient C_{60}:ZnPc Absorption Layers in Small-Molecule Solar Cells

3.1 The Architecture of Organic Solar Cells

When the first organic solar cell based on small molecules was introduced in 1985 by Ching W. Tang, it consisted only of a two-layered interface between an electron donor and an acceptor material, yielding an efficiency of 0.95%.[82] He discovered that the efficiency dropped after a certain layer thickness was exceeded, which indicated that the separation of the exciton occurs only at the donor-acceptor interface. In order to enhance the interface surface and to ensure charge carrier creation, a blended layer was inserted between the pure donor and acceptor layers which was achieved by the co-deposition of the two materials and became renown as the concept of the bulk heterojunction (BHJ).[83] Since the first working organic solar cells, the efficiency has continuously been increased along with the complexity of the cell. Figure 3.1 depicts the historical development of the device structure with respect to their efficiency. Each increase in efficiency has been associated with the introduction of an extra layer of material. The utilization of exciton blocking layers (EBLs) has become essential because excitons are quenched if they diffuse to the metal contact. Due to the low conductivity of organic semiconductors, their final thickness has been limited to a few nm which has made the incoupling adjustment of the incident light rather difficult. This has been much easier by using the concept of p- (or n-) doping of hole (or electron) transport layers.[84] Over time, the more the pn-structure of inorganic semiconductors has been mimicked, the better has been the performance of the solar cell. The best devices[1] based on

---

[1] The best solar cell (tandem device) based on small molecules reaches an efficiency of 12.0% on an active area of 1.1 cm^2, fabricated by Heliatek and certified by SGS.[85]

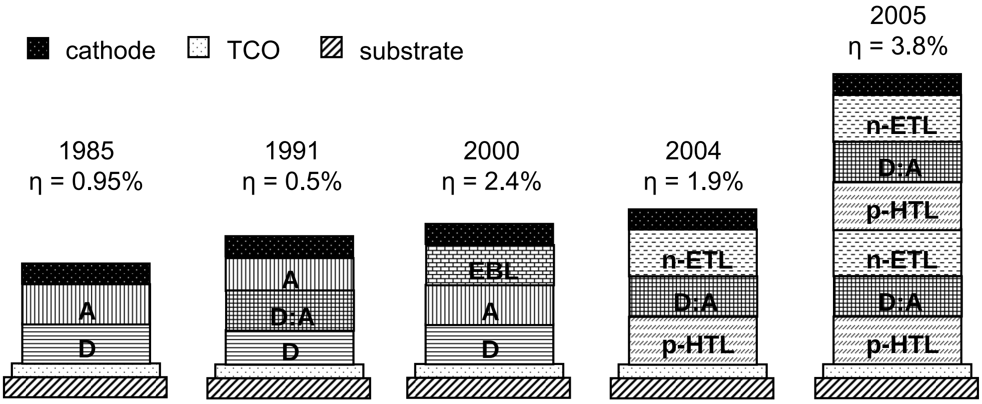

Figure 3.1: Historical development of the invention of new layer segments for organic solar cell architectures starting with the planar heterojunction in 1985,[82] the bulk heterojunction in 1990,[83] the exciton blocking layer in 2000,[89] the doping of hole and electron transport layer in 2004[84] and the realization of a tandem architecture in 2005.[90]

small molecules, which have been described so far, consist of p- and n-doped transport layers, where the intrinsic absorption layer is localized in between these layers resulting in a pin-stacked solar cell. Another important improvement for solar cell architecture has been the previously mentioned intimate mixing of donor and acceptor molecules to enhance the interfacial area of the donor-acceptor interface.[86] Heating of this blend resulted in the enhancement of the cell's performance due to morphology changes, enabling a better charge separation and a better transport to the electrodes.[87,88] It is generally agreed that an optimum nanoscale morphology with a balanced interfacial area and continuous pathways is necessary. Although considerable effort has been put into morphology optimization, less work has been performed on absorber layers with controlled compositional changes.

Although many of host- und dopant materials for the transport layers have been investigated, the list of examined absorber materials with appropiate characteristics is comparably short: metal phthalocyanines, porphyrins, perylene, pentacene, oligothiophenes and squarines.[91] A common combination for bulk absorbers is C_{60} as acceptor with a metal phthalocyanine as donor. This combination is characterized by strong absorption coefficients in the visible range of the spectrum and high thermal stability. Although the zero-field mobility of C_{60} is acceptable with 5.1×10^{-2} cm^2/Vs for electrons, the hole zero-field mobility of phthalocyanines is several orders of magnitude lower, *e.g.* for CuPc just 7.4×10^{-4} cm^2/Vs.[63] Rand *et al.* investigated the charge mobility of pure materials as well as the blend of both materials in different concentration ratios as depicted in figure 3.2 a.[63] The diagram shows that the charge carrier mobility decreases for holes (or electrons, respectively) with increasing the material concentration of the acceptor (or donor, respectively). Furthermore, the hole mobility is much more affected by

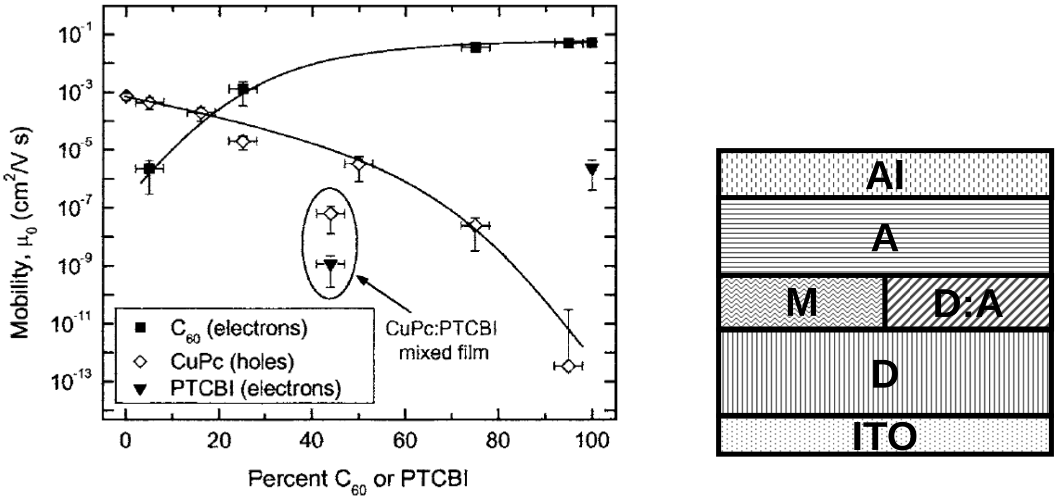

(a) (b)

Figure 3.2: (a) The zero-field mobility, μ_0, for electrons (filled symbols) and holes (open symbols) in various pure and mixed films containing CuPc (diamonds) and C_{60} (squares) *vs.* weight percent of C_{60}, reproduced from reference[63]. (b) Simple architectures of the first gradient-like structure with a D-M-A (left) and D-D:A-A (right) layer composition.

concentration variations than the electron mobility.

Regarding the problem with the charge carrier mobility, an ideal structure for a solar cell is proposed where the p-type layer is located near the high work function anode and the n-type layer close to the low work function cathode. In this work, a concept has been examined to improve this property within the absorber layer by processing the BHJ layer to have a vertically graded distribution of the bulk composition. This should result in a cumulative charge carrier mobility from the center of the absorption layer towards their corresponding transport layers. With this approach, a better balanced charge carrier distribution should be obtainable, which is crucial to minimize recombination losses. The existence of a donor-acceptor compositional gradient has already been proposed for several polymer-based solar cells and showed better performances, compared with their counterparts. The graded constitution of the absorptive layers has been achieved by appropiate solvent modification,[92] annealing[37,86] or thermally-induced interdiffusion of two films.[93] For small molecule based devices, little work has been done in order to investigate the positive influence of a gradient-like structure. Hong *et al.* examined the influence of a multilayered absorption stack on the device efficiency. He showed that the performance corresponded to the number of interfaces between the donor and acceptor. Keeping this number constant it was also reported that the highest efficiency was achieved with a "graded" thickness distribution (C_{60} 1, 2, 3 nm/ ZnPc 3, 2, 1 nm *vs.* 3 × C_{60} 2 nm/ ZnPc 2 nm).

The simplest gradient-like structure has already been realized many times without calling it a gradient. Either, a mixed D:A layer is positioned between a pure donor and acceptor material layer,[83] or an interlayer with moderate, but similar transport properties (M) for holes and electrons is inserted between the donor and acceptor (*cf.* figure 3.2 b).[94] Sullivan and Heutz *et al.* have gone a step further. They have prepared several samples including a device where the constitution of the blended absorption layer has been varied three times (CuPc:C_{60} with 75:25, 50:50, 25:75) surrounding this structure by pure CuPc and C_{60}.[58,88] This sample has shown an efficiency improvement of 1.36% compared to the reference device with a fixed 50:50 blended layer (1.17%). The increase both in J_{SC} and FF have been attributed to an improved charge collection efficiency driving the charges to the appropriate electrodes.[58,88] This has also been confirmed by the work of Chen and co-workers.[95] Tress *et al.* on the other side have used drift-diffusion simulations showing that the gradient helps to reduce recombination processes which is particularly beneficial for hybrid planar/ bulk heterojunction structures. Efficiency improvements have mainly been related to optical effects.[96] Here, it will be shown that both arguments are valid for the cell architecture investigated here. Although otherwise disregarded in the literature[96] a graded absorption layer can also be beneficial for the solar cell architecture p-HTL/ C_{60}:ZnPc/ BL/ n-ETL. The positive influence of such a gradient architecture on the solar cell performance will be demonstrated by the variation of the gradient strength and the absorption layer thickness after the absorption layer itself has been optically characterized in detail.

3.2 Theoretical Considerations

3.2.1 Optical Issues

With respect to the incoupling of incident light, a graded structure can be helpful to increase the photocurrent. As presented in figure 3.3 a, the square amplitude of the optical field Ψ^2 varies for each wavelength and each position within a stacked solar cell[2]. The optical field gets partially absorbed and therefore (excitons and) charges are formed. Although the AL is relatively thin, the fact that the incoupling of light is differently sensitive for each wavelength can be used for a graded structure. In figure 3.3 a two incoupling maxima are located in the HTL (730-800 nm) and between the HTL and AL (550-600 nm). The arrow emphasizes the shift of the maximum square amplitude regarding the position and the wavelength. In this example it means that light of low energy is more closely located to the HTL and light of higher energy closer to the ETL. This distribution of the field amplitude

---

[2] Architecture used for simulations: 130 nm ITO / 50 nm p-HTL / 35 nm AL / 20 nm BL / 15 nm n-ETL / 200 nm Al.

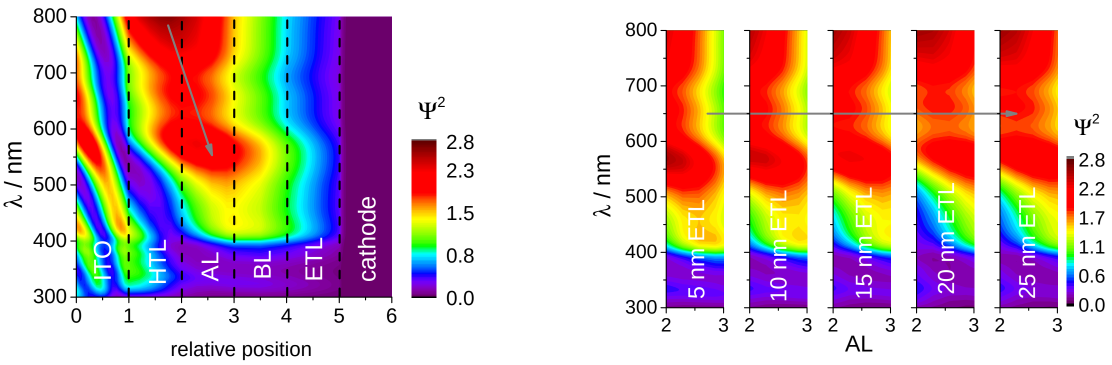

(a)

(b)

Figure 3.3: Graphical illustration of the field amplitude penetration profile of the incident light for (a) a whole solar cell as a function of the layer position and (b) the penetration profile only for the absorption layer for various ETL thicknesses.

within the absorption layer can be changed with regard to intensity and position by modifying the thicknesses of the transport layers, which is depicted in figure 3.3b for an ETL variation. Considering this, a graded structure should be fabricated, where the low-energy absorber has a higher concentration close to the HTL and a lower concentration towards the ETL. An ETL thickness should be chosen such that the absorption maximum of the low energy absorber has its maximum close to the HTL and the high energy absorber to the ETL, respectively. Since C_{60} provides very strong absorption bands from 300-400 nm and from 400-500 nm, its concentration should increase towards the ETL.

3.2.2 The Electronic Structure of the ZnPc/C_{60} Heterojunction

When the contact between a donor and an acceptor is formed, the work function difference of the separate phases is overcome by induced band bending and formation of an interface dipole. Park and co-workers investigated the electronic structure of the C_{60}/ZnPc interface for organic solar cells and explained the higher V_{OC} for BHJ cells compared to PHJ cells.[97] In blend layers, the LUMO energy of C_{60} is higher localized due to charge redistributions of dipoles. Additionally, a smaller shift to lower binding energies of the ZnPc HOMO has been observed. Its origin has been assigned to energy level relaxation from the blended layer/ ZnPc interface.[97] Hein *et al.* determined the influence of annealing ZnPc on the electronic structure of the ZnPc/C_{60} interface. With increasing annealing temperature, the C_{60} HOMO position shifted to higher binding energies. Because the ionization energy of ZnPc changed strongly during the transition from 124 ℃ to 155 ℃, a transition from the α to the β-phase was discussed.[98]

Since a ZnPc/C_{60}:ZnPc/C_{60} layer sequence is itself a coarse gradient an energy

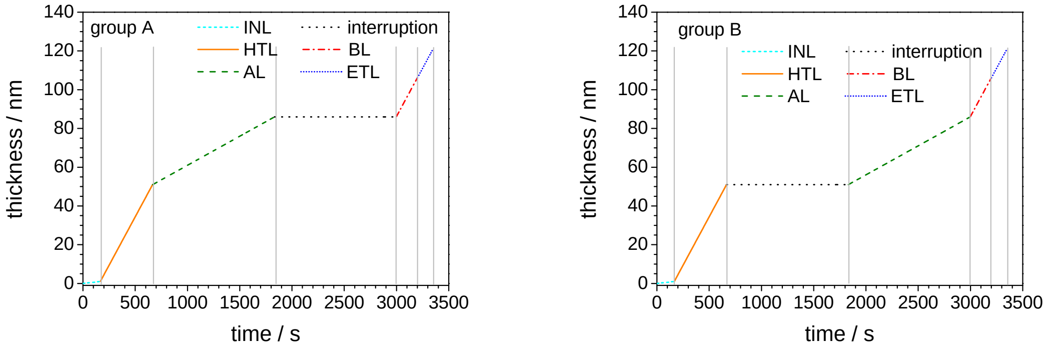

(a)

(b)

Figure 3.4: Schematic representatation for the realization of the experiment process including the test (a) and reference sample (b) within one run.

level distribution as presented in figure 3.9 a can be assumed. Here, the HOMO level of ZnPc rises with increasing ZnPc content and is in accordance to the experimental data presented by Tress and co-workers.[68] Due to a higher-lying HOMO energy level of the HTL material (p-spiro-TTB), extraction barriers for holes between the donor and HTL HOMO can be neglected. Thus, the open circuit voltage correlates directly with the electronic structure of the donor and acceptor material. Because the stack architecture of the organic solar cell comprises a pure C_{60} layer as blocking layer and an n-doped C_{60} layer as ETL, the transport level for the electrons is assumed not to be influenced as also claimed in literature.[68] A band-bending-like feature similar to that described here has also been reported for the F_{16}CuPc/CuPc system by Mao and co-workers.[99]

3.3 Realization of the Experiments

In order to compare devices with homogeneous and graded C_{60}:ZnPc films, test and reference cells were processed within a single run. Four substrates (each four pixels on one substrate) can be coated at the same time. In this way, it is valid to compare the results of the test- and reference cell without needing to consider run-to-run fluctuation. In order to decouple the coating of the absorption layers from each other, a wedge tool and a half opened mask for the organic material have been used. The other organic layers were processed through the same shadow masks. The process flow of this method is depicted in figure 3.4. A decrease of the substrate temperature resulting from the heating interruption due to the mask and substrate transfer (≈ 7 min) can be excluded since convective thermal transfer is inhibited at high vacuum and the heat is stored in a silicon mat which has been placed between the substrate and the cover plate.

For substrate heating during deposition, a test run was carried out to estimate

Table 3.1: Summary of measured key properties of solar cells fabricated according to process A and B.

group	V_{OC} / mV	J_{SC} / mAcm^{-2}	FF / %	η / %
A	530 ± 5	5.80 ± 0.09	59.9 ± 1.4	1.85 ± 0.08
B	517 ± 6	5.75 ± 0.12	61.0 ± 1.1	1.82 ± 0.05

the impact of different heating profiles due to mask exchange on the device performance. For this purpose, simple-stacked solar cells[3] at a substrate temperature of 125 °C were fabricated. A weak influence of the process on the key properties was observed (*cf.* table 3.1). Whereas J_{SC}, FF and the η are within the standard measurement uncertainty, V_{OC} of group A is slightly higher than for group B. This is attributed to the longer heating duration of the absorber layer C_{60}:ZnPc according to the heating profile of A. For room temperature samples no influence on the samples has been observed. The devices were processed in a custom made vacuum chamber (BESTEC GmbH, Berlin) of a pressure of 10^{-7} mbar. The material flux was monitored with a quartz microbalance and was controlled by the tool software. This software control is very important for the continuous growth of the graded composition. The given fractions for multi-component mixed films have been related to the volume.

For the implementation of the gradient, the rate regulation mode was modified to have a maximum rate deviation of ± 3%. Based on the fact that rates of both the donor and the acceptor material have to be adjusted simultaneously, a deposition recipe has been written to control the evaporation. Here, the gradient has been approximated as a multilayer system consisting of 5 nm thick layers with different compositions (7 × 5 nm). After each deposition of a 5 nm blended film, the rates have linearly been de- (ZnPc) and increased (C_{60}), while keeping the total rate trend constant in order to exclude morphological differences due to dissimilar heat introduction. Figure 3.5 shows the non-linear (a) and linear (b) increase of the C_{60} and ZnPc content during deposition, whereupon the total thickness of blended layers grows constantly.

3.4 Results and Discussion

The processes that contribute to the efficiency of organic BHJ solar cells include (i) the absorption of photons and the creation of excitons, (ii) exciton diffusion towards the charge separation interface, (iii) exciton dissociation to free electrons and holes by the heterojunctions, and (iv) charge carrier transport and collection by the electrodes. Therefore, these issues will be discussed in the following section.

---

[3] 50 nm p-spiro-TTB, 35 nm C_{60}:ZnPc (67:33), 20 nm C_{60}, 15 nm n-C_{60}, 200 nm Al.

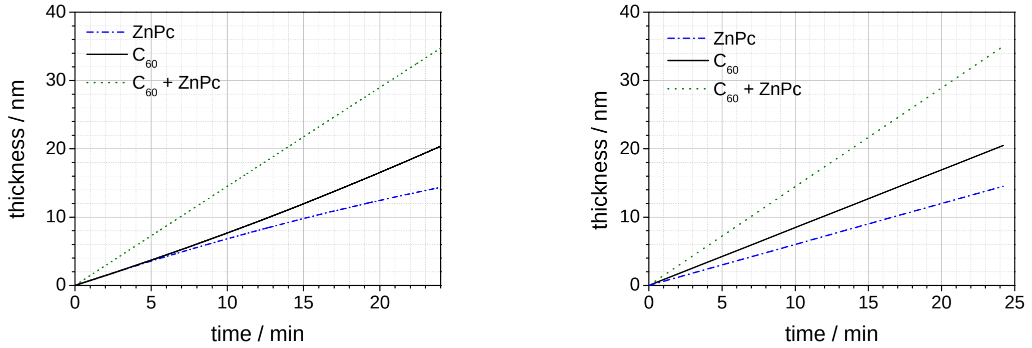

(a) (b)

Figure 3.5: Diagram of the thickness increase measured during depostion and its composition for the (a) gradient (ZnPc: 50→33%/C_{60}: 50→67%) and the (b) homogeneous (ZnPc: 41.5%/C_{60}: 58.5%, b) absorber layer.

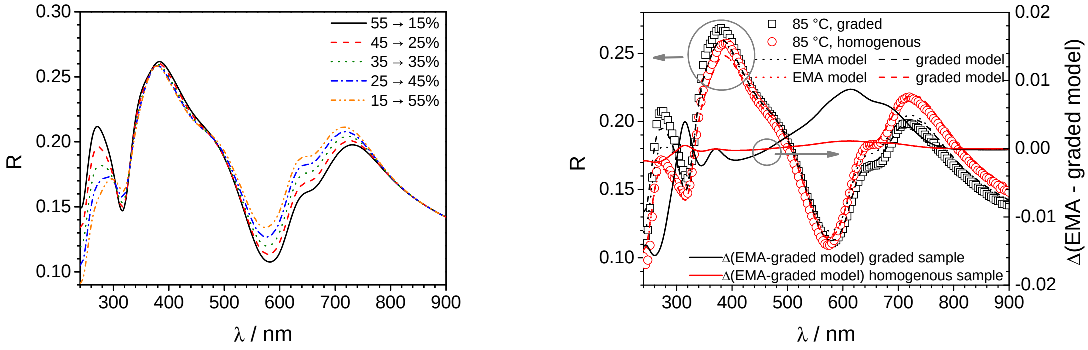

(a) (b)

Figure 3.6: (a) Simulated reflection spectra for C_{60}:ZnPc thin films with a total ZnPc content of 35% using a graded fitting model and (b) measured reflection spectra of a gradient-like and a uniform C_{60}:ZnPc layer with a thickness of 80 nm and the results of the fitting curves.

3.4.1 Optical Characterization of the Absorption Layers

To verify the success of the gradient deposition technique, UV/vis reflection spectroscopy has been used to investigate the layer structure. A C_{60}:ZnPc thin film reflection spectrum has been simulated with different gradients, keeping the total ZnPc content unchanged. The results of these simulations are depicted in figure 3.6 a. The behavior of optical regions from 240 to 300 nm and from 540 to 740 nm is very sensitive to the layer architecture. The higher the initial ZnPc content, the lower the reflection in the larger wavelength range and the higher in the shorter wavelength region. This observation is in agreement with expections.

Based on this, 80 nm thick samples both with a uniform and a graded blend structure have been fabricated in order to verify the gradient architecture. Figure 3.6 b presents the measured reflection spectra of the aforementioned samples. Each spectrum has also been modeled using a homogeneous (EMA model) and a gradient-like (using a graded model) distribution based on the optical properties of C_{60} and ZnPc determined from pure films prepared under comparable conditions. Due to the dependency of Q^+/Q described below, the oscillator strength has been introduced as a fitting parameter in addition to the film thickness d and the layer composition or gradient. For the homogeneous (*i.e.* no gradient) samples both models are suitable to describe the measurement. The red dotted line in figure 3.6 b shows a negligible difference between the two simulated spectra. The gradient model results in a fitted gradient of 41→38.5% (MSE of 0.81) which is consistent with a homogeneous layer within the expected fitting error range (MSE of EMA fit was 0.92). However, with a graded sample, the two fitting models result in significantly different simulated spectra as the homogeneous model cannot account for the graded layer composition (MSE of 2.30). The best fit using the graded model results in a gradient of 49→30% (MSE[4] of 0.80), which is in the range of the expected values according to the deposition process. The deviation is most strongly expressed at the optical regions between 260 to 320 nm and 500 to 760 nm, *i.e.* exactly the positions where the highest influence was predicted according to the reflection simulations (*cf.* figure 3.6 a).

Furthermore, absorbance spectra have been recorded at different positions[5] within a 180 nm graded and uniform C_{60}:ZnPc layer. The data are presented in figure 3.7 a. Since the aggregation behavior of ZnPc is very sensitive to concentration variations, the Q band can be used to investigate the graded composition. Figure 3.7 a, top shows the measured absorbance spectra for a graded and for a uniform layer. The Q^+ band (625 - 633 nm) derives from electronic $\pi^* \leftarrow \pi$ transitions and the Q-band (682 - 688 nm) is assigned to an excitonic transition or vibronic interval.[100–103] These transitions are responsible for the intense visible absorption and suggest that ZnPc may exist in the α-phase.[42] The analysis of the Q-band spectrum provides an opportunity to explore the relationship between its shape and the packing structure of ZnPc in thin films. The position of the Q-band and its full width at half maximum (FWHM) have proven to be most sensitive to the molecular ordering in the stacking direction over distances of at least 6-10 molecular units.[104] Whereas the existence of the Q^+ peak is attributed to aggregated ZnPc molecules with cofacial arrangement leading to strong intermolecular coupling, the Q peak is claimed to originate from the monomeric ZnPc species which can also easily be assigned in the solution spectrum (*cf.* figure B.1).[105–108] By analyzing the ratio of these peaks, the relative concentration of higher aggregated ZnPc species within the layer can be determined.

Initially, the content of higher aggregated ZnPc species is almost equal for

---

[4] MSE = mean squared error.

[5] The positions correspond to the following thicknesses: 1. 30 nm , 2. 70 nm, 3. 110 nm, 4. 150 nm and 5. 180 nm.

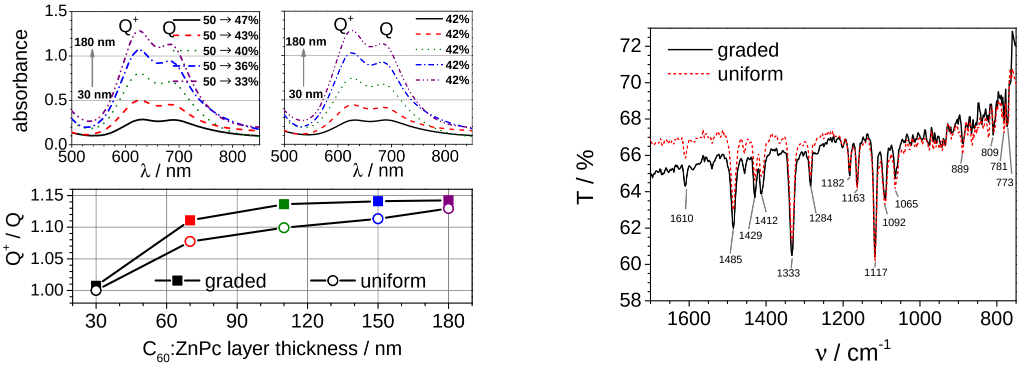

(a) (b)

Figure 3.7: (a) Absorbance spectra of a graded (top, right) and uniform (top, left) C_{60}:ZnPc mixed layer. The lower part shows the aggregation development by means of the absorbance ratio A_{Q^+}/A_Q for both layer systems. (b) FT-IR spectrum of a graded (black, line) and a uniform (red, dashed) C_{60}:ZnPc mixed layer.

both sample types. However, with rising thickness, the concentration of the higher aggregates rises which is believed to be due to boundary surface effects. In graded samples, the concentration of higher aggregates increases faster than for uniform films and saturates at a certain point. For uniform samples this saturation ratio is reached about 90 nm later. Hence, with a gradient-like structure, the formation of higher aggregated ZnPc has been accelerated. This higher aggregation grade may result in a comparatively higher hole mobility on the ZnPc sites, which will be beneficial for the device performance due to facilitated charge carrier extraction.

In order to investigate the vibrational behavior of ZnPc as a function of the processing conditions, spectra in the infrared range have been measured on silicon substrates. This technique has the advantage of only being sensitive to polar bonds (transition dipole moment $\neq 0$), so that apolar molecules such as C_{60} do not appear in an IR spectrum. This facilitates the interpretation of spectrum from a blended absorption layer, if the focus lies on ZnPc. Because the spectral range from 4000 to 2000 cm^{-1} is related to vibrations occuring in functional groups, no significant peaks can be measured for a C_{60}:ZnPc mixed layer. Hence, figure 3.7 b shows the IR spectrum of a uniform and graded layer recorded from 2000 to 750 cm^{-1}. This interval is often called the finger print region, which is very specific and unique for each molecule and can be also be affected by different processing conditions. Even different crystal modifications of ZnPc can be distinguished *via* IR spectroscopy. As seen in the IR transmission spectra, no significant difference can be identified between the gradient and uniform samples. The assignment of the peaks leads to the conclusion that ZnPc exists in the blended layer as α-modifiction, as has already been pointed out by other authors.[100,109,110] The peaks and their corresponding vibrations are summarized in table 3.2.

Table 3.2: Summary of measured absorption peaks of C_{60}:ZnPc thin films and their assignment. Those, which have been referenced to peaks occuring in α-ZnPc are presented in the third column.

measured / cm^{-1}	strength[a]	reference / cm^{-1}	assignment
1610	m	1608	-C=N-C (aromatic)
1541	w	-	-C=N-C (aromatic)
1485	s	1487	asymmetric C-N=C-streching
1429	m	-	-
1412	m	1410	-
1333	vs	1333	C-C-streching mode of pyrrole
1284	m	1290	-
1182	m	-	-
1163	m	1167	C-C-streching mode of pyrrole
1117	vs	1117	C-C-streching mode of pyrrole
1092	m	1080	C-N-bending mode
1065	m	1061	C-H-bending mode
889	m	888	aromatic C-H out of plane bending mode
809	m	-	aromatic C-H out of plane bending mode
781	m	777	aromatic C-H out of plane bending mode
773	m	773	aromatic C-H out of plane bending mode

[a] w: weak, m: medium, s: strong, vs: very strong.

3.4.2 Effect of the Substrate Temperature

The positive effect of substrate heating during and after deposition has been reported both for polymer and small-molecule based solar cells.[11,37,87,111–113] The enhanced efficiencies have been attributed to a better interpenetration of the D:A system and expanded percolation paths. Because of the substrate heating, the thermal energy of the molecules deposited on the substrate is higher, so that they can diffuse over larger distances before they adsorb.[87] Consequently, a more interconnected network and fewer isolated clusters of the donor and acceptor material are formed, which facilitates charge carrier extraction. Therefore, the transport properties can be dramatically improved with less recombination losses yielding lower saturation values S[6] and higher FF.

In the best case, employing the gradient architecture should show an enhancement of the cell performance or in the worst case no change after all. Surprisingly, the introduction of a compositional gradient has affected the efficiency of room temperatured samples in a detrimental way. Figure 3.8 a presents the J-V curves of graded solar cells and their uniform reference cells. The corresponding key values can be taken from table 3.3. Solar cells processed at room temperature and with a graded absorption layer always show worse characteristics than their homo-

---

[6] defined as the ratio ($J(-1\ V)/J_{SC}$).

Table 3.3: Key values of uniform (41.5% ZnPc) and graded (50→33%) solar cells[a] in dependence on the substrate temperature (ϑ_{Sub}).

ϑ_{Sub} / ℃	V_{OC} / mV	J_{SC} / mAcm^{-2}	FF / %	η / %	S
25 (graded)	463	7.21	45.0	1.44	1.33
25 (uniform)	482	8.08	46.5	1.82	1.14
85 (graded)	527	8.68	56.0	2.57	1.15
85 (uniform)	527	8.25	58.3	2.55	1.15
105 (graded)	539	8.14	59.6	2.60	1.16
105 (uniform)	533	7.97	56.0	2.39	1.14
125 (graded)	536	8.34	54.0	2.40	1.13
125 (uniform)	535	7.66	39.8	1.63	1.25
145 (graded)	556	5.84	31.4	1.02	1.43
145 (uniform)	583	3.98	22.0	0.52	1.90

[a] 130 nm ITO / 50 nm p-spiro-TTB / 35 nm C_{60}:ZnPc / 20 nm C_{60} / 15 nm n-C_{60} / 200 nm Al.

geneous analogs and yielded lower values for the V_{OC}, the J_{SC} and the FF; J_{SC} and the FF are most strongly affected.

At a substrate temperature of 85 ℃, the graded and uniform solar cells exhibit equal performance. As expected it increases for both types of solar cells due to the positive temperature effect on J_{SC} and FF. However, increasing the substrate temperature to 105 ℃, the advantages of a gradient-like structure start to dominate the side-effects such as enhancing the disorder. It is assumed that the grade of disorder might be higher in gradient-like blends compared to homogeneously processed layers; this also influences the charge carrier mobility. Additionally, another fact has to be taken into account. With decreasing material concentration in the blend, the probability to form closed paths to the transporting materials decreases. Therefore, charge carriers recombine and the FF and the J_{SC} decrease. Here, the graded sample is higher both in J_{SC} and FF compared to the reference cell and gives the highest efficiency within this set of experiments of 2.60%.

The relative improvement for a gradient-like structure becomes more distinct with continuously rising substrate temperature. The efficiency of the reference sample processed at 125 ℃ is one third lower than that of the graded sample but the uniform sample processed at 145 ℃ has only half the efficency of the graded sample processed at this temperature. A serious problem of the annealed samples is the series resistance in the first quadrant. One reason for the worse performance processed at temperatures higher than 105 ℃ might be the release of dopant molecules during deposition since their evaporation temperature ranges from 100 to 130 ℃ . Nevertheless, for graded samples the resistance is lower compared to uniform samples.

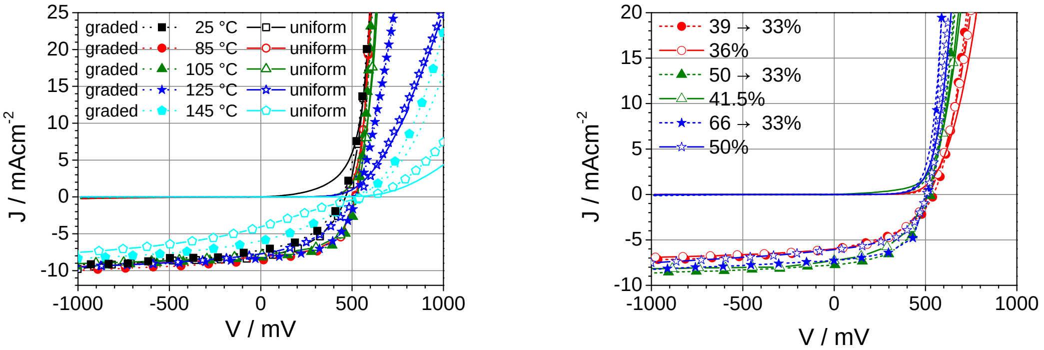

(a)

(b)

Figure 3.8: J-V characteristics under illumination (line and symbol) and in the dark (line) of OSC with a graded (filled symbol) and uniform (open symbol) absorption layer for (a) various substrate temperatures and (b) the total amount of ZnPc.

Table 3.4: Key values of solar cells[a] in dependence on the gradient strength keeping the total ZnPc amount fixed at 33% both for uniform and graded absorption layers.

Absorption layer	V_{OC} / mV	J_{SC} / mAcm^{-2}	FF / %	η / %	S
39→33%	556	5.93	43.2	1.42	1.21
36%	531	5.96	46.3	1.45	1.16
50→33%	526	7.86	51.4	2.14	1.09
41.5 %	513	7.44	47.0	1.80	1.10
66→33%	511	7.73	58.3	2.21	1.05
50%	505	6.19	52.6	1.65	1.21

[a] 130 nm ITO / 50 nm p-spiro-TTB / 35 nm C_{60}:ZnPc / 20 nm C_{60} / 15 nm n-C_{60} / 200 nm Al, ϑ_{Sub} = 85 °C.

3.4.3 Impact of the Gradient Strength

In order to investigate the influence of the gradient strength on the solar cell performance, the gradients have been varied. Since it is known that the efficiency is high at a ZnPc concentration of 33%, the gradients were varied while keeping the final amount (33%) of ZnPc constant. Table 3.4 gives an overview of the used gradients and the key values from the resulting samples. The corresponding J-V curves are shown in figure 3.8 b. For each graded sample, a reference sample with an equal total amount of ZnPc was fabricated for comparison.

The introduction of a gradient-like structure in the absorption layer has directly affected the performance of the solar cells. Whereas the positive contribution of a small gradient (39→33% *vs.* 36% ZnPc) can hardly be separated from the reference sample within the experimental uncertainty, it becomes obvious when the graded structure is sufficiently pronounced. The improvement on J_{SC} and FF of graded samples with regard to their homogeneous analogs correlates with the strength of the gradient, and so the highest efficiency of a graded absorption layer is achieved with a 66→33% ZnPc distribution. In principle, the graded samples are subject to the same physical relationships as their reference samples when modifying the blend constitution. V_{OC} decreases when increasing the total content of ZnPc, which has also been reported elsewhere.[68] This drop in V_{OC} has been attributed to different polarization energies in the mixtures, which results in a shift of the HOMO level from ZnPc.[114] Comparing the V_{OC} between the graded und uniform samples, it seems that graded samples always show slightly higher values. Since the increase is in the range of deviations due to processing fluctuation and measurements, it is difficult to conclude that there is a significant trend. However, numerical simulations predict an increase of around 10 mV for comparable graded samples.[96]

The higher the total content of ZnPc, the lower has been the series resistance due to improved percolation path formation, which can clearly be seen in the fourth quadrant of figure 3.8 b. Furthermore, the series resistance of all graded samples decreases with the gradient strength. This can be attributed to regions within the absorption layer with higher charge carrier mobility, in particular for holes since a higher sensitivity has been reported for holes than for electrons in phthalocyanine:fullerene blends.[63] The improvement becomes significant for 66→33% graded samples. The parallel resistance is affected neither by the total content of ZnPc in the absorption layer nor by the layer architecture. Therefore, *FF* reaches its maximum with a graded cell at a total content of 50% ZnPc, whereas J_{SC} reaches its maximum with a graded sample at 50→33% ZnPc.

3.4.4 Influence of the Gradient on the Absorber Layer Thickness

After the positive influence of the gradient strength has been demonstrated, it is assumed that the benefical effect of a gradient structure becomes more obvious with the thickness of the absorption layer. Hence, samples with a gradient from 50→33% have been fabricated for 35, 50 and 60 nm thick absorption layers. The key values of the resulting solar cells and their reference samples are summarized in table 3.5. The corresponding *J-V* curves are displayed in figure 3.9 b.

With rising absorption layer thickness both for graded and uniform samples, the J_{SC} value increases and the *FF* value drops. However, the graded samples always outperform their corresponding reference cells due to the much better *FF*. The advantage of graded samples increases with the layer thickness. For all samples the series resistance remains almost constant, but the graded samples show, in all cases, a slightly lower resistance. The parallel resistance decreases for thicker absorption layers which is due to the decrease of the EBL and ETL layer in order

Table 3.5: Key parameters of organic solar cells[a] with graded and uniform absorption layers for various absorption layer thicknesses.

structure	d / nm of C_{60}:ZnPc	d / nm of BL / ETL	V_{OC} / mV	J_{SC} / mAcm^{-2}	FF / %	η / %	S
graded	35	20 / 15	517	9.55	55.2	2.71	1.27
uniform	35	20 / 15	515	9.62	53.8	2.66	1.26
graded	50	5 / 15	513	9.86	50.5	2.56	1.44
uniform	50	5 / 15	511	9.72	46.2	2.30	1.43
graded	60	5 / 5	507	10.1	49.2	2.51	1.41
uniform	60	5 / 5	508	9.73	45.0	2.24	1.53

[a] 130 nm ITO / 50 nm p-spiro-TTB / C_{60}:ZnPc / C_{60} / n-C_{60} / 200 nm Al, ϑ_{Sub} = 85 ℃.

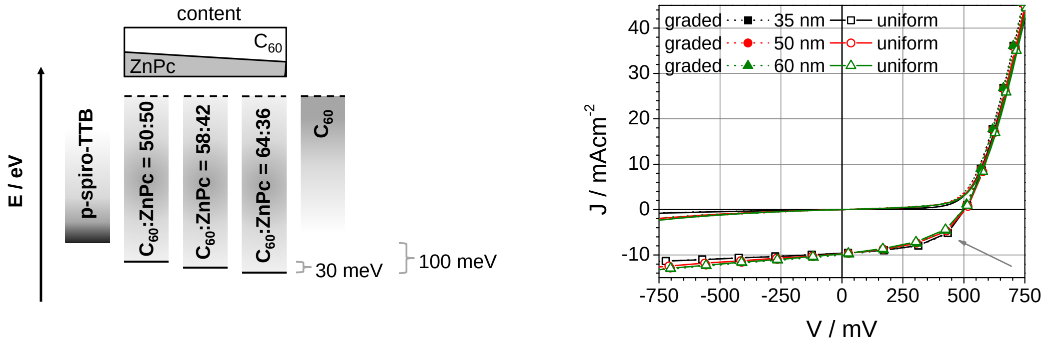

(a) (b)

Figure 3.9: (a) Proposed molecular orbital energies for various C_{60}:ZnPc mixing ratios. (b) J-V characteristics of OSCs in dependence on the absorption layer thickness with graded (filled symbol) and uniform (open symbol) D:A distribution under AM1.5 illumination (line + symbol) and in the dark (line).

to keep the total thickness of the stack constant. With respect to the J_{SC} value the dominance of the graded structure demonstrates the predicted better transport of the free charge carriers towards the transport layers.

3.4.5 Electrical Characterization

Because charge generation, recombination and charge transport in bulk heterojunction solar cells can be dependent on charge carrier density and applied voltage, it is important to investigate the spectral response (SR) spectrum of devices under high charge carrier densities and for different applied biases.

When the applied voltage reaches the open circuit condition, the internal electrical field decreases. Because bimolecular recombination increases and the charge separation efficiency declines, the spectral response signal becomes weaker. Brenner *et al.* used the shape variations in his voltage dependent EQE spectra because of its sensitivity to film morphology and microstructure.[115] For this purpose, three sample pairs have been chosen for a detailed investigation with the following

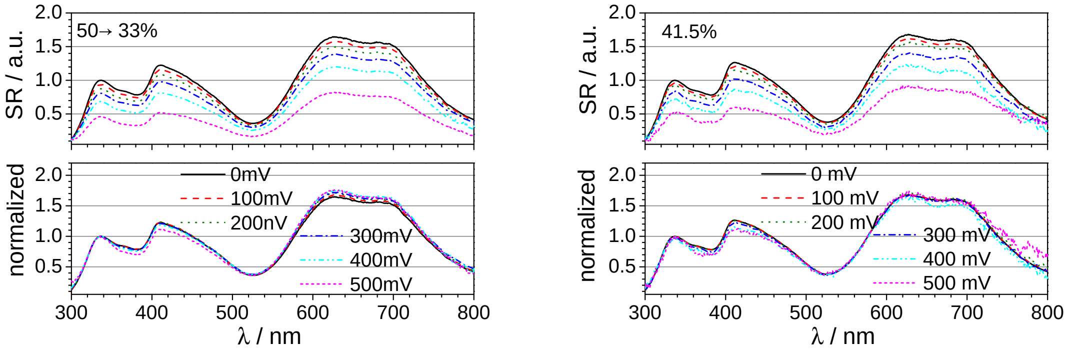

(a) (b)

Figure 3.10: SR spectra (top) recorded at various bias and their normalized analogs (bottom) of graded (a, 50→33%) and uniform (b, 41.5%) samples with an absorption layer thickness of 50 nm.

C_{60}:ZnPc structure: 50 nm with total content of 41.5% (*cf.* figure 3.10), 35 nm with 41.5% (*cf.* figure 3.11) and 35 nm with 50% of ZnPc (*cf.* figure 3.12) within the absorption layer. An increase in the applied bias leads to a reduction of the measured photocurrent. For better comparison, the lower subplot shows the curves normalized to the first peak at 340 nm.

For homogeneously processed samples (lower plots, figure 3.10 to 3.12) the normalized shape of the spectra remains unchanged with increasing bias voltages up to 400 mV. Only a bias voltage close to V_{OC} leads to a slight change. For the graded sample on the other hand, a different behavior appears. The normalized spectra reveal a decrease of the C_{60} related bands and an increase for the ZnPc attributed bands. Because of the distribution of the incident light within the absorption layer, most of the blue light is absorbed by C_{60} close to the cathode, where also the concentration of that molecule is higher. The red light is preferentially absorbed by ZnPc close to the anode. Furthermore, in a C_{60}:ZnPc blend the hole mobility is lower than for electrons. Holes that are generated by excitons originating from C_{60} related absorption in the blue region of light have to move for a long distance with a slowly rising mobility towards the anode, so, many holes recombine with electrons before reaching the transport layers. On the other hand, the current originating from ZnPc increases, which is a result of normalization at 340 nm where both ZnPc and C_{60} related excitons contribute to that peak. This has also been described by Tress and co-workers.[68] The positive influence of a graded structure thus originates from the better matching of light in-coupling to the spatial absorption profile of the materials.

In order to prove this, the relative decrease of the photocurrent signal from 0 to 400 mV applied bias has been determined and is summarized in table 3. Starting with the 35 nm sample with a gradient of 50→33% (*cf.* figure 3.11), the relative decrease of the photocurrent is for the graded sample larger than for the uniform

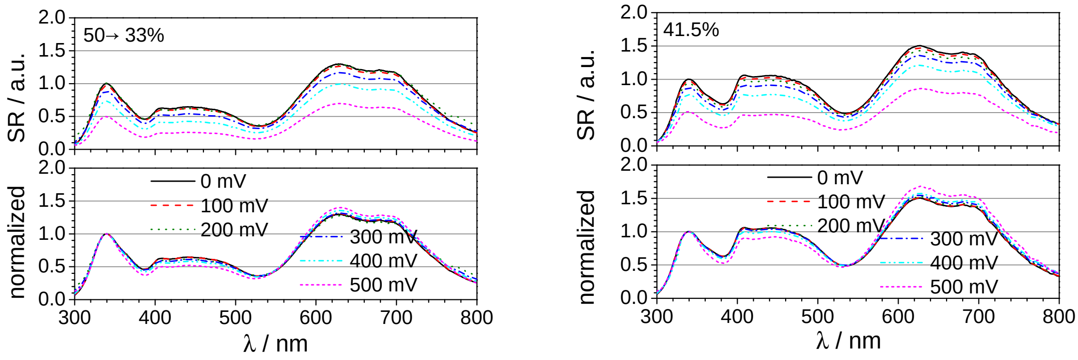

(a) (b)

Figure 3.11: SR spectra (top) recorded at various bias and their normalized analogs (bottom) of graded (a, 50→33%) and uniform (b, 41.5%) samples with an absorption layer thickness of 35 nm with an illumination intensity of 100%.

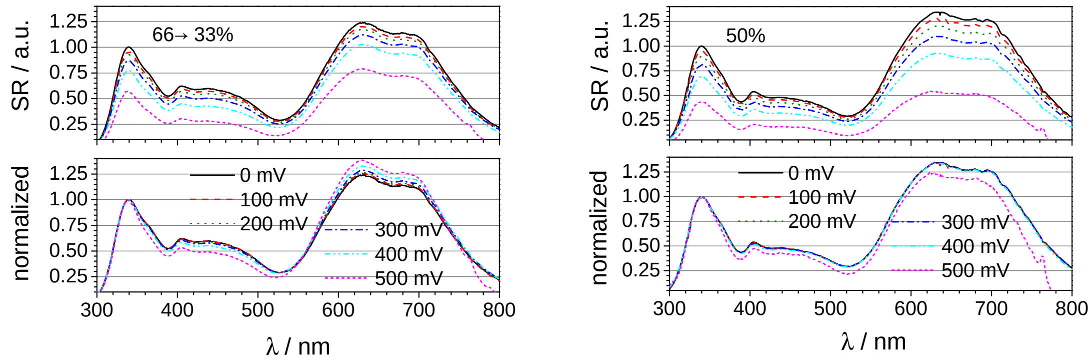

(a) (b)

Figure 3.12: SR spectra (top) recorded at various bias and their normalized analogs (bottom) of graded (a, 66→33%) and uniform (b, 50%) samples with an absorption layer thickness of 35 nm with an illumination intensity of 40%.

one, which means that the aforementioned recombination of the holes is higher for graded cells than for uniform samples. An increase of the thickness from 35 to 50 nm shows that both structures behave similarly. As expected, the absolute value of the decrease is higher, resulting from the enhanced recombination since the charge carriers have to pass a longer distance through the thicker absorption layer. For both types the recombination is similar, which means that the increased recombination for graded cells is compensated. Since the improved absorption for graded samples is for all sample pairs in the same range, the higher number of generated excitons can not be used as the only explanation.

With a closer look to the sample pair with the stronger gradient 66→33% (35 nm thick, *cf.* figure 3.12), the difference between the relative decline is remarkable. Whereas the current drops only by 21% for a graded sample, the current falls by 30% for the uniform sample. Although the recombination has increased for uniform samples, it has dropped for graded cells. Recombination can be re-

Table 3.6: Overview between the decay behavior of SR spectra for OSC with graded and uniform absorption layers in dependence on the composition and bias difference.

d_{AL} / nm	composition	bias difference	decrease[a]/ %
50	50→33%	0 to 400 mV	-29.2
50	41.5%	0 to 400 mV	-29.0
35	50→33%	0 to 400 mV	-26.2
35	41.5%	0 to 400 mV	-23.6
35	66→33%	0 to 400 mV	-20.8
35	50%	0 to 400 mV	-30.0

[a] The Reduction of graded and uniform samples have been determined by integrating the SR spectra and relating them for 0 and 400 mV.

duced by increasing the mobility of the charge carriers, which is supposed to be the case in graded layers. Since this property is supposed to be more pronounced for 66→33% than for 50→33% devices, the charge transport improvement is measureable by the stronger gradient sample. The positive influence of a graded absorption layer at low gradient strengths is thus attributed to the matched absorption profile for a mixed system. After the gradient strength exceeds a certain level, the mobility improvement due to the varied mixing ratio of hole transporting donor and electron-transporting acceptor contributes significantly to the increased photocurrent. Therefore, a high concentration of that material is necessary at the edges of the absorption layer, where mobility suffers the most by mixing it with a counter material, in this case ZnPc.

3.5 Outlook

The modified device architecture presented here opens a unique route to increasing device efficiency. The concept of employing a graded composition in the BHJ structure has been investigated and shown to work. The increase in efficiency of the fabricated samples is attributed more to an improved absorption profile than to the changed charge carrier transport. The positive influence of a graded structure is dependent on the gradient strength, layer thickness and processing parameters such as the substrate temperature. Since the size of the donor and acceptor aggregates affects the morphology as well, the process parameters for applying an gradient for efficiency increase will differ with new donor:acceptor systems. Furthermore, a graded system with a higher amount of the donor should result in better hole mobilities, and effects of mobility improvements related to a graded structure should be investigated further.

With regard to fabrication, the manufacture of a graded structure is rather challanging using point sources, as presented in figure 3.13. The left-hand side

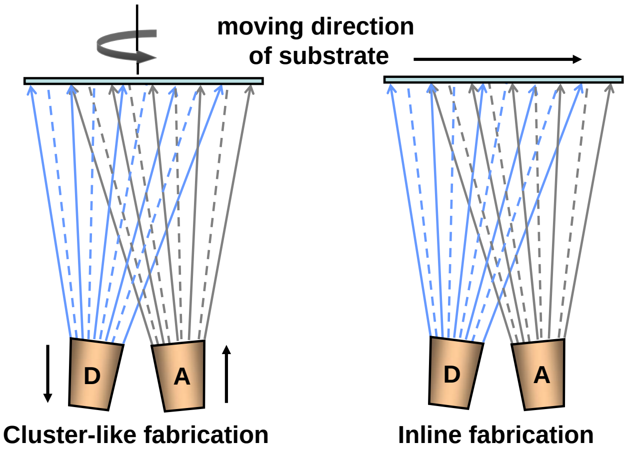

Figure 3.13: Graphical illustration of the possible fabrication processes for the insertion of graded structures.

shows the deposition principle in a cluster-like tool, where the substrate rotates for homogenity reasons. In order to realize a gradient on a substrate, the deposition rate of both the donor and acceptor material has to be simultaneously de- and increased, respectively. Without breaking the process flow, this can only be realized by computer control, and the deposition rates have to be continuously adjusted. Changing permanently the deposition rates costs time and is therefore not suitable for mass production. However, deposition processes where the sources are located in-line and the substrates pass the sources, are very suitable for the fabrication of graded layers. The right-hand side presents the deposition principle for such inline tools, where the movement of the substrate can easily be used to insert a graded structure in a mixed layer. Depending on the angles and the distance of the sources to each other, the strength of the graded zone can be adjusted. With alteration of the fixed deposition rates, the thickness of the gradient can be modified. Hence, this device architecture is very suitable for inline fabrication approaches appropiate for mass production such as roll-to-roll processes.

Chapter 4

Fluorescent Emitters and their Application in OSCs

The compounds 3-(2'-benzothiazolyl)-7-diethylaminocoumarin (coumarin 6, abbreviated C6)[1] and 4-(dicyanomethylene)-2-methyl-6-(*p*-dimethylaminostyryl)-4*H*-pyran (DCM)[2] are known to exhibit high molar extinction coefficients in the visible spectrum, to emit with high quantum yields[116] and to be very (photo)-stable.[117] Thus, these compounds have been widely used as laser dye materials[118–121] or down-shifting emitters in solar concentrators.[117,121,122] Additionally, many examples described the utilization of C6[34,123,124] and DCM[36,125–127] as emitter dopants for organic light-emitting diodes with excellent performance characteristics before it became clear that triplet emitters are necessary to achieve maximum power efficiencies. Because of the unique electro-optical characteristics of C6, it has been introduced into OLEDs to investigate the excitation mechanisms for photo- and electroluminescence.[34,128] Furthermore, it has successfully been used as a sensitizer in dye sensitized solar cells (DSSCs).[129,130]

Bulk heterojunction (BHJ) solar cells are composed of an interpenetrating network of a p-type semiconducting donor material and an n-type semiconducting acceptor material. This concept ensures a large interfacial area and results in large numbers of generated charge carriers, providing an approach for high-efficiency solar cells. However, C6 used as sensitizer in polymer based BHJ polymer cells has shown weak performance with efficiencies below 0.3%.[131–133] The poor performance has mainly been attributed to the low conductivity of the C6 containing absorption layer. DCM on the other hand has already shown better performance in planar heterojunction (PHJ) solar cells with an efficiency of 1.6%.[35] These examples show that compounds which have commonly been used as emitter materials are able to act as potential candidates for solar application. Other examples have also been reported of established OLED emitter materials being used as absorbers in

---

[1] For chemical structure *vide* figure 2.1.

[2] For chemical structure *vide* figure 2.1.

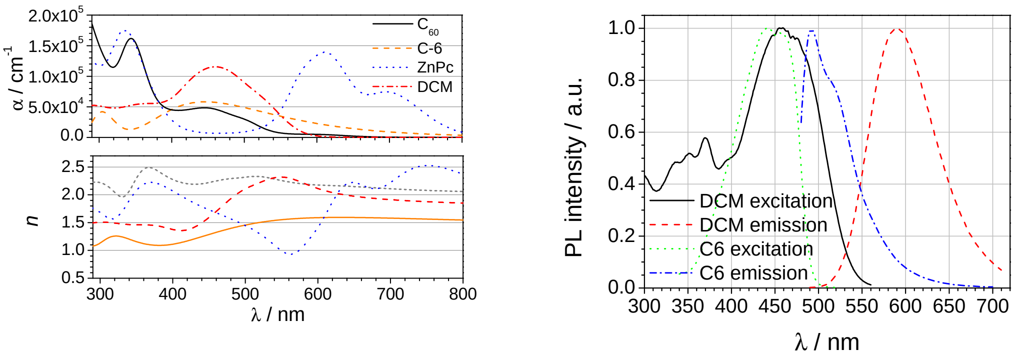

(a) (b)

Figure 4.1: (a) Optical constants α and n of 100 nm C_{60}, 100 nm ZnPc and 50 nm C6 and DCM as well as (b) the PL charactersitics of C6 and DCM dissolved in THF.

HJ photovoltaic cells, for example such as 2,3,7,8,12,13,17,18-octaethyl-21*H*,23*H*-porphyrineplatinum(II) (PtOEP).[56]

Figure 4.1 a shows the absorption coeffcients α and the refractive indices n of pure C6, DCM, ZnPc and C_{60} layers. Figure 4.1 b shows the highly fluorescent properties of C6 and DCM solutions under UV excitation. Although ZnPc is a good absorber for UV-light in the region between 550 and 750 nm, it is not suitable to harvest the light from 380 to 550 nm. So, the energy of this light is usually lost for solar cells built up with C_{60}:ZnPc blended absorption layers. Solid C6 and DCM show a strong absorption in that range and are widely known to be strong emitters in the orange to red region of light, where the Q^+ band transitions of ZnPc can be excited.

This chapter will discuss two different approaches, to show that emitter compounds can also contribute to the power efficiency of OSC and that their application should not only be restricted to organic light emitting devices. The first part focuses on the utilization of a strong emitter, here C6, as a donor material with low PL quantum efficiencies in pin-BHJ-OSC based on small molecules to yields devices with a high spectral sensitivity that are able to compete with classical silicon based photodiodes. For the second part, the emission strength of DCM will be used to increase the overall spectral sensitivity of C_{60}:ZnPc based BHJ solar cells by converting the filtered UV-irradiation of sunlight.

4.1 Coumarin 6 and its Use as Donor Material

Coumarin derivatives have recently been used for a wide range of photovoltaic applications, in particular as sensitizer for dye-sensitized solar cells (DSSC) [129,130] or to improve the spectral coverage for MEH-PPV based bulk heterojunction solar cells. [131] Although, many photophysical properties were determined in the past. Iijima *et al.* more recently investigated in the late 80s the photovoltaic properties of C6 as well as other derivatives and showed their suitability for photocells as p-type semiconductors. [134] Much later, Meixner and co-workers have successfully introduced C6 into phototransistors, yielding a higher conductivity of the host material and achieving a higher spectral response close to the wavelength region where C6 absorbs strongly. [135] In 2010, C6 was introduced as a donor material in bulk heterojunction solar cells together with PCBM as acceptor. [132,133] The layers of this device were fabricated by solution-based processes and have been intensively studied. It turns out, that C6 is more affected by annealing steps than PCBM. However, the power efficiency of the best cell yielded only 0.19%, accompanied by low J_{SC} (1.6 mA/cm^2), FF (37%) and V_{OC} (340 mV). These values have been explained due to the low conductivity properties of C6, although no absolute values for the charge carrier conductivity or mobility have been published. Further studies have revealed the existence of subband transitions and the efficiency has been improved to 0.22%. [133]

Here, we plan to introduce the coumarin 6 molecule as a donor in BHJ organic solar cells because of the aforementioned properties. We believe that higher efficiencies than 0.3% can be achieved for organic BHJ solar cells, in particular based on small molecules. In order to reach this goal and to obtain a better understanding, firstly the absorption layer composition and its thickness will be modified (and cells characterized), and then the HTL material will be varied.

4.1.1 The Content of Coumarin 6

The emission and excitation spectra of C6 in solution and as a pure thin film are shown in figure 4.1 b and 4.2 a, respectively. In the solution based spectrum, a structured excitation band from 430 to 460 nm can be observed. The emission band is less structured with a main peak at 475 and a shoulder at 530 nm. With respect to the thin film sample, both the excitation and emission spectrum are hypsochromatically shifted probably due to stack type interactions [136] and the emission is broadened and shows peaks at 358, 380 and 440 nm. The excitation maximum could not be determined because it lay beyond the corrected detector sensitivity (240 nm). It follows that the Stokes shift of the thin film samples is higher than for the diluted samples in solution. Because the concentration of singlet

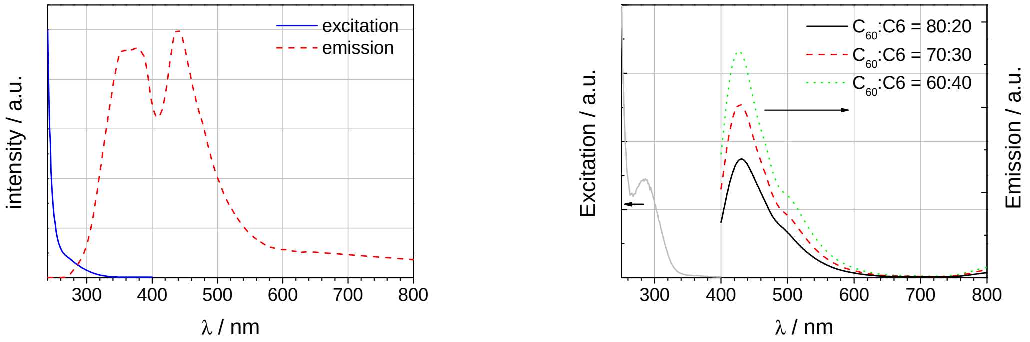

(a) (b)

Figure 4.2: Photoluminescence spectrum of (a) a pure 80 nm thick C6 film and (b) of C_{60}:C6 films excited at 295 nm in dependence on their composition.

states is very high in the pure film,[137] singlet-singlet annihilation occurs, which reduces the PL intensity and complicates the analysis of the emissive properties.

The excitation and emission spectra of the C_{60}:C6 mixed layers are presented in figure 4.2 b. Whereas no excitation maximum has been detected till 240 nm for the pure C6 film, a small maximum can be found at 286 nm for the C_{60}:C6 mixture. The emission spectrum of the blend looks similar to the pure film. With increasing C6 content, the emission intensity rises. However, in presence of the fullerene C_{60}, the emission of C6 was quenched and hardly detectable, which shows the enormous acceptor strength of C_{60}. Thus, C_{60} can be used to investigate the exciton diffusion length L_D via photoluminescence measurements adapted from literature.[57,138] A layer of thickness d is assumed to have a quenching interface (C6/C_{60}) and the other is nonquenching (C6/glass). If the film is sufficiently thin ($d < \lambda/2n$)[3] and absorption effects ($d < L_D$) are negligible, then a uniform exciton generation rate throughout the thin film can be assumed. The fraction of excitons reaching the interface is hence η_{ED} = 1- PL_1 (with quencher)/PL_2 (without quencher). By fitting these data with

$$\eta_{ED} = \frac{L_D}{d} \frac{[1 - exp(L_D/2d)]}{[1 + exp(L_D/2d)]} \tag{4.1}$$

L_D can be obtained. The measured data and its plot are depicted in figure A.1 a. It has to be noted that the reproducibility of this measurement is poor since the emission properties of the samples changed from batch to batch. This can be explained by the tendency of C6 to crystallize and to form aggregates which seem to change as the layer thickness is increased. The transition from transparent to scattering samples could not be controlled. The results have been used for which the exciton diffusion length had the smallest deviation of 11.8 ± 0.3 nm.

Since the emission of C6 is quenched in the presence of C_{60}, C6 can be used as

---

[3] n as the real part of the index of refraction.

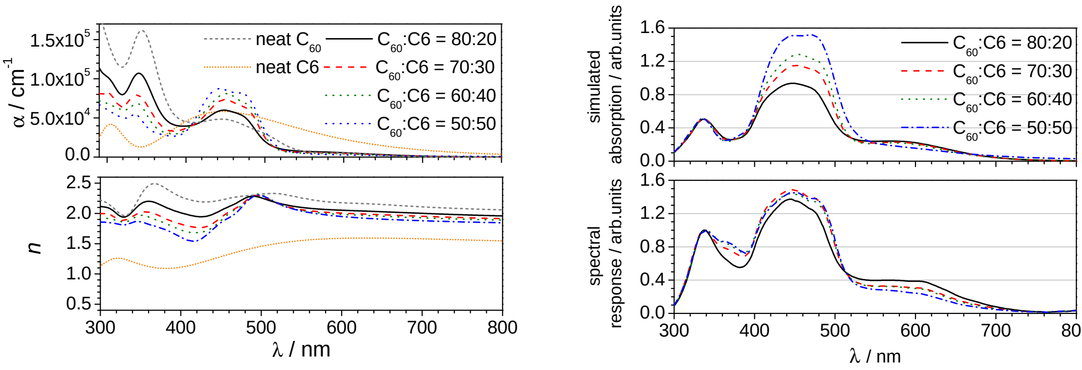

(a) (b)

Figure 4.3: (a) Absorption coefficients α (top) and refractive indices n (bottom) of C_{60}:C6 films for changing compositions as well as (b) spectral response measurements (bottom) varied by the AL composition and the corresponding simulated absorption behavior (top) of the single ALs within the solar cell.

an absorber material for photovoltaic applications. Figure 4.3 a shows the optical constants α and n of different donor acceptor mixtures and the pure materials. Because C6 highly has a strong tendency to crystallize, the pure film was characterized by strong scattering. Thus, the analysis of the refractive indices and absorption coefficients was difficult and resulted in a higher MSE value. After blending C6 with C_{60} a smooth and transparent film was obtained, showing that C_{60} inhibits the crystallization of C6.

The absorption spectrum of C_{60} has strong transitions at 344 nm (1.62×10^5 cm^{-1}) and 445 nm (4.85×10^4 cm^{-1}). On the other hand, C6 shows a strong absorption band at 446 nm (5.82×10^4 cm^{-1}), which will result in a large overlap for the bicomponent C_{60}:C6 system. The spectra of the different mixtures are characterized by these bands as well. When reducing the amount of C_{60}, the band maximum shifts hypsochromically from 344 to 338 nm, probably due to stack type interactions.[136] The location of the absorption band rises with increasing amounts of C6 and shifts bathochromically from 445 to 451 nm. Noteworthy is the fact that the absorption coefficients between 445 and 451 nm are higher for the mixtures than for the pure materials; that might result from a better molecule orientation in order to interact with the electric field. The refractive indices (*cf.* figure 4.3 a, bottom) of the mixed layers are strongly influenced by C_{60}. Absolute values and shape are similar to the pure C_{60} film.

In order to achieve efficient photodiodes, the stack has been optimized for different aspects. Depending on the charge carrier mobility and the exciton diffusion length, the absorber layer constitution may have a large influence on the performance. Therefore, several diodes with different donor-acceptor mixtures have been processed while keeping the other layers unchanged. The results of this are summarized in table 4.1.

Table 4.1: Key parameters of the photodiodes[a] in dependence on the absorption layer composition.

C_{60}:C6	80:20	70:30	65:35	60:40	50:50
ϵ_r	4.6	4.4	-	4.3	-
$\sigma \times 10^{-10}$/ S cm^{-1}	10.0	7.08	-	6.42	-
V_{OC} / mV	566.0	599.9	623.6	654.6	682.9
J_{SC} / mAcm^{-2}	5.56	5.99	5.43	4.83	4.30
FF / %	42.8	41.4	40.8	36.8	36.8
η / %	1.35	1.50	1.38	1.17	1.08
S	1.35	1.27	1.24	1.28	1.33

[a] Glass / 130 nm ITO / 1 nm NDP-9 / 50 nm p-spiro-TTB / 35 nm C_{60}:ZnPc / 20 nm C_{60} / 5 nm n-C_{60} / 200 nm Al.

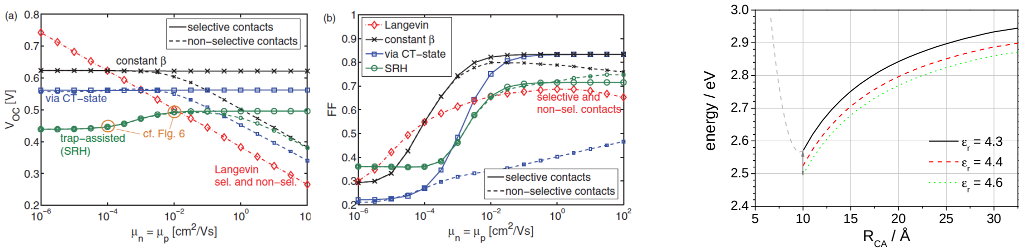

(a)

(b)

Figure 4.4: (a) V_{OC} and FF as a function of the charge carrier mobility $\mu_n = \mu_p$ for different recombination models reproduced from reference[74]. The red graphs present the behavior for mobility dependent recombination constants β proposed by the Langevin theory. (b) CT energy in dependence on center to center difference R_{CA} for the evaluated ϵ_r values.

Obviously, all parameters are affected by the donor:acceptor ratio, this has also been reported in the literature for other D:A compounds.[68,73] The V_{OC} rises with increasing amounts of the C6. Since the origin of V_{OC} is still under debate, several possible explanations will be discussed now. A variation of the Fermi-level splitting due to a shift of the HOMO or LUMO levels could be a reason for the change in V_{OC}. Generally, V_{OC} scales with the effective gap, which is the difference between the LUMO of the acceptor and the HOMO of the donor. As discussed by Tress and co-workers for C_{60}:ZnPc blended absorption layers, the variation of the D:A ratio yielded a shift of the blend HOMO and thus, a V_{OC} adjustment.[68] Although a very similar pin-architecture has been applied, the HOMO shift resulted there in higher extraction barriers which can strongly effect the Fermi-level splitting and hence, V_{OC} of the cell. However, for our example we can exclude a LUMO shift of C_{60} since a replacement of the pure C_{60} showed no effect on V_{OC}, too. If lowering of the C6 HOMO level with increasing C6 content is considered, only injection barriers will be enhanced, which will not affect the V_{OC} according to drift-diffusion simulations.[15]

Another reasonable explanation is provided by the mobility dependent recombination given by the Langevin theory which proposes, for decreasing charge carrier mobilities, a drop in FF and a rise of V_{OC}, *vide* figure a. 4.4. However, this has never been experimentally proven so far for small-molecule solar cells, although it would be in very good agreement with the results presented here.[74] Finally, a correlation between the charge transfer (CT) states and V_{OC} is considered, as described by Deibel and co-workers.[139] After light absorption, a singlet exciton is formed on the donor and can diffuse towards the donor-acceptor heterojunction, where it can dissociate by performing a charge transfer, if the energy of the CT complex is lower than the energy of the singlet exciton given by the optical absorption gap. Using the equation for the Gibbs free energy of photoinduced electron transfer, it has been shown that the charge transfer energy (E_{CT}) stabilizes with higher dielectric permittivities ϵ_r and thus, V_{OC} decreases.[140] For an estimation of the ϵ_r influence on the CT energy, this relation has been used:

$$E_{CT} = e\left[E^0(D/D^+) - E^0(A/A^-)\right] - Z\left(\frac{1}{\epsilon_{ref}} - \frac{1}{\epsilon_r}\right)\left(\frac{1}{r^+} + \frac{1}{r^-}\right) - \frac{Z}{\epsilon_r}\frac{2}{R_{CA}} \quad (4.2)$$

with $Z = e^2/(8\pi\epsilon_0)$, 1.02 eV as oxidation potential for C6,[141] -1.3 eV as reduction potential for C_{60}[142] determined in acetonitrile ($\epsilon_{ref} = 35.9$), a radius of the cation $r^+ = 4.5$ Å and a radius of the anion $r^- = 5.6$ Å, as used in reference[140].

With increasing C6 amount, the relative dielectric constant decreases from 6.6 (20% C6) to 6.3 (40% C6) which results in higher CT energies. Thus, the loss with regard to $e{\cdot}V_{OC}$ lowers and V_{OC} increases. The reduction of ϵ_r from 4.6 to 4.3 results in a difference of about 80 mV, which is in very good agreement with the V_{OC} difference (90 mV) of these samples. A similar behavior for polymeric blends of a fluorine copolymer (PF10TBT) and a fullerene derivative (PCBM) have been observed by Veldman and co-workers.[140]

Whereas the open circuit voltage increases almost linearly, the fill factor decreases with rising C6 content. Additionally, the short circuit reaches its maximum at a C6 content of 30% with 5.99 mA/cm^2 which results in a maximum efficiency of 1.50%. The higher the C6 concentration in the absorption layer, the more strongly photons can be absorbed by C6 as shown in figure 4.3 a. In order to interpret the SR-measurements, the absorption behavior of each absorption layer has been simulated considering the interfaces of the stacked photodiode, as presented in figure 4.5 a. The peaks at 338 and 450 nm can be assigned both to C_{60} and C6. The shoulder appearing at 600 nm seems to correlate with C_{60} since it decreases with falling C_{60} content. For better comparison, the spectra are both normalized to the first peak. According to the simulation, the absorption of the second peak is supposed to increase strongly with rising C6 amount. However, with respect to

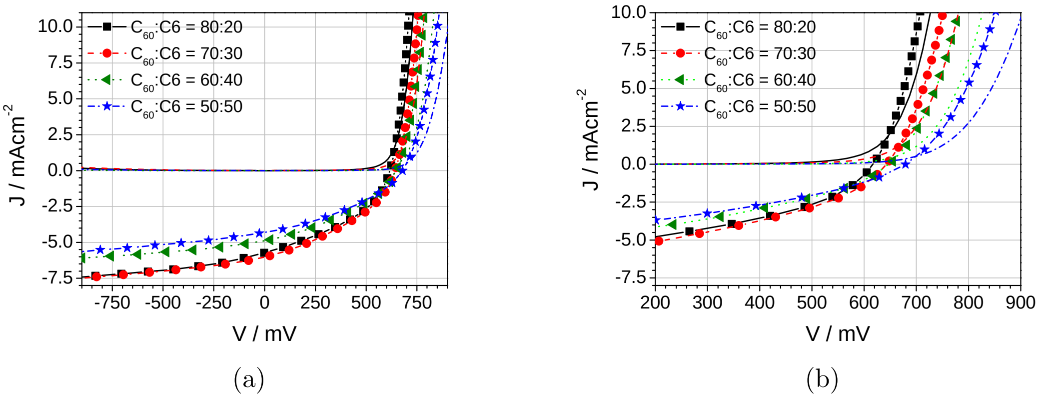

(a)

(b)

Figure 4.5: (a) J-V curves of illuminated (line + symbol) and darked (line) organic solar cells in dependence on the absorption layer composition as well as (b) its detailed presentation.

the measured SR-spectra the ratio of the first two peaks (340, 465 nm) is hardly affected by the composition, whereas the shoulder (610 nm) rather shrinks. Although the absorption strength at 465 nm is large and many excitons are formed, only a limited number of free charge carriers reach the transport layers. The excitons recombine before they reach the interface or the released free charge carriers are trapped and recombine. This observation is supported by the fact that the peak ratio remains rather equal. Recombination rates are high if the exciton diffusion length, the exciton lifetime and/ or the charge carrier mobility within the blended layer is too low. A disturbance of the percolation network influenced by the morphological properties of C6 can also explains the low *FF*.

Figure 4.5 shows the J-V curves of the different diodes under illumination and in the dark. The series resistance has to be discussed under two aspects: with and without the photoconductivity. In the dark, the R_S rises with increasing amount of C6. Since the overall thickness of the absorption layer remained constant, the rising R_S can be attributed to defects at the D/A interface or to the poor conductivity of the polycrystalline molecular film. A decreasing conductivity with rising C6 content has also been determined for the blend from the impedance measurements. Changing the content from 20 to 40% of volume fraction, reduces the conductivity from 10.0 to 6.42×10^{-10} Scm^{-1}. Although under illumination a distinct photoconductivity can be observed for all samples, its extent becomes more distinct the higher the content of C6. Nonetheless, the photoconductive properties cannot compensate for the rise of the series resistance due to traps or barriers. The saturation and thus, the R_P seem to not be affected by the composition. Summarizing, the charge carrier separation and/ or the charge transport towards the electrodes are disadvantageously influenced by the low charge carrier mobility of C_{60}:C6.

However, a reduction of the absorption layer thickness should result in improv-

Table 4.2: Key parameters of the C_{60}:C6 containing organic solar cells[a] in dependence on the absorption layer thickness.

d_{AL} / nm	V_{OC} / mV	J_{SC} / mAcm^{-2}	FF / %	η / %	S
35	619.6	5.43	40.9	1.38	1.24
30	619.8	5.17	43.1	1.38	1.26
25	621.9	5.17	43.4	1.39	1.27
20	615.7	4.62	47.1	1.33	1.35

[a] Glass / 130 nm ITO / 1 nm NDP-9 / 50 nm p-spiro-TTB / C_{60}:C6 = 7:3 / 20 nm C_{60} / 5 nm n-C_{60} / 200 nm Al.

ing fill factors. Therefore, samples with different thicknesses were processed using the AL constitution, for which the photodiodes yielded high efficiencies with a moderate amount of C6 (35%).

4.1.2 Layer Thickness Variation of C_{60}:C6

In order to improve the *FF*, samples with absorber layers of different thicknesses have been prepared using the wedge tool. This procedure ensures a good comparability of the different samples since the other layers remain unchanged.

However, another issue has to be taken into account when decreasing the AL layer. When changing the absolute thicknesses of layers, the maximum field amplitude of the incident light changes its location due to interference effects. For excellent photon harvesting this maximum must be placed in the AL. Whereas a modification of the HTL thickness affects hardly the position of this maximum, the overall thickness of each the AL, the BL and the ETL influences strongly the absorption efficiency of the AL since the non-absorbed light is reflected at the cathode. Figure 4.6 a depicts the absorption efficiency's dependence on the AL and ETL thickness considering the stack architecture referred to in table 4.2. Keeping the ETL thickness fixed at 10 nm with variation of the AL height results in distinctively different absorptions for the incident light. A thicker AL thickness must be compensated with a thinner ETL in order to gain the highest absorption. The two figures also show that the absorption spectrum normalized to 465 nm differs from the solar integrated absorption (SIA) since each wavelength interferes differently in the stack.

Figure 4.7 presents the J-V characteristics of the aforementioned samples under illumination and in the dark. The key values of these curves are summarized in table 4.2. Whereas the V_{OC} is unaffected by the decrease of the AL thickness, the fill factor increases from 40.9% to 47.1% by reducing the AL from 35 to 20 nm. At the same time J_{SC} decreases from 5.43 to 4.62 mAcm^{-2}, which is a remarkably small difference considering that the height of the AL was nearly halved. This observation indicates that a large part of the excitons formed in the thick layers

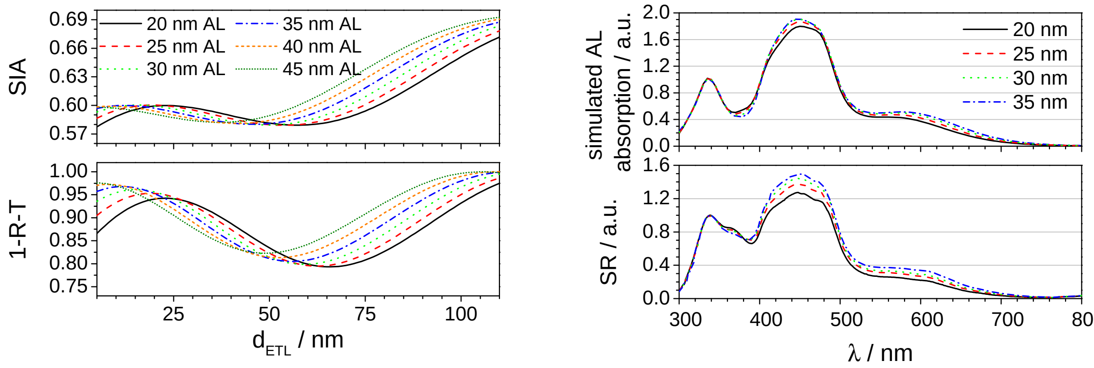

(a) (b)

Figure 4.6: (a) Simulated absorption intensities with respect to 465 nm (bottom) and the AM 1.5 solar spectrum (top) *versus* ETL thickness for different AL thicknesses using the optical simulation software Setfos. (b) Spectral response measurements (bottom) and the simulated absorption (top) of the AL for various thicknesses.

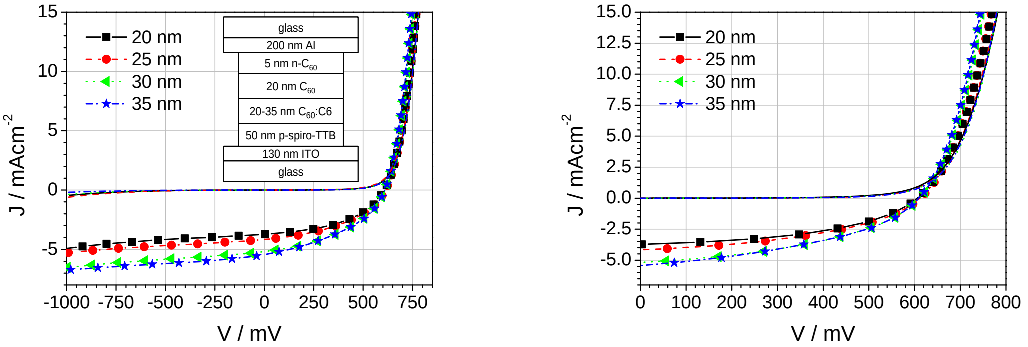

(a) (b)

Figure 4.7: (a) J-V curves of organic solar cells under illumination (line + symbol) and in the dark (line) for various AL thicknesses as well as (b) its enlargement.

can not contribute to the photocurrent due to recombination processes. On the other hand, a J_{SC} value of 4.71 mAcm^{-2} for a 20 nm thick AL emphasizes the strong absorption characteristics of the C6 molecule.

With respect to the shape of the J-V curve (*vide* figure 4.7), the reduction of the AL height has no influence on the R_S value, neither under illuminated nor dark conditions, which means that the interfaces remained unchanged. The rise of the saturation from 1.24 to 1.35 rather indicates that the shunt resistances and leakage currents increase with thinner AL due to the thinner total stack, in which the roughnesses of the elctrodes can begin to significantly affect the parallel resistance R_P. Another concomitant phenomenon of reducing the AL height is that the dark current increases and therefore the diode ideality worsens, as depicted in figure 4.7 a. This can be explained by a reduction of the effective barrier height due to multi-step tunneling and image forces.[40] Nevertheless, an improvement of

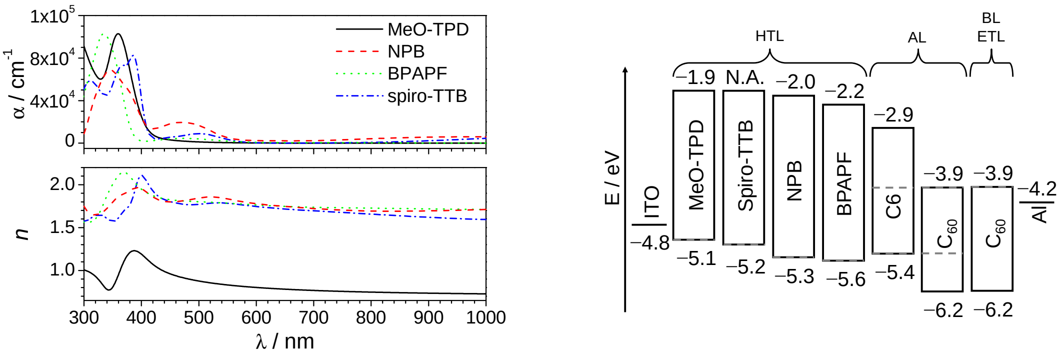

(a) (b)

Figure 4.8: Optical constants of the determined HTL-materials (a) and (b) the HOMO and LUMO energy levels of the investigated HTL materials.

the fill factor is caused by the reduction of the AL because less recombination of the charge carriers occurs.

4.1.3 Variation of the HTL-Material

Transport materials are important to ensure an efficient charge carrier collection from the absorber layer by electrodes. If the optical properties are comparable and the energy levels of the molecular orbitals are similar, in theory a replacement of the transport materials should have a low impact on the photo-cell performance. In comparison to PHJ solar cells having pure absorbing thin films, the exciton- and charge transport properties are altered after the formation of a BHJ network. Phase separation and film morphology of blends have more important roles than for pure materials. Many examples have been reported where the aforementioned characteristics have a huge influence on key values such as the V_{OC}.[35] Hence, different compounds such as *N,N'*-di(naphthalen-1-yl)-*N,N'*-diphenyl-benzidine (NPB), *N,N,N',N'*- *tetrakis*(4-methoxyphenyl)-benzidine (MeO-TPD), 2,2',7,7'-tetra(m-tolyl-phenylamino)-9,9'-spiro-bifluorene (spiro-TTB) and 9,9-*bis*-4-[di-(p-biphenyl)-aminophenyl]-fluorene (BPAPF) have been used as HTL material to study such effects. Their optical properties are presented in figure 4.8 a.

The stack information and energy levels of the materials used were taken from the literature (*cf.* table 2.1) and are depicted in figure 4.8 b. Because not all HTL-materials could be varied within one processing run, each substitution of a HTL material was carried out with a reference sample (spiro-TTB). The conductivity of all HTL layers was set to 10^{-5} S/cm with p-type dopants NDP-2 (spiro-TTB, NPB, MeO-TPD) or NDP-9 (spiro-TTB, BPAPF) and the thickness was kept equal to neglect interference effects. The C6 content in the AL was set at 35%.

The results of these experiments are summarized in table 4.3 and show a distinct variation of the key values as a function of the HTL material. Because the electron

Table 4.3: Key parameters of the photodiodes in dependence on the HTL material.

HTL (Run)	V_{OC} / mV	J_{SC} / mAcm^{-2}	FF / %	η / %	S
MeO-TPD (A)	571.3	5.48	38.9	1.22	1.34
spiro-TTB (A)	620.7	5.58	41.8	1.45	1.20
NPB (B)	731.8	4.87	40.5	1.44	1.36
spiro-TTB (B)	621.2	5.14	42.6	1.36	1.26
BPAPF (C)	850.5	6.05	36.1	1.87	1.16
spiro-TTB (C)	647.5	5.76	41.2	1.54	1.18

Glass / 130 nm ITO / 1 nm NDP-9 / 50 nm p-spiro-TTB / C_{60}:C6 = 7:3 / 20 nm C_{60} / 5 nm n-C_{60} / 200 nm Al.

mobility in C_{60} is higher than the hole mobility, holes are concentrated near the HTL/AL interface and recombine. Depending on the morphology, the mobility may change due to crystal packing and resulting defects. AFM images of MeO-TPD (a), NPB (b), BPAPF (c), spiro-TTB (d) and the following AL are presented in figure 4.10. However, a clear correlation between the surface roughness of the HTL and the resulting AL and J_{SC} could not be drawn given the investigated area of 1 × 1 µm^2. The consecutive AL material seems to grow smoother than the HTL layer.

Another interesting aspect is presented in figure 4.10 a with the SR spectra (bottom) and the simulated absorption behaviour (top) of the AL. With respect to the SR measurements, the shape of the graphs varies enormously from 300 to 400 nm, bearing in mind that the AL composition has been kept equal for all samples. Since the peak at 340 nm is missing for the BPAPF containing photodiode, the spectra have been normalized to the C6 peak at 450 nm. For comparison, the absorption behavior of the AL has been simulated. Here, the incoupling of the incident light is significantly affected by the optical properties of the underlying HTL material, in particular in the region from 300 to 400 nm. According to the simulated spectra, the C_{60}-related absorption at 320 nm can be assigned in all simulations, either as a peak or a shoulder (BPAPF). In the measured SR spectra only those of MeO-TPD and spiro-TTB reveal this aforementioned peak. Regarding NPB and BPAPF this peak disappears in the background of stronger and new peaks at 365 nm (NPB) and 380 nm (BPAPF). The band at 365 nm (NPB) can also be assigned in a structured shoulder in the spiro-TTB sample. With respect to the main band at 450 nm, except for NPB the shape is similar. With NPB a distict peak at 475 nm can be located. The shoulder from 500 to 700 nm looks similar for all samples, which is expected except for MeO-TPD. According to the simulation, the light incoupling should be stronger in the range from 500 to 600 nm.

Since the differing shape of the SR spectra can not be explained by transitions occuring according to the simulated absorption spectra, the interface HTL/AL

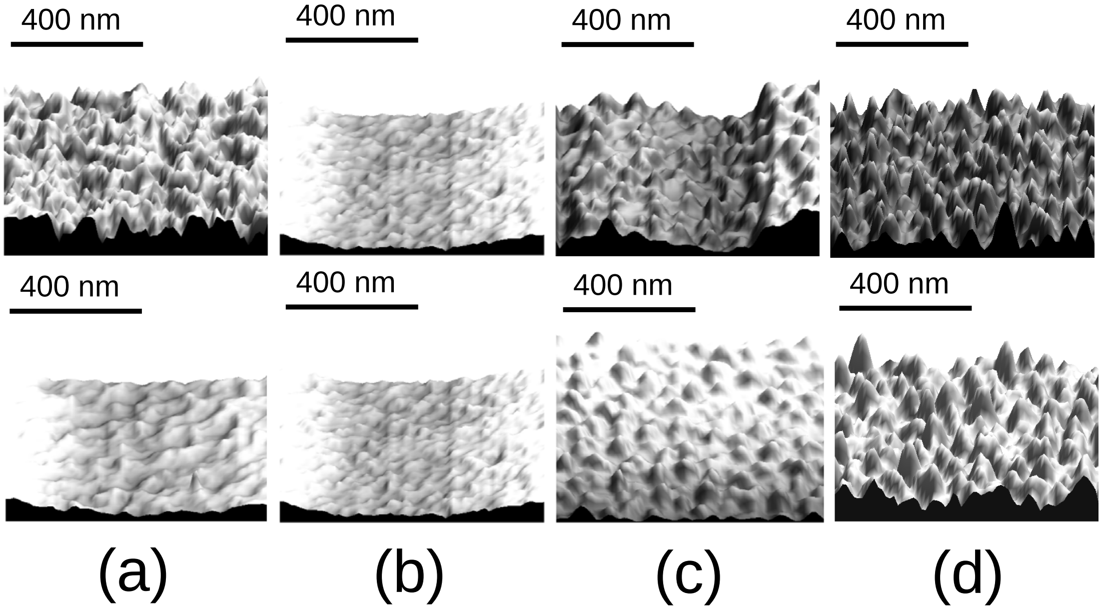

Figure 4.9: AFM images of the AL (bottom) deposited on the different HTL-materials (top), such as MeO-TPD (a), NBP (b), BPAPF (c) and spiro-TTB (d).

seems to have a pronounced impact on the active layer absorption and thus, on the generated photocurrent. Similar effects have been observed with C6:PCBM layers deposited either on glass or ITO covered glass. On ITO covered glass samples, subband transitions of low energy have been observed in the region 520 - 800 nm and were associated with an increase of the total photocurrent.[132] Nevertheless, we believe that the emission properties of the different HTL materials are responsible for the shape of the SR spectra from 300 to 400 nm. Figure 4.10 b shows the PL spectra for each material for different excitation wavelengths.

The excitation wavelength was varied from 290 to 350 nm in order to investigate the resulting change in the emission profile. Excitation at 290 nm resulted, for all HTL materials, in similar broad emission from 350 to 550 nm without any specific features. The emission maximum for all materials was located at around 440 nm. That means that the main part of the PL spectra overlaps with the absorption maximum of the AL originating from C6 transitions (415 - 500 nm, *cf.* figure 4.3 a.) With increasing excitation wavelength (in direction of arrow) the emission intensity at 440 nm decreases and new bands arise. For clarity, these bands are also marked with an arrow. From MeO-TPD (418 nm), spiro-TTB (408 nm), BPAPF (392 nm) to NPB (378 nm) the location of this band varies systematically with rising excitation wavelength. With the reduction of this emission wavelength, absorption at the band 330 - 365 nm (originating from C_{60}) becomes more probable. Besides the variation of the emission profile, the PL quantum efficiencies also differ for each material and thus the emission intensity. Because the Förster energy resonance transfer only works for distances smaller than 15 nm, most of the emission energy

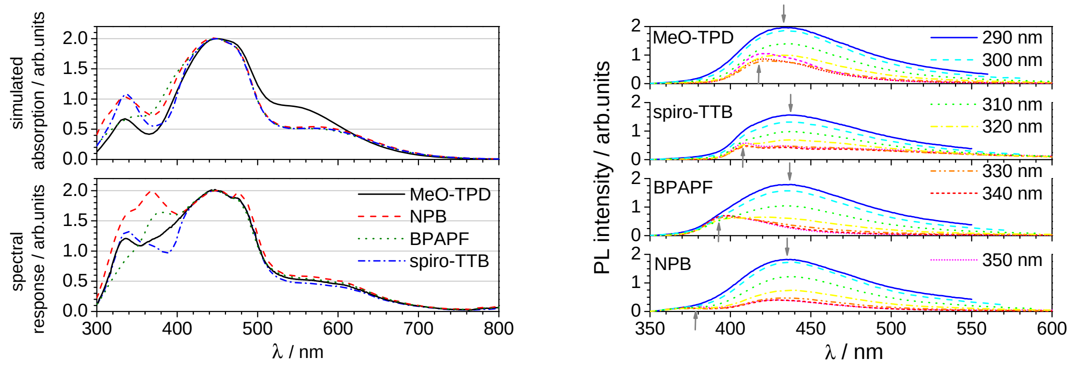

(a) (b)

Figure 4.10: (a) Spectral response measurements (bottom) and the simulated absorption (top) of the AL in variation of the HTL material and the emission spectra of MeO-TPD, spiro-TTB, BPAPF and NPB excited at various wavelenghts λ_{ex}.

can not be absorbed by the AL since the HTL has a thickness of 50 nm. Moreover, there is still the unanswered question of whether the blue emission originating from the HTL can be absorbed effectively within the stack. Nonetheless, the impact of the HTL material on the photocurrent has been sufficiently large to detect it and should be taken into account for solar cell device architectures.

Besides the variation of the short circuit current, the open circuit voltage is even more effected by the underlying surface. The V_{OC} value ranges from 571.25 mV (MeO-TPD) to 850.53 mV (BPAPF). Here, the V_{OC} is higher, the lower the HOMO level of the HTL material is.

With variation of the HTL materials, injection as well as extraction barriers for holes at the HTL/AL interface have been realized. An injection barrier is formed if the HOMO of the HTL lies higher than the HOMO of the donor since the holes experience an energy barrier passing from the ITO via the HTL to the donor. Extraction barriers occur for (photogenerated) holes in the donor layer if the destination layer possesses a deeper HOMO layer. For BHJ solar cells using the stack architecture applied in this work, Tress and co-workers reported that V_{OC} is strongly influenced by the HOMO of the HTL. If the HOMO of the HTL is higher than the the HOMO of the donor (injection barrier), the HOMO of the HTL will limit the V_{OC} and the HOMO of the donor will become irrelevant.[15] The quasi-Fermi level splitting in the blend is reduced towards the HTL/blend interface because of the high concentration of holes delivered by the anode leading there to an increased recombination probability of electrons and holes. Hence, eV_{OC} is only the difference between the hole quasi-Fermi level at the anode and the electron quasi-Fermi level at the cathode and does not reach the maximum quasi-Fermi level splitting in the absorber.

Besides the correlation between the HOMO level and V_{OC}, the V_{OC} is higher the lower the dark current at 0 V is or vice versa. This analogy has been reported

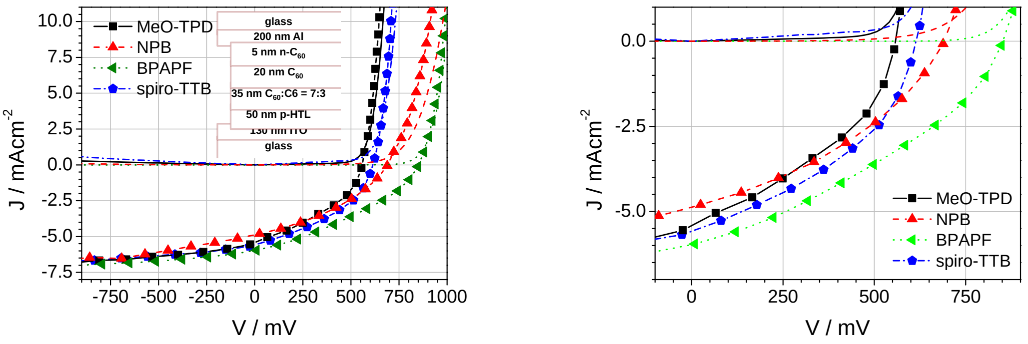

(a) (b)

Figure 4.11: *J*-*V* curves of illuminated photodiodes in dependence on the HTL material as well as (b) its detailed presentation.

by Li and co-workers, who showed the connection between the dark saturation current and the open circuit voltage.[24] Concerning the dark current curve, the diode ideality appears to correspond to the V_{OC}, too. This might be ascribed to the fact that with rising V_{OC} the HOMO level of the HTL is closer to the HOMO of C6 (5.4 eV). Thus, barriers are reduced and exciton separation is favoured.

Temperature Dependency during Fabrication

Since it is known that heating the substrate during deposition and post-annealing can have a positive influence on the morphology and thus on the mobility, the substrates of the photodiodes have been heated as well during deposition. In order to estimate the substrate temperature, the thermal properties of C6 have been determined. For C6 a melting point T_m of 207.6 ℃ and a glass transition temperature T_g of 83.9 ℃ have been measured. Substrate heating until 150 ℃ and post-annealing of the samples to a temperature of 200 ℃ showed no improvement of the photodiode performance.

4.1.4 Summary and Outlook

Using C6 as donor material, devices have been achieved with the highest efficiency (1.87%) ever reported for HJ organic solar cells under AM1.5 illumination. However, the *FF* was unsatisfactory (36 to 42%) for various configurations, which will inhibit the implementation of this binary system C_{60}:C6 in tandem devices or similar. The spectral sensitivity in the blue region of light has been remarkable and applications can be realized where the overall power efficiency is not targeted, such as for sensors detecting high energy photons in the visible range of light. Considering this, a comparison of the spectral responsivity between classical silicon based photodetectors and these organic photodiodes using C6 as s sensitizer shows that these organic photodiodes are more sensitive between 300 to 500 nm. This spectral region is especially important for the detection of emission originating from scintillators that react to energetic particle radiation. Therefore, lifetime investigations and temporal response measurements should be carried out in order to assess the applicability of these photodiodes.

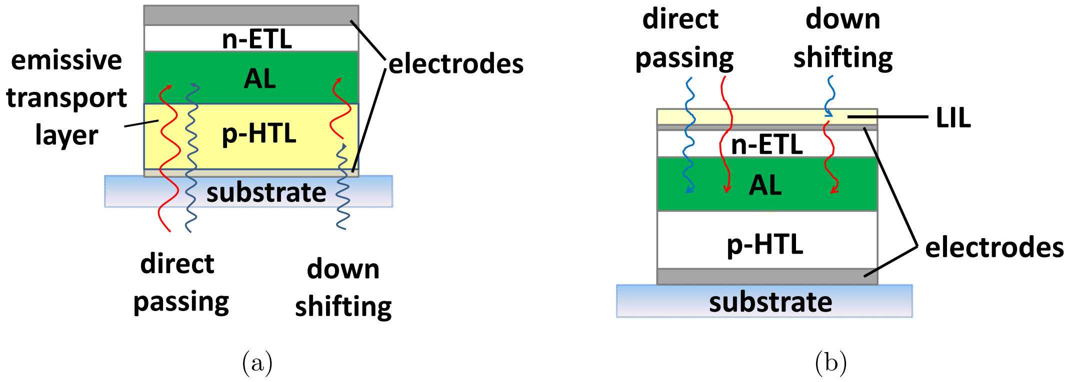

(a) (b)

Figure 4.12: Schematic representation of tow suggested approaches to integrate emitting layers in the stack architecture of organic solar cells. (a) shows the insersation of an emitting transport layer and (b) the application of an emitting light incoupling layer (LIL).

4.2 DCM as Energy Down-Shifter in OSC

Using photon conversion processes to positively influence the absorption behavior is a common approach in the field of inorganic photovoltaics due to the discrete band structure of inorganic semiconductors. Photon conversion processes aim to convert (*via* luminescence) the solar spectrum to better match the absorption properties of a semiconductor device. 'Multi-photon' mechanisms such as up-conversion as well as down-conversion, and single-photon processes like down-shifting can be used to achieve this goal.[79,143] Because the suitability of DCM as a donor material in BHJ solar cells has already been verified by Wang et al.,[35] the excellent fluorescent properties of this emitter will be exploited to study the concept of inner-down-shifting of the solar light for organic solar cells. The aim is to modify the absorption profile of binary C_{60}:ZnPc BHJ solar cells by utilizing the emission strength of DCM in the range between 580 to 780 nm. DCM will be inserted either in the p-doped hole transporting layer or in the light incoupling layer (LIL) in order to absorb light and to convert it to lower energy radiation. That the emissive properties of the HTL can be used to influence the absorption profile of OSC has already been shown in the previous section for C_{60}:C6 based organic solar cells.[144] Several HTL materials have been used and a correlation between the HTL emission profile and the spectral sensitivity profiles have been noted[4].

Converting light of higher energy to lower energy by down-shifting is accompanied by a loss of photon energy and will result in a high degree of heating of the semiconductors due to the Stokes shift.[79] However, this heating has to be dealt with for classical inorganic solar cells since the efficiency of these cells decreases at higher temperatures. This dependency of efficiency upon temperature

---

[4] Because of the donor C6, the sensitivity for blue light has been very high for this device architecture, which has been well matching with the blue emission of transparent HTL materials.

is reversed for organic solar cells.[9,76,145] So, the introduction of a down-shifting emitter molecule does not just convert the solar spectrum, it also heats the cell from the inside. For our investigations the down-shifting emitter DCM is placed in a layer within the optoelectronic device. When discussing the results of this study, several aspects should be considered:

- The emission profile of the down-shifter is supposed to overlap with the absorption profile, whereas its excitation and absorption profile must not compete with the absorption profile of the donor material. DCM is known to strongly emit reddish light and to absorb between 400 and 520 nm, whereas ZnPc is a red absorber, but weak in the green region of light.
- The addition of a third component into a doped HTL might influence its conductivity or the energy level of the HOMO. Furthermore, adding another material might result in parasitic absorption.
- Since singlet excitons are able to quench themselves due to aggregation, an optimum doping concentration of DCM in the designated layer has to be determined.
- The FRET works only up to a maximum distance of approximately 15 nm. Due to the thickness of at least 50 nm of the doped p-HTL, not all the emission from this layer will be transported by energy transfer. If the emission is too far away, its excited state will either be quenched or radiatively decay, emitting a photon that may or may not find its way to an energy acceptor. Furthermore, when locating this emissive zone within an optoelectronic device, it can not be treated as coherent light source. This means that is it not possible to simulate the light incoupling of the red emission with the usual software tools such as Setfos.[78]
- The efficiency of the down-shifting approach is determined by the luminescence quantum efficiency of the emissive species, the waveguide losses and the reabsorption within the waveguided material. Since the emissive layer is isotropic, this efficiency will be much lower than unity.

4.2.1 Evaluation of the DCM Doping Concentration

With spiro-TTB as HTL Material

DCM has been doped into the hole transporting material spiro-TTB. For processing reasons, the 80 nm thick HTL has been doped with NDP-9, where a doping concentration of only 3% is necessary to reach conductivities of 10^{-5} S/cm. The values obtained are summarized in table 4.4. Clearly, the conductivity of the HTL

Table 4.4: Influence of DCM on the properties of the HTL spiro-TTB doped with 3% NDP-9. The thin film has been prepared on CE glass.

c_{DCM} / %	σ / $\times$ 10^{-5} Scm^{-1}	$T_{\lambda=506\rightarrow493nm}$	$T_{\lambda=605nm}$
0.0	5.6	0.80	0.87
0.1	5.2	0.80	0.86
0.2	5.7	0.80	0.86
0.4	5.1	0.79	0.86
0.8	5.9	0.77	0.85
1.7	4.4	0.76	0.85
3.3	3.6	0.71	0.84
6.5	2.5	0.67	0.84

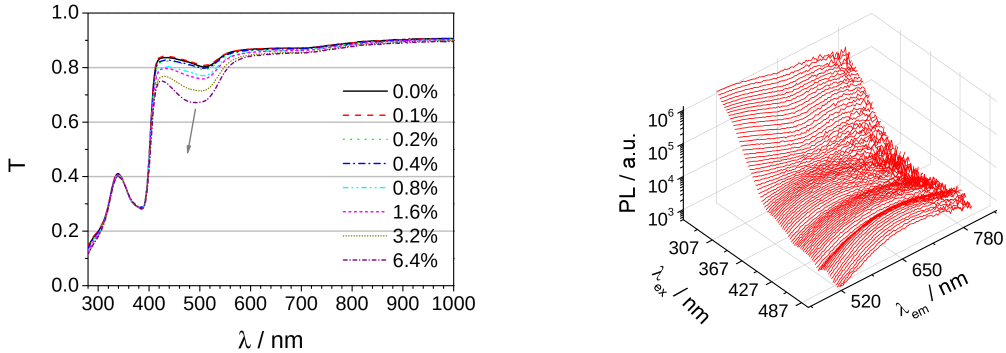

(a)

(b)

Figure 4.13: (a) Absorbance spectra of various DCM doped p-spiro-TTB thin films in dependence on the DCM concentration. The p-HTL has been doped with 3% NDP-9. (b) Fluorescence spectra in dependence on the excitation wavelength for 60 nm pure spiro-TTB.

layer is not affected until a DCM doping concentration of 1% is reached. Beyond this, the conductivity decreased from ≈ 5.5 to 2.5×10^{-5} Scm^{-1}, but still remained in a suitable range.

Figure 4.13 a shows the transmission spectra of the aforementioned layers. With rising DCM doping concentration, the optical density between 493 and 506 nm increases slightly, whereas it remains nearly constant in the red region of visible light, which is important for the ZnPc absorption.

Figure 4.13 b shows the emission intensity for DCM doped p-spiro-TTB as a function of the excitation wavelength. Clearly, at excitation wavelengths below 260 nm, the red emission is very intense. However, increasing the excitation wavelength resulted in only a very weak red emission which was close to the detection limit of the fluorospectrometer.

Table 4.5: Influence of DCM on the properties of the HTL Meo-TPD doped with 3% NDP-9 deposited on CE glass. The film thickness has been about 80 nm.

c_{DCM} / %	σ / $\times 10^{-4}$ Scm^{-1}	$T_{\lambda=504\rightarrow493nm}$	$T_{\lambda=605nm}$
0.0	2.4	0.76	0.84
0.4	2.6	0.74	0.84
1.7	1.5	0.72	0.84
6.6	1.0	0.64	0.83

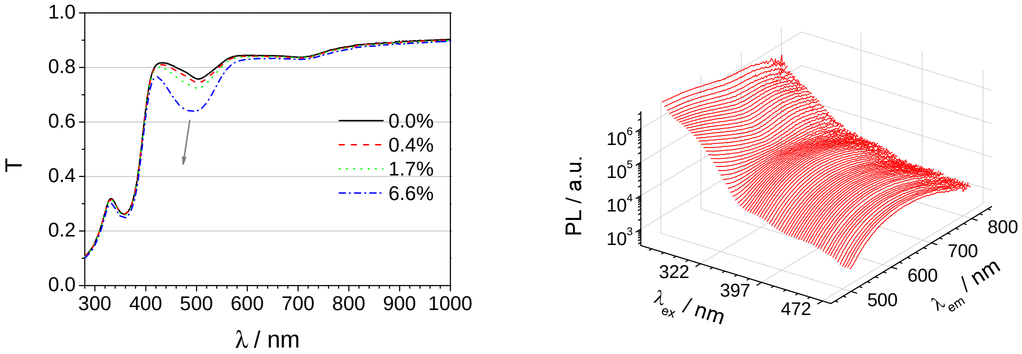

(a) (b)

Figure 4.14: (a) Absorbance spectra of various DCM doped p-MeO-TPD thin films for several DCM concentrations. The p-HTL has been doped with 3% NDP-9. (b) PL spectrum of a p-MeO-TPD layer with 6.6% DCM *versus* excitation wavelength.

With MeO-TPD as HTL Material

DCM has also been doped into p-MeO-TPD. The initial conductivity, of the order of 10^{-4} Scm^{-1} was high and decreased slightly with the addition of DCM (*cf.* table 4.5). Compared to the spiro-TTB samples, the conductivity values were lower by 50% with 6.6% DCM. The transmission was similar at 0.83. However, the investigation of the photoluminescent properties originating from DCM was difficult. As displayed in figure 4.14, only emission with low intensity could be detected at low, energy rich excitation wavelengths. Exciting the sample at wavelengths longer than 320 nm resulted in a clear drop of red emission. In order to be able to present the PL spectra, it has to be plotted on a logarithmic scale. Thus, the system p-MeO-TPD doped with DCM is not suitable for down-shifting applications.

With Alq_3 as LIL Material

As mentioned at the beginning of this chapter, DCM has widely been used as an emitter dopant material in tris(8-hydroxyquinolinato)aluminium (Alq_3) as the host system. Remarkably, DCM shows a distinct solid solvation dependency in Alq_3.[146] This effect is expressed in the form of a concentration dependent emis-

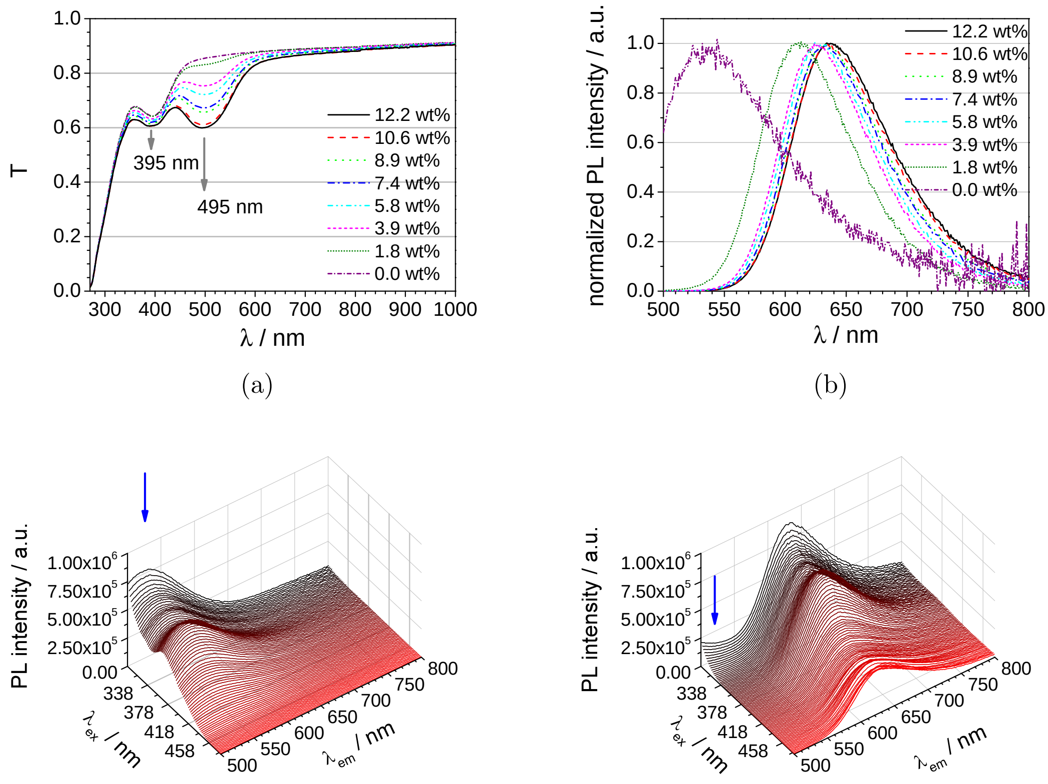

(a) (b)

(c) (d)

Figure 4.15: Transmission (a) and normalized PL spectra (b) of 80 nm Alq_3:DCM thin films in dependence on the DCM concentration as well as 3D photoluminescence spectra of thin films of pure Alq_3 (c) and Alq_3 doped with 10 wt% DCM (d).

sion color and intensity. The more emitter is doped into Alq_3, the more the emission is bathochromically shifted. This has been ascribed to the self-polarization of the DCM molecule, since it is more polar than the average organic semiconductor material or Alq_3, respectively. Because of this dependence of emission upon concentration, thin films with different DCM concentrations were fabricated and characterized.

Figure 4.15 a shows the transmission spectra of various Alq_3:DCM thin films with different compositional ratios. For better comparison the transmission properties are summarized in table 4.6. The more DCM is added, the stronger the transmission around 495 nm is reduced; this is due to the increasing absorption of DCM. Figure 4.15 shows the PL spectra of these layers excited at 495 nm for various DCM contents. As mentioned before, the emission shows a bathochromic shift due to the increasing polarity. After reaching a doping concentration of 10 wt%, the emission is not further red-shifted. Additionally, the emission originating from Alq_3 is immediately reduced after the addition of DCM. This is a clear sign of an efficient Förster resonance energy transfer.

Table 4.6: Optical properties of Alq_3:DCM thin films in dependence on the DCM concentration.

c_{DCM} / %	$T_{\lambda=507\rightarrow494nm}$	$T_{\lambda=605nm}$
0.0	0.83	0.88
1.8	0.83	0.88
3.9	0.75	0.87
5.8	0.72	0.86
7.4	0.67	0.85
8.9	0.66	0.85
10.6	0.61	0.83
12.2	0.60	0.83

Table 4.7: Overview of the emission maxima of pure and DCM-doped thin films.

Alq_3		Alq_3:DCM	
λ_{ex} / nm	λ_{em} / nm	λ_{ex} / nm	λ_{em} / nm
300	522	300	628
370	534	366	632
480	666	480	632

In order to investigate the excitation and emission characteristics of pure Alq_3 and DCM-doped Alq_3, emission spectra have been recorded for excitation wavelengths between 270 and 480 nm. These 3D spectra are presented in figure 4.15 c and d for pure and doped Alq_3, respectively. In both graphs the emission has been measured from 500 to 800 nm, where it can match with the ZnPc absorption. The spectrum from pure Alq_3 is characterized by green emission which exhibits its lowest energy excitation maximum at 370 nm. It can be seen that the wavelength of the emission maximum increases with rising excitation wavelength, (*cf.* table 4.7), whereas it stays almost unchanged in the doped Alq_3 thin film. The emission in this case is characterized by a red color with high intensity. The existence of FRET is attested to the unchanged location of the lowest energy excitation maximum at around 368 nm, which means that the energy absorbed by Alq_3 is directly transferred to the acceptor molecule DCM. Beyond the excitation of Alq_3, DCM still emits by itself with a slightly lower intensity. Thus, red emission can be realized by excitation between 270 and 550 nm. Furthermore, it should be noted that there is a difference in the shape of the absorption and excitation spectra of Alq_3:DCM thin films. It is a common mistake to isolate the excitation maximum from the absorption profile. The magnitude of the mismatch between these two spectra depends on the extent of radiationless losses.

Comparing the quantum yield of DCM in p-spiro-TTB, p-MeO-TPD and Alq_3, the highest emission intensity is achieved with Alq_3 as host. Hence, DCM is not suitable for down-shifting emission within a hole-transporting material. On the other side, Alq_3 has often been described as an electron transporting material realizing an ohmic contact in combination with a thin LiF layer. However, since the pin-concept is supposed to be used, the system Alq_3:DCM will be applied as a down-shifting light-incoupling layer. Light-incoupling layers are used to influence the optical field distribution and its amplitude, and to reduce the external reflection of the semitransparent top contact. Whereas a strong correlation between the LIL and the J_{SC} exists, Meiss et al. described minor influences on the V_{OC}, FF and saturation values.[147]

Because of the convenient possibility of tuning the emission color by varying the doping concentration, this LIL can be adjusted for several donor systems absorbing between 500 and 700 nm. Furthermore, with the combination of DCM and Alq_3 another advantage arises. Pure Alq_3 has a strong absorption coefficient ($\alpha > 10^5$ cm^{-1} from 250 to 300 nm,[148] $\alpha > 10^4$ cm^{-1} from 300 to 420 nm) in the UV to blue light while staying below 10^{-1} cm^{-1} for longer wavelengths. This means that more than a half of the near-UV is absorbed by a film of only 40 nm thickness. Additionally pure Alq_3 shows a green emission, whose intensity is, however, still two magnitudes lower than the doped film, thus rather non-emitting. Due to the strong absorption between 300 and 440 nm, the energy rich UV/vis radiance, which has often attribted for the degradation of several organic semiconductors in organic solar cells, is filtered out before the organic solar cells.[149] Adding DCM into Alq_3 broadens the absorption spectrum of energy rich radiance to 550 nm. Additionally, the energy is not lost for the solar cell as it would be the case for pure Alq_3. The absorbed light with a wavelength as short as 400 nm will be transferred from Alq_3 to DCM *via* FRET, resulting in radiative decay as red emission. This can easily be absorbed by the C_{60}:ZnPc containing absorption layer, as shown by the spectral overlap of Alq_3:DCM emission with C_{60}:ZnPc absorption. The normalized spectra (*cf.* annex figure A.1) b have an overlap of 99.5%.

4.2.2 Design of the Top-Absorbing Solar Cells

Optical Simulation

In order to apply a fluorescent LIL in organic solar cells, a stack architecture for top-absorbing solar cells is utilized. The principle architecture has been adopted from references[147] but has been modified. Several optical simulations have been carried out in order to locate the electric field amplitude maximum in the absorption layer. The optical simulation started with a fixed stack architecture, and the variation was carried out for each layer. The results are presented in figure 4.16 and 4.17 for pure Alq_3 and doped Alq_3 as LIL material.

Clearly, the absorptivity of the C_{60}:ZnPc shows a dependency upon all layers

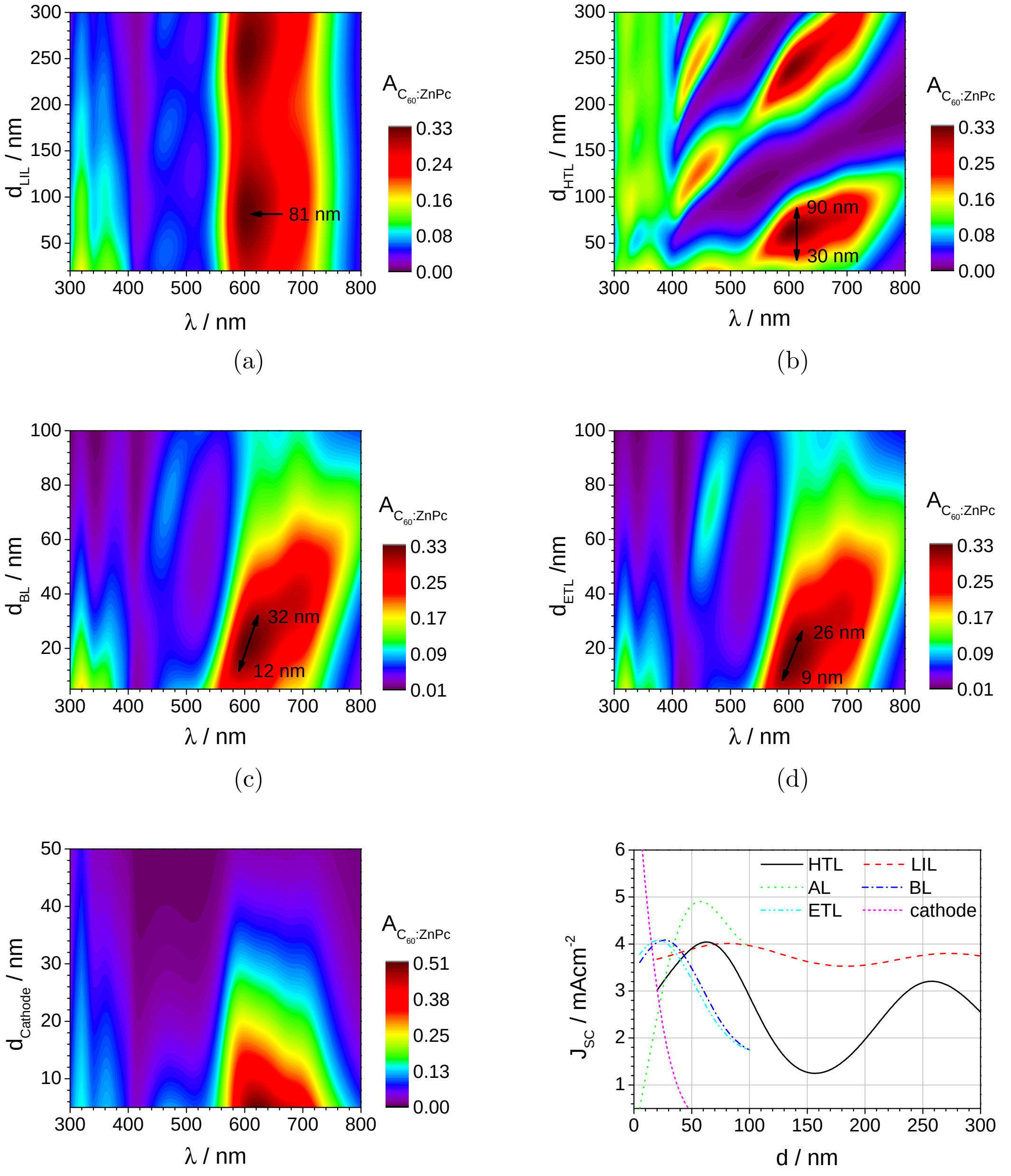

(a) (b) (c) (d) (e) (f)

Figure 4.16: Optical simulation of the absorptivity of the absorption layer C_{60}:ZnPc for different layer thicknesses of the DCM free LIL (a), p-HTL (b), BL (c), ETL (d) and the semitransparent cathode (e). If not varied for the plot, the thicknesses were 80 nm Ag, 60 nm p-HTL, 35 nm AL, 20 nm BL, 15 nm ETL, 15 nm Ag, 80 nm LIL doped with DCM. The subfigure (f) shows the predicted J_{SC} generated by the AL assuming the AM 1.5 spectrum for the variation of each layer thickness.

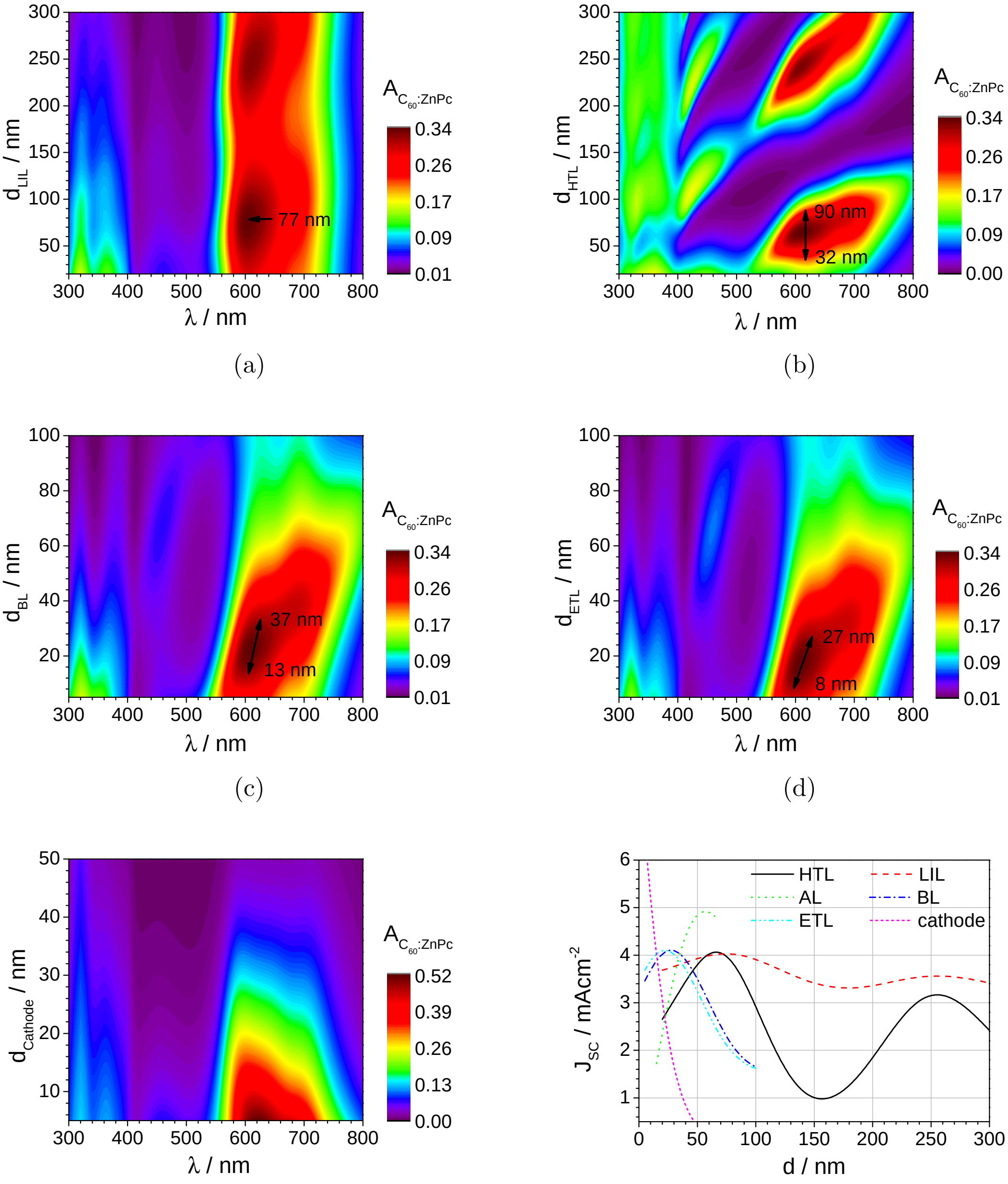

(a) (b) (c) (d) (e) (f)

Figure 4.17: Optical simulation of the absorptivity of the absorption layer C_{60}:ZnPc for various values of the layer thickness of the LIL doped with DCM (a), p-HTL (b), BL (c), ETL (d) and the semitransparent cathode (e). If not varied for the plot, the thicknesses were 80 nm Ag, 60 nm p-HTL, 35 nm AL, 20 nm BL, 15 nm ETL, 15 nm Ag, 80 nm LIL doped with DCM. The subfigure (f) shows the predicted J_{SC} generated by the AL assuming the AM 1.5 spectrum for the variation in thickness of each layer.

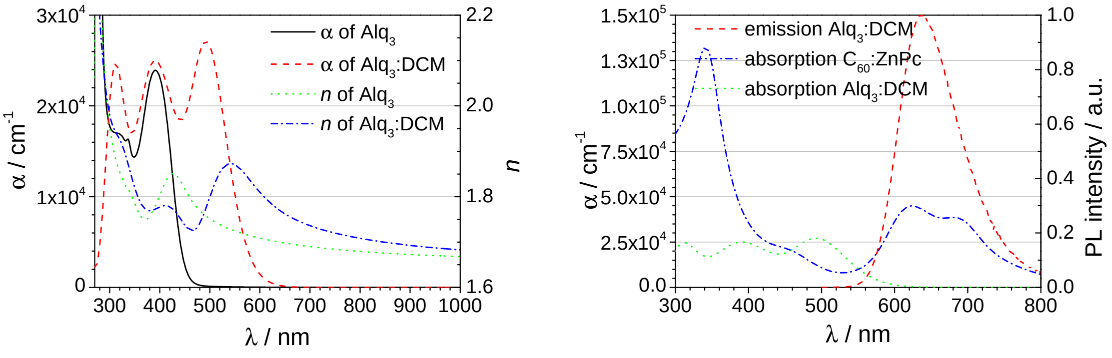

(a) (b)

Figure 4.18: (a) Optical constants α and n for pure Alq$_3$ and doped Alq$_3$ with 10wt% DCM. (b) Spectral properties of the emissive and absorptive layers of the OSC.

in the spectral region from 550 to 750 nm, however with different sensitivities. Whereas the thickness of the BL, ETL and HTL have an enormous impact on the position of the optical cavity, the influence of the LIL is comparatively low. For clarification, the predicted J_{SC} under the assumption of AM 1.5 illumination is illustrated in figure 4.16 and 4.17 f.

Due to the parasitic absorption of the BL and ETL, their thicknesses were limited for simulation revealing only the first field amplitude maximum. However, because of processing reasons, the second thickness maxima were not considered for the HTL and LIL. Furthermore, it can be seen that a thin semitransparent cathode is essential for high J_{SC} values. Hence, a thickness for an optimal compromise between high transparency and good conductivity should be chosen.

The simulations for pure and doped Alq$_3$ as light-incoupling layers show that the dopant (concentration) has only a minor influence on the optical field distribution even though the optical constants are rather different, as shown in figure 4.18. The absorption bands of Alq$_3$ can easily be assigned in spectra from the mixed Alq$_3$:DCM thin film, which additionally feature an absorption band occuring at 490 nm, due to DCM absorption. With respect to the low DCM concentration of 10 wt%, the value of the absorption coefficient at that wavelength is remarkable (α(490 nm) $= 2.7 \times 10^4$ cm^{-1}), suggesting a strong transition dipole moment and a medium with a high polarity.

According to the optical simulation, more photons will be absorbed by the doped LIL in the region from 300 to 530 nm (A = 0.33 - 0.66) than all photons absorbed by the AL from 550 to 750 nm. The absorption profiles of the LILs with and without DCM are depicted in figure 4.19. Furthermore, the maximum absorption of the LIL can also be tuned by varying the HTL thickness.

Because of the good agreement between the pre-assumed stack architecture and the simulation results, only the thickness of the HTL will experimentally be varied

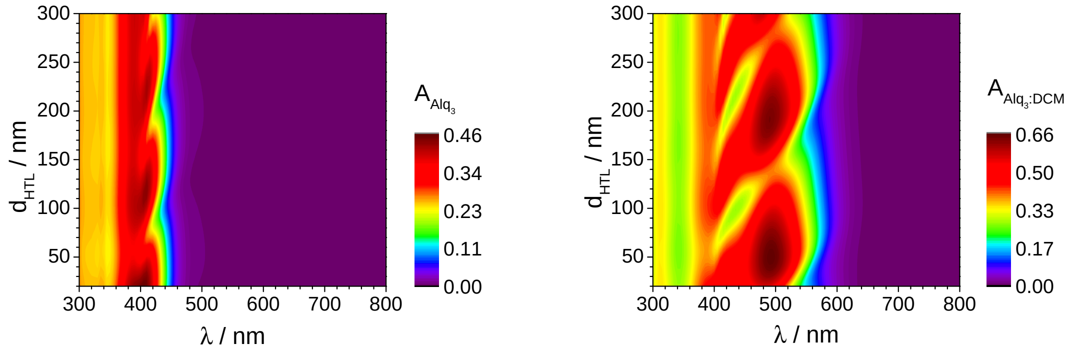

(a)

(b)

Figure 4.19: Optical simulation of the absorption behavior of (a) pure Alq_3 and (b) Alq_3:DCM thin films doped with 10 wt% DCM in dependence on the HTL layer thickness.

for optimization purposes. Hence, an organic solar cell consisting of the following layer sequence will be investigated: glass / opaque anode of aluminium and silver / x nm p-spiro-TTB, 35 nm AL / 20 nm BL / 15 nm ETL / 15 nm cathode of aluminium and silver / 80 nm LIL. Since the emissive LIL and the absorbing AL are separated by around 50 nm, which is too large for FRET, the magnitude of the incoupling will be investigated by a variation of the DCM concentration in the LIL to directly study the effect of this of this approach.

Optimization of the Electrodes

The fabrication of top-absorbing solar cells necessitates the deposition of an opaque anode and a semitransparent cathode. In order to enhance the J_{SC} value due to the back reflection of light at the opaque anode, a material such as silver is generally used for high reflectivity. The drawback of thin silver films is their general tendency to form films with very high roughness, which is disadvantageous for the parallel resistance of organic devices. Therefore, a thick layer of aluminium was deposited prior to the fabrication of a thin silver layer to give an opaque anode with a high reflectance and low roughness. For this purpose different fabrication parameters such as layer thicknesses and deposition rates were varied to optimize the anode.

Figure 4.20 shows the transmission and reflectance curves of several combinations of Al and Ag. The transmission decreases with both the thickness of Al and Ag. However, the same thickness increase realized by Ag does not give such good results as the same total thickness of Al. This is attributed to the wetting behavior of Ag, which forms islands before becoming a closed film.

The reflection spectra show that Ag is necessary to increase the reflectivity, in particular at longer wavelengths. All samples with 40 nm thick Ag show the highest transmission at 700 nm, however, the samples with 40 or 50 nm Al and

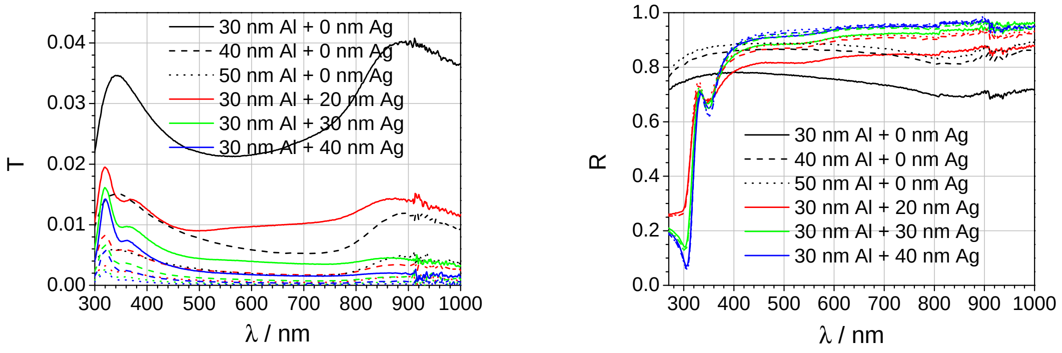

(a) (b)

Figure 4.20: (a) Transmission and (b) reflection spectra of different metal thin films. The thickness of Al is varied from 30 nm (line), 40 nm (dashed) to 50 nm (dotted) and of Ag from 0 nm (black), 20 nm (red), 30 nm (green) to 40 nm (blue). The aluminium or silver rate have been set to 0.3 or 0.7 Å/s, respectively.

Table 4.8: Summary of the anode properties in dependence on the deposition parameters of silver. The anode consists of 50 nm Al (r = 0.3 Å/s) and 30 nm Ag.

	r_{Ag} = 0.3 Å/s	r_{Ag} = 0.5 Å/s	r_{Ag} = 0.7 Å/s	r_{Ag} = 1.0 Å/s
RMS	2.6	3.2	2.8	3.1
S_a	2.1	2.5	2.2	2.4
S_{ku}	6.2	3.1	3.3	3.7
S_p	31	18	16	28
S_v	25	13	13	12
S_z	56	31	29	40

30 nm Ag are similarly reflective. Hence, since 10 nm more Ag means higher roughness, the deposition parameters were varied for the combination 50 nm Al / 30 nm Ag because here the transmission will be below 0.2% and the reflectivity above 90% from 400 to 900 nm. In order to optimize the morphology of the Ag coating, the Ag evaporation rate was varied. The resulting surface properties of AFM images (1 × 1 µm^2) are summarized in table 4.8. With respect to the root mean square (RMS) roughness and the arithmetic mean value (S_a) all samples are similar. However, the kurtosis (S_{ku}) which is a measure of sharpness of the surface as well as the peak (S_p) and valley (S_v) values are different. The sample, for which the silver coating was applied at a deposition rate of 0.7 Å/s has the best distribution of spikes and has the lowest sum of peak and valley value (S_z). Thus, all anodes were fabricated with 50 nm Al (r = 0.3 Å/s) and 30 nm Ag (r = 0.7 Å/s).

Table 4.9: Key values of top-absorbing organic solar cells[a] in dependence on their HTL thickness.

d_{HTL} / nm	V_{OC} / mV	J_{SC} / mAcm^{-1}	FF / %	η / %	S
45	503	4.23	47.9	1.03	1.18
55	508	5.20	49.3	1.31	1.21
60	506	5.40	48.7	1.35	1.15
65	536	5.63	44.8	1.36	1.15
70	516	5.61	46.5	1.36	1.17
80	538	5.58	47.1	1.42	1.17
90	519	4.84	43.2	1.10	1.21

[a] Glass / 50 nm Al and 30 nm Ag / 1 nm NDP-9 / x nm p-spiro-TTB / 35 nm C_{60}:ZnPc (6:4) / 20 nm C_{60} / 15 nm n-C_{60} / 3 nm Al and 12 nm Ag / 80 nm Alq_3:DCM (10 wt%).

4.2.3 Variation of the Hole Transporter Layer Thickness

As summarized in figure 4.16 and 4.17 f, the dependency of high photocurrents upon thickness is most pronouced for the HTL. Thus, samples with seven different HTL thicknesses ranging from 45 to 90 nm were fabricated in order to investigate the best thickness to enable high J_{SC} values. Table 4.9 gives an overview of the resulting key values of the devices. As expected, FF and V_{OC} show no dependency on the HTL thickness. This is attributed to the high conductivity of the p-HTL preventing charge carrier losses due to high resistance. However, the scattering of the values is higher than expected from the evaluated measurement uncertainty.

Nonetheless, a clear relation between J_{SC} and the HTL thickness can be drawn. Figure 4.21 presents the measured J-V curves in the dark and under illumination and shows the evaluated d_{HTL}-J_{SC} relation in comparison with the predicted J_{SC} values from the optical simulation.

Clearly, J_{SC} has a maximum for thicknesses in the range between 65 and 80 nm and the results are consistent with the predicted behavior. According to the simulations, a maximum short circuit current density is reached for an HTL thickness of 65 nm. The experiments show that slightly higher thicknesses also give very good photocurrents. This reproduction shows that the optical model used as well as the applied parameter sets of the optical constants are in good agreement with reality.

4.2.4 Impact of the DCM Concentration within the LIL

In order to validate the justification of the DCM insertion into the LIL, the DCM concentration was increased from 0 to 10 wt%. The J-V curves recorded under illumination and in the dark of the resulting OSC (*cf.* figure 4.22 a) show samples with high fill factors and V_{OC} values as expected for C_{60}:ZnPc BHJ cells. The

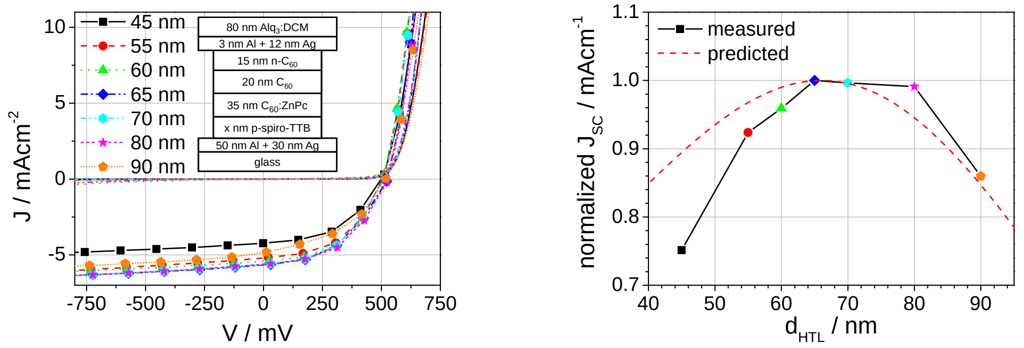

(a) (b)

Figure 4.21: (a) *J*-*V* characteristics of top absorbing OSC under illumination (line + symbol) and in the dark (line) in dependence on the HTL layer thickness and (b) the J_{SC} value plottet against the HTL layer thickness.

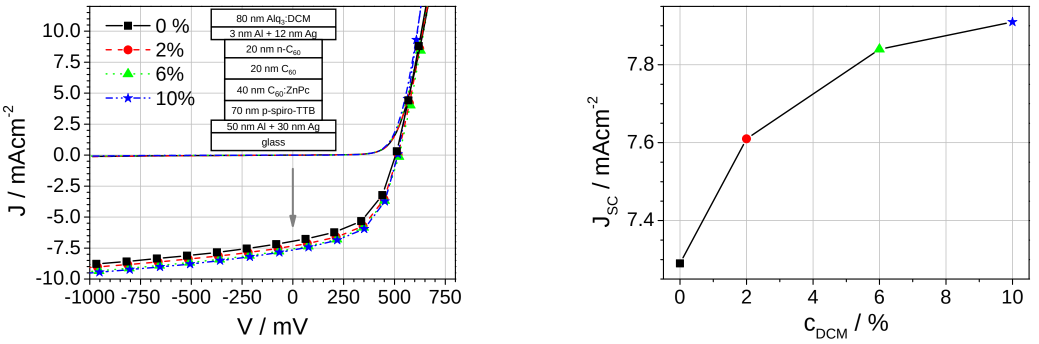

(a) (b)

Figure 4.22: (a) *J*-*V* characteristics of top absorbing OSC under illumination (line + symbol) and in the dark (line) as well as (b) the J_{SC} value plottet versus the DCM concentration.

key values of the resulting devices are summarized in table 4.10. Since the LIL is not involved electrically in the photovoltaic processes, parameters such as the *FF*, V_{OC} and *S* are not affected by the dopant concentration. Merely the short-circuit current density J_{SC} increases with rising DCM content in the LIL. Starting with the top-absorbing sample with pure Alq_3 as LIL material, short circuit current densities of 7.20 mAcm^{-2} are obtained yielding an efficiency of 1.90%, which is slightly higher than reported by Meiss and co-workers (1.84%).[147]

After adding DCM to Alq_3 by co-deposition, the emission intensity increased and changed from greenish to orange-reddish; the BHJ absorption layer can better absorb the red light re-emitted by the LIL. This is confirmed by the spectral response measurements, which will be discussed later in detail.

Interestingly, the enhancement of the photosensitivity saturates quickly, as displayed in figure 4.22 b. The highest jump of 0.41 mAcm^{-2} is observed at 2% DCM addition. Addition of further DCM to a dopant concentration of 6% enhances the

Table 4.10: Key values of top-absorbing organic solar cells[a] in dependence on the DCM concentration in the light incoupling layer.

C_{DCM} / %	V_{OC} / mV	J_{SC} / mAcm^{-1}	FF / %	η / %	S
0	514	7.20	51.3	1.90	1.21
2	524	7.61	52.7	2.11	1.19
6	537	7.80	51.7	2.16	1.19
10	525	7.92	53.3	2.21	1.19

[a] Glass / 50 nm Al and 30 nm Ag / 1 nm NDP-9 / 70 nm p-spiro-TTB / 40 nm C_{60}:ZnPc (6:4) / 20 nm C_{60} / 20 nm n-C_{60} / 3 nm Al and 12 nm Ag / 80 nm Alq_3:DCM (x wt%).

J_{SC} by 0.21 mAcm^{-2}, and after another 4% DCM (total content of 10%) only by 0.12 mAcm^{-2}.

In order to analyze these results further, reflectance and emission spectra have been recorded for these samples. By means of the reflectance spectra, the absorption of the whole device can be evaluated. As displayed in figure 4.23 a, the absorption peaks originating from Alq_3 (405 nm), DCM (505 nm) and ZnPc (625 - 690 nm) can be assigned. Whereas the absorption stays nearly unchanged for Alq_3 and ZnPc related bands, the DCM band increases noticeably with rising dopant concentration, which results, for the sample with 10% DCM in the LIL, to an absorption value comparable to that of the ZnPc band. These measurements show that the absorption profile can be considerably altered by the choice of the LIL composition.

However, there is often a huge difference between the absorption capability and the generation of free charge carriers. Unlike the absorption spectra, the SR spectra show the dominant Q/Q$^+$ bands of ZnPc and the superposition of C_{60} and Alq_3 absorption. For clarification, the spectra are normalized at the ZnPc related bands because the layers beyond the LIL have been kept equal. At 480 nm an absorption shoulder rises and increases with the DCM content. For the interpretation of the SR spectra, a discussion of the emission properties of the light incoupling layers is required.

The PL spectra of all solar cell samples are presented in figure 4.24. As mentioned before, the emission color and intensity change with the DCM content. Figure 4.24 shows the emission spectra of all four samples at various excitation wavelengths. These wavelengths have been selected to correspond to shoulders or maxima in the SR spectra. Depending on the excitation wavelength, transitions occuring in either Alq_3 (330, 365 and 405 nm) or DCM (480 nm) are excited. The device with pure Alq_3 has a yellowish emission with rising intensity the honger the excitation wavelength. Any emission in the red region is missing. After inserting 2% DCM into Alq_3, all the excitation energy in transferred to the DCM molecule via FRET, resulting in red emission. Furthermore, the DCM molecule can also be

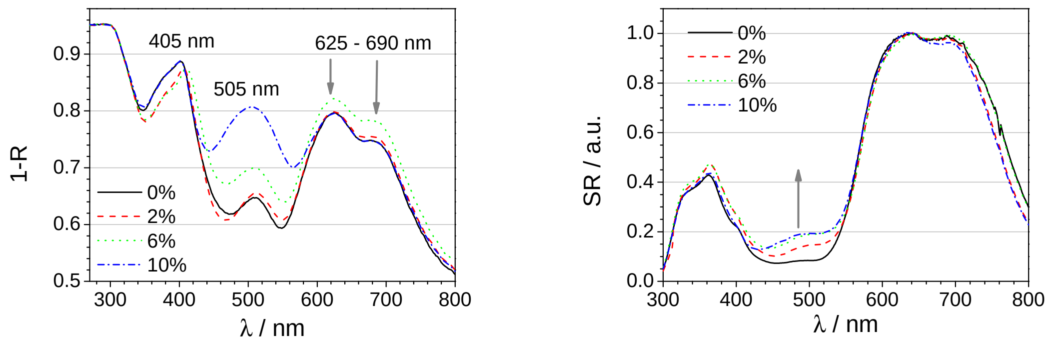

(a) (b)

Figure 4.23: (a) Absorption spectra of the devices as well as (b) their corresponding spectral response measurements in dependence on the DCM concentration in the light incoupling layer.

directly excited by illuminating it with 480 nm light. Further addition of DCM to 6% has increases the emission intensity and shifts it slightly bathochromatically. Beyond that, the direct excitation of DCM becomes more effective. This observation continues to be true up to a content to 10%. The highest intensity of red light is achieved after direct excitation of DCM, for which the energy transfer from Alq_3 is less efficient compared to lower DCM concentrations.

A comparison between these results and the SR spectra (4.22 b) explains the steep increase of the short circuit current density after the insertion of 2% DCM into the LIL and the subsequent saturation. The emission from pure Alq_3 is green and can hardly be absorbed by ZnPc. Due to the effective FRET from Alq_3 to DCM, photon energy absorbed by DCM and most notably by Alq_3 can be utilized for exciton generation in the C_{60}:ZnPc blend because of the matching spectral overlap between the red DCM related emission and the absorption profile of ZnPc. Up to 6% of DCM, the effectivity of this FRET and the emission intensity increase with the doping concentration. This can be seen in the SR spectra with a higher sensitivity at 360 nm (Alq_3 excitation) and 480 nm (DCM excitation). At 10% DCM content, the sensitivity at 360 nm drops back to a value prior to DCM doping and reveals only a higher response at 480 nm, which means that mainly direct excitation of DCM occurs. Hence, higher DCM concentrations in the LIL will not increase the J_{SC} value further.

The solar energy irradiated from 300 to 420 nm yields only 71 $\mathrm{mWm^{-2}nm^{-1}}$ and increases up to 247 $\mathrm{mWm^{-2}nm^{-1}}$ within the spectral range of 300 to 540 nm, which is around the half of the spectral range from 300 to 800 nm with 589 $\mathrm{mWm^{-2}nm^{-1}}$. Thus, enhancing the absorptivity in the blue range of light can only account for 12% of the achievable energy from 300 to 800 nm. Addressing also the part of the spectrum till 540 nm, already 42% of the irradiated energy is available for charge generation. Keeping this in mind, the J_{SC} improvement resulting from the

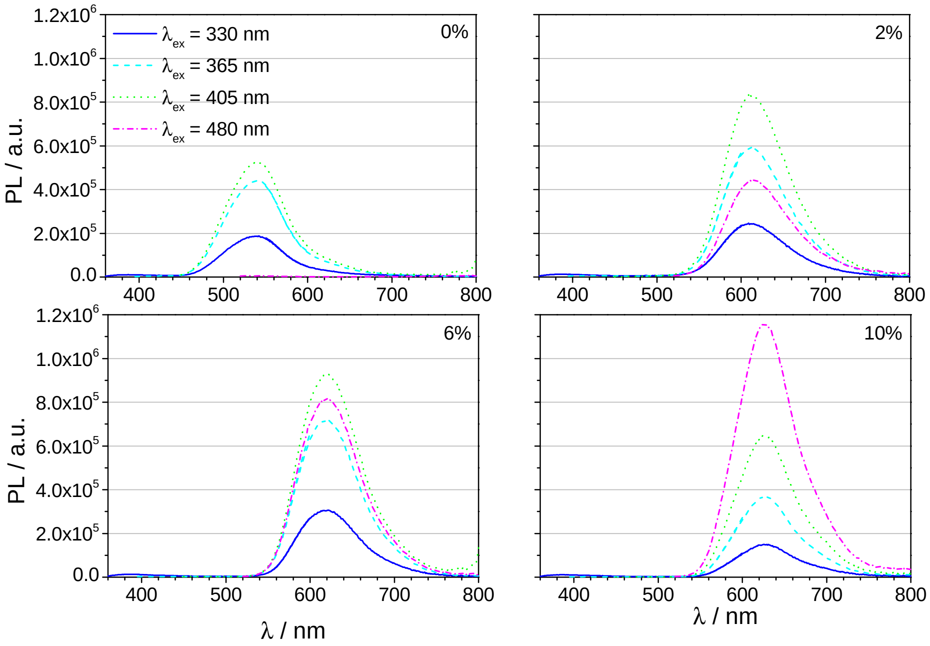

Figure 4.24: PL spectra of top-absorbing OSC with different LILs in variation of their DCM doping concentration. These spectra are depicted for the excitation wavelengths at 330 nm (line), 365 nm (dashed), 405 nm (dotted) and 480 nm (dash-dotted).

addition of 2% is with 0.4 $\mathrm{mAcm^{-2}}$ (5%) remarkable and maximizes at 10 wt% by 0.72 $\mathrm{mAcm^{-2}}$ (10%).

4.2.5 Summary and Outlook

Different approaches have been considered in order to realize a energy-down-shifting layer integrated in the stack architecture of organic solar cells. Besides the insertion in a light incoupling layer, several material combinations for hole transport layers have been tested. However, sufficiently emissive properties have only be achieved for the system $\mathrm{Alq_3}$:DCM, which was applied on top of a semi-transparent top-cathode as a LIL. The optical properties of the designated LIL were investigated. The stack architecture used here has been adopted from literature but then modified. In order to achieve best performances optical simulations were carried out and the layer thicknesses have been adjusted. Using the resulting optical layer sequence gave devices with efficiencies comparable to these reported in the literature. It has been shown that the concept of introducing a down-shifter in a OSC can be used to enhance the absolute J_{SC} by 10% by blocking the harmful UV radiation which is believed to be responsible for degradation processes in organic photovoltaics. With this approach, this energy is not lost and can be used for charge generation. DCM is not the only great off-the-shelf fluorescent emitter that can be used for inner-down-shifting applications. This means that the separated UV-irradiation can be transformed for any D:A system. Additionally, the results of these experiments show that any emitter can be used as sensitizer, if its emission matches well with the spectral response profile of the OSC. Even the utilization of this concept for x-ray detection can be considered, since several evaporable organic semisconductors are known to act as scintillators, *e.g.* 2-phenyl-5-(4-biphenyl)-1,3,4-oxadiazole. Moreover, other aspects have to be considered. Since plasmonic processes allways occur close to metal films, any emission within 40 nm of this metal film is quenched, so lost for charge generation. Consequently, any non-emitting material with weaker parasitic absorption should be used as spacer. Keeping this in mind, there is still no tool for optical simulations available which enables the treatment of emissive layers within an organic solar cell, which also absorb and transform the sun light. Finally, applying another layer on top of the LIL might also help to inhibit the loss of emissive radiation from the LIL into air.

Chapter 5

Organic Solar Cells with Ternary Absorption Layers

As outlined in the previous chapters, organic solar cells with BHJ binary blended films have attracted tremendous attention since they are currently leading the efficiency record for OPV with 12.0%.[85] The concept of BHJs represents the nanoscale, self-assembled heterojunctions via spontaneous phase separation of the donor and acceptor material throughout the bulk. Efficient exciton dissociation and the charge transport through a bicontinuous interpenetrating network are the characteristics of BHJ blended films.

In binary blended BHJ solar cells, the J_{SC} is proportional to the product of the absorption strength and spectral breadth of the active layer, which is generally limited by the bandgap (E_g) of the donor material. In principle, a smaller E_g gives a broader wavelength range of light absorption and consequently a higher J_{SC}. However, most organic compounds show characteristic absorption bands in the UV/vis range and hence, a limited match with the solar spectrum. An approach to circumvent this and to gain higher efficiencies instead, is the principle of tandem solar cells, in which two (or more) subcells absorbing light in different regions of the solar spectrum are connected either in series or parallel. This has become an attractive alternative to simple BHJ solar cells. Predictions for the ultimate achievable efficiency of tandem solar cells were between 14 to 15%.[150] In the case of serially connected subcells, the V_{OC} of the tandem cell can achieve the sum of the subcell V_{OC}, whereas J_{SC} approaches only the lowest value of subcells. For parallel connected subcells, the correlations of V_{OC} and J_{SC} are reversed. A further drawback of the tandem solar cell design is the increased complexity of the architecture and fabrication. In order to address these challenges, the concept of small-molecule based BHJ solar cells with ternary blended absorption layers will be investigated in this chapter.

Due to the easy fabrication of a tricomponent system, the use of polymer

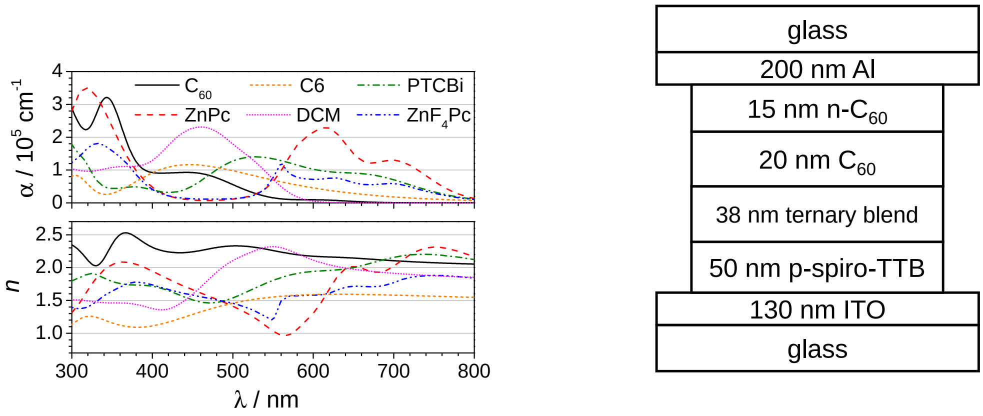

(a) (b)

Figure 5.1: (a) Optical properties of the pure materials which will be used for the tricomponent absorption layer in OSCs. (b) General stack architecture of the organic solar cells fabricated for this chapter.

based ternary blends for organic BHJ solar cells has increasingly been explored since 2003. The third material has been used to broaden the spectral sensitivity of the solar cell by addition of a sensitizer dye such as porphyrine or copper phthalocyanine[131,151–155] or another polymer,[156–158] to improve the charge carrier transportation properties within the absorption layer by introducing a material with ambipolar properties (B),[159,160] or to control the blend morphology by the additive.[161–164] Hence, various combinations such as D:D:A, D:A:A, D:B:A or all-polymer[156,157,162] and polymer:small molecules[131,152–155,161,163,165–167] have been investigated. For many examples, the introduction of a third component in the BHJ led to an efficiency decrease,[152,166] however, lately, many examples have been reported where the ternary system has shown better performance than their binary subsystems.[131,158,160,164,165,167] The improvement has often been related to a simplified morphology control which is important to limit the grain size of the polymer aggregates. However, there is a significant difference between polymer-based and small molecule-based solar cells. During fabrication, polymers show a strong tendency for phase separation and aggregate formation, which can reach the µm regime in extreme cases when the aggregates are too large compared to the small exciton diffusion length. When introducing a third component to the blended system, the crystallization is disturbed and can even be suppressed. While this represents an advantage for polymer-based solar cells, it can be a serious problem for small molecule based ones since the size of the aggregates is much smaller and particular care has to be taken to support the crystallization.

The introduction of a third material in the absorption layer thus allows the possibility of analyzing its impact to the photo- and electrophysical properties of organic solar cells and can help to obtain a deeper understanding of such solar cells. For this purpose, various combinations of a tricomponent system have been chosen to pay attention to different issues, which can not always be realized in one single compound due to the different optical and electric properties of each material:

- The *offset of the molecular orbitals*: The positions of the energy levels will be varied for the donor molecules in order to realize a cascade structure for the holes or electrons. Moreover, traps for charge carriers of different depth will be generated. This will be discussed within the series C_{60}:ZnPc:C6 (A:D:D, ZnPc and C6 with ΔHOMO = 0.3 eV) or C_{60}:PTCBi:ZnPc (A:A:D, C_{60} and PTCBi, ΔLUMO = 0.1 eV) and, to exclude any influence due to different geometries, the series C_{60}:ZnF_4Pc:ZnPc (A:D:D, ZnPc and ZnF_4Pc with ΔHOMO = 0.2-0.3 eV) will be investigated.
- The *spectral coverage* with respect to the solar spectrum will be broadened. This will be highlighed for C_{60}:ZnPc:C6 and C_{60}:PTCBi:ZnPc tricomponent systems.
- Additives with different chemical structures will impact the *morphology* differently. This will be considered for all test series.
- The continuous variation of the blend composition has a significant influence on the *key values* of the solar cells, in particular on V_{OC}. This will be discussed for all the test series and in more detail for the ternary blend C_{60}:ZnF_4Pc:ZnPc.

Because several issues are simultaneously addressed by one ternary system, each blended absorption layer combination will be analyzed separately and afterwards a summarized discussion will follow. In order to ensure a high comparability, the content ratio of either the acceptor or donor material will be kept constant in all material systems. The ratio variation is referred to volume fractions.

5.1 C_{60}:ZnPc:C6 Ternary Blends

5.1.1 Optical Characterization

The optical constants and the investigations regarding the photoluminescent properties of the C_{60}:ZnPc:C6 ternary thin films are depicted in figure 5.2. With rising C6 content, both the absorption coefficient and the refractive index increase in the range from 400 to 500 nm due to C6 related transitions. In contrast, the absorption strength decreases between 600 and 700 nm. Additionally, the ratio of the Q^+ band (610 nm) to the Q band (690 nm) changes, suggesting that the amount

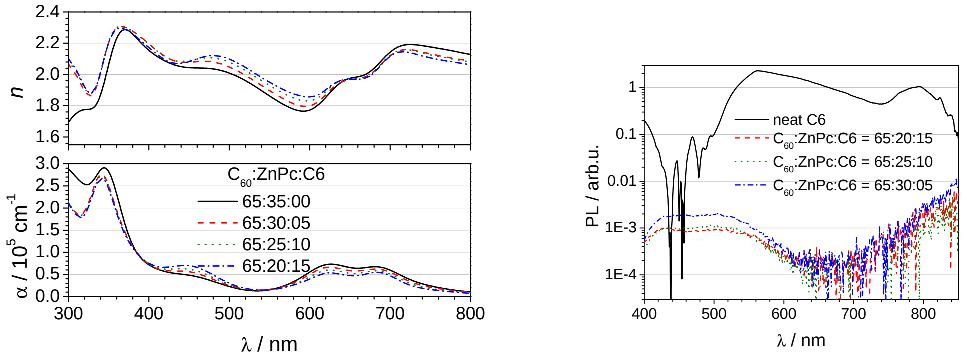

(a) (b)

Figure 5.2: Absorption coefficient α (a, bottom) and refractive indices $\mathbf{n}$ (a, top) of C_{60}:ZnPc:C6 blended layers as well as their PL spectrum after excitation at 295 nm (b).

Table 5.1: Solar cell key values of diodes with ternary absorber layers in dependence of its composition and corresponding determined relative permittivies of the absorption layers.

C_{60}:ZnPc:C6	V_{OC} / mV	J_{SC} / mAcm^{-2}	FF / %	η / %	S	ϵ_r
65:35:00	542	8.72	58.7	2.75	1.13	4.87
65:30:05	538	7.45	55.7	2.22	1.14	5.45
65:25:10	522	7.27	54.4	2.06	1.12	5.61
65:20:15	514	6.65	42.9	1.47	1.17	5.72

of higher aggregated ZnPc lowers at the expense of the smaller ZnPc aggregates with increasing C6 concentration, as a result of the ZnPc dilution. Remarkably, the refractive index within the aforementioned spectral regions is affected from 450 to 600 nm and at the end of the spectrum. With respect to the photoluminescent characteristics, no emission originating from C6 could be detected, although C6 is renowned for its high fluorescence quantum efficiency. This makes this layer composition suitable for introduction in PV cells because radiant desactivation paths of the excited states seem not to be present.

5.1.2 Characterization of the Solar Cells

The previously listed tricomponent mixtures of the absorber materials were utilized for the fabrication of solar cells in order to investigate the influence of the composition. The impact on the devices is summarized in table 5.1. Figure 5.3 shows the corresponding J-V characteristics under illumination and in the dark.

Clearly, with the introduction of a third absorber the efficiency drops from 2.75% to 1.47%. This decrease is mainly related to the reduction of the FF and J_{SC}. The lowering of FF can neither be explained by means of R_S nor by R_P. Although C6 has demonstrated a lower charge carrier conductivity in previous

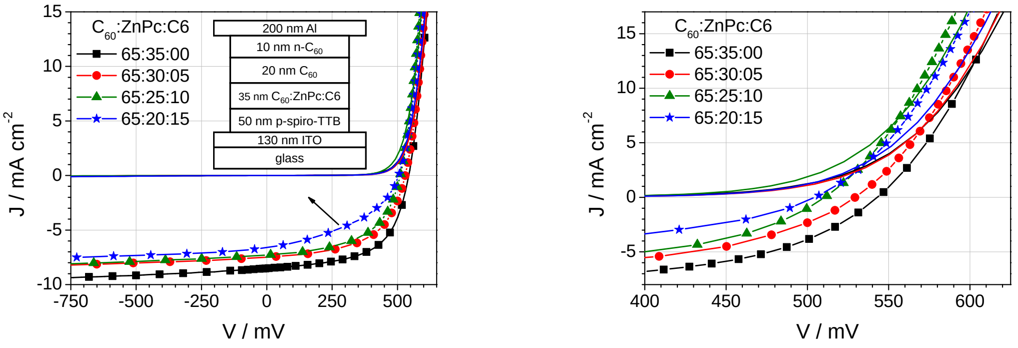

(a) (b)

Figure 5.3: *J*-*V* characteristics under illumination (line + symbol) and in the dark (line) of ternary solar cells in dependence on the AL constitution. The cells have been fabricated at room temperature.

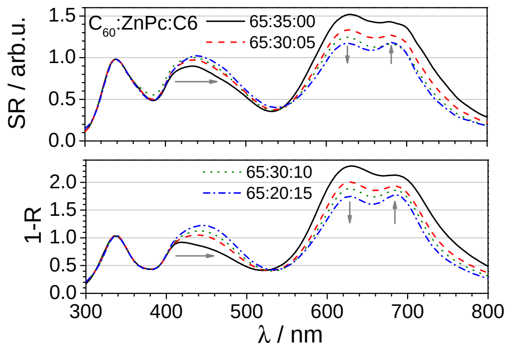

Figure 5.4: SR spectra (top) and their corresponding absorption spectra (bottom) in dependence on the AL composition.

investigations,[144] no increased R_S can be assigned in the *J*-*V* curves with rising C6 content. Furthermore, no change in S is indicated, which means that R_P is sufficiently high. The drop in FF is due to charge carrier traps generated by C6 which will be discussed later on.

Regarding the J_{SC} value, it declines for the binary AL from 8.72 mAcm^{-2} to 6.65 mAcm^{-2} for the ternary AL. At first glance, this drop seems tremendous, but taking into account that the match with the solar spectrum decreases as well, the drop is less distinct than it appears. Taking the absorptivity of the different ALs into account, the ternary cells show a J_{SC} which is only 10% lower than the maximum possible related to the binary reference sample.

With respect to the spectral sensitivity, the current which originates from ZnPc related bands is lower than expected according to the absorption within the AL. For better comparison, see figure 5.4 a, where the spectra are normalized to the first absorption peak due to C_{60}. According to the simulation, the ZnPc bands should be twice as high as the reference peak (at 340 nm). However, in the SR measurements, the ZnPc band is only 150% of the reference peak. Nevertheless,

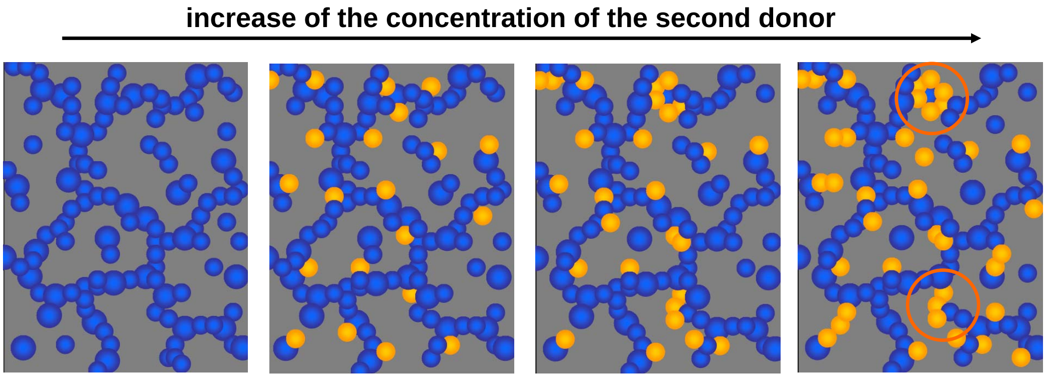

Figure 5.5: Possible detail of the different ALs when varying the C6 content. ZnPc (blue balls) and C6 (orange balls) are embedded in a C_{60} matrix (grey). Depending on the composition the donor in the minor concentration may act as a sensitizer or interrupt the percolation path (circled) of the donor in the major concentration.

it can not be concluded that the introduction of C6 reduced red light absorption (550 to 800 nm) further. The differences between the measured SR and absorption spectra are comparable with regard to the AL composition. As expected from the absorption coefficients, the ratio between the Q and Q^+ bands varies due to the dilution of the ZnPc concentration. The peak of smaller aggregates rises slightly at the expense of the peak due to larger aggregates. Furthermore, the relative optical impact of C6 in the SR spectrum is less distinct than predicted by the absorption spectra.

Overall, the photoconductivity increases with the amount of C6 in the AL. This photoconducting property of C6 has also been investigated in the binary C_{60}:C6 mixture.[144] The opposing effects of adding C6 such as increasing the series resistance due to the rising disorder on the one hand and reducing the resistance because of the photoconductivity on the other hand, reveal a lowest series resistance for 10% C6, *vide* figure 5.3 b, green curve with triangle. By enhancing the C6 amount, the *FF* falls from 58.7% to 42.9% with a pronounced drop after rising the C6 content from 10% to 15%. At 15% C6 the *J*-*V* curve shows a distinct loss of a rectangular shape, and a suggestion of a kink can be seen.

The presence of a kink could be explained by the existence of extraction barriers. Figures 5.5 and 5.6 present a possible explanation, which will be also applicable for systems described later. Figure 5.5 shows how the composition variation might affect the bulk layer. From the left to the right, the C6 concentration is enhanced from 0% to 15%. The binary blend is characterized by almost closed percolation paths. Holes will be transported *via* ZnPc and electrons *via* C_{60} to the corresponding transport layers. Adding a slight amount of C6, the C6 molecules can then only cover some ZnPc clusters and are directly connected to C_{60}; they will hardly interrupt the percolation path of ZnPc. They may act as antenna molecules for

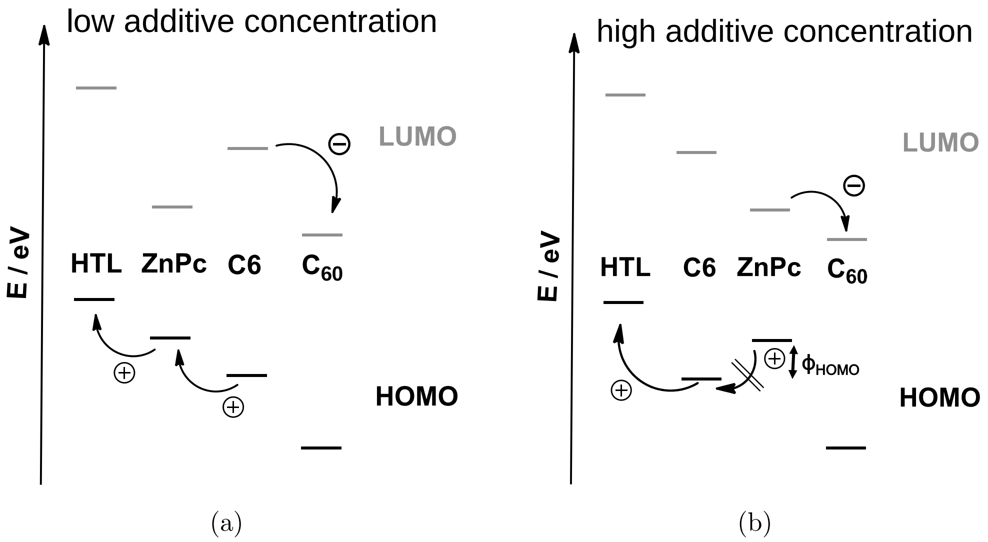

Figure 5.6: Schematic of the occurring extraction barrier ϕ for the system C_{60}:ZnPc:C6 depending on the energy levels of the HOMO (black) and LUMO (grey) levels. (a) At low C6 concnetrations, the C_{60}:C6 interface are close to ZnPc percolation paths. Holes can move towards the HTL by utilizing ZnPc molecules. For high concentrations of C6 the formation of a hole extraction barrier (ϕ_{HOMO}) is apparent due to the likely interruption of the ZnPc transport ways.

ZnPc (images in the middle). However, after exceeding a threshold concentration, C6 molecules will not only be connected to the ZnPc agglomerates, but also to each and C6 clusters are more likely, which will interrupt the ZnPc percolation paths to the transport layers.

For the last scenario, a hole extraction barrier exists as shown in figure 5.6 b. Since we assume that C_{60} is present in excess, all electrons will be transported through C_{60} molecules after exciton generation. Only the hole extraction barrier has to be taken into account (approx. 0.3 eV). At a low C6 concentration, where the hole can directly be transferred to ZnPc, no barrier has to be surmounted. However, when the ZnPc transport path is interrupted it becomes necessary for holes to have to surpass C6 aggregates in order to enter the ZnPc network. However, the HOMO level barrier inhibits a proper hole extraction. The probability of this occuring rises with the C6 concentration and is especially significant when the C6 concentration (15%) is close to the ZnPc concentration (20%).

In order to investigate the aforementioned extraction barrier, test samples were fabricated where a pure layer of the other donor has been inserted between the hole transporting layer and the binary blend layer. For comparison, a reference sample without this pure interlayer were also fabricated. The *J*-*V* characteristics and the SR spectra are shown in figure 5.7. The key parameters of the solar cells are summarized in table 5.8.

The binary C_{60}:C6 blend solar cell shows a *J*-*V* behavior which is typical for this

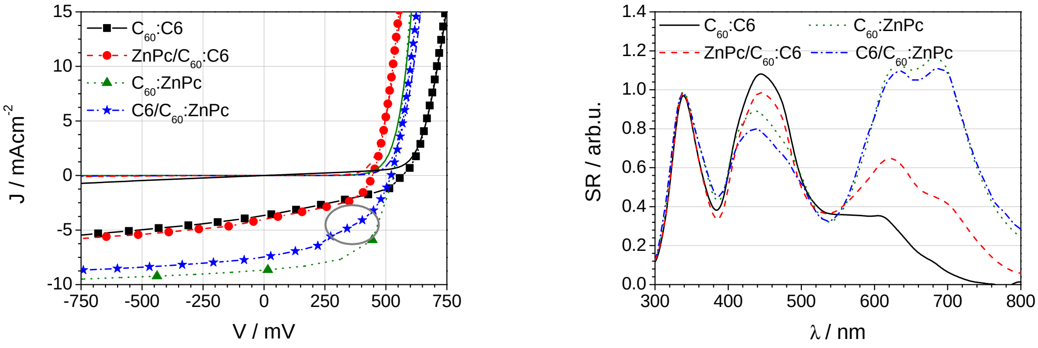

(a) (b)

Figure 5.7: (a) *J*-*V* curves of the test samples for extraction barrier investigations as well as their (b) SR spectra.

Table 5.2: Solar cell parameters of test samples^{a} for extraction barrier investigations.

AL	V_{OC} / mV	J_{SC} / mAcm^{-2}	FF / %	η / %
35 nm C_{60}:C6	579	3.70	34.7	0.75
5 nm ZnPc/ 30 nm C_{60}:C6	451	4.13	50.7	0.95
35 nm C_{60}:ZnPc	537	8.61	59.1	2.74
5 nm C6/ 30 nm C_{60}:ZnPc	519	7.46	45.1	1.75

[a] glass/ 130 nm ITO/ 50 nm p-HTL/ 35 nm D_1:A blend or 5 nm D_2 + 30 nm D_1:A blend/ 20 nm EBL/ 10 nm n-ETL/ 200 nm Al.

architecture. The *FF* is, with 33% low, but the V_{OC} is, with 579 mV, much higher than for ZnPc containing blends (537 mV). The SR spectra reveal a strong absorption between 400 and 500 nm and a shoulder which flattens more up to 600 nm. With the addition of a pure ZnPc layer in front of the blend (ZnPc/C_{60}:C6), the V_{OC} decreases to 448 mV, but the *FF* dramatically improves to 51%. The serial resistance seems to be slightly lower as well. The improvement of J_{SC} is small. The pure ZnPc layer can also be inferred from the SR measurements. The band which is typical for dimeric ZnPc species dominates the spectrum from 550 to 750 nm. This means that excitons which have been generated on ZnPc molecules could be separated at a C_{60} interface. Either the excitons have diffused to the ZnPc/ C_{60}:C6 blend interface and separated there or the exciton could also be transferred to C6 molecules.

Regarding the opposite experiment, the insertion of a pure C6 layer did not much influence the value of V_{OC}, but drastically reduced the value of *FF* from 59% to 45%. No influence on the serial resistance was observed. However, a distinct kink (circle) appears in the fourth quadrant. This is definitely due to the extraction barrier caused by C6. Interestingly it seems that the pure C6 layer did not contribute to the photocurrent as the pure ZnPc layer did in the corresponding experiment. Futhermore, the photocurrent was also reduced in the ZnPc related

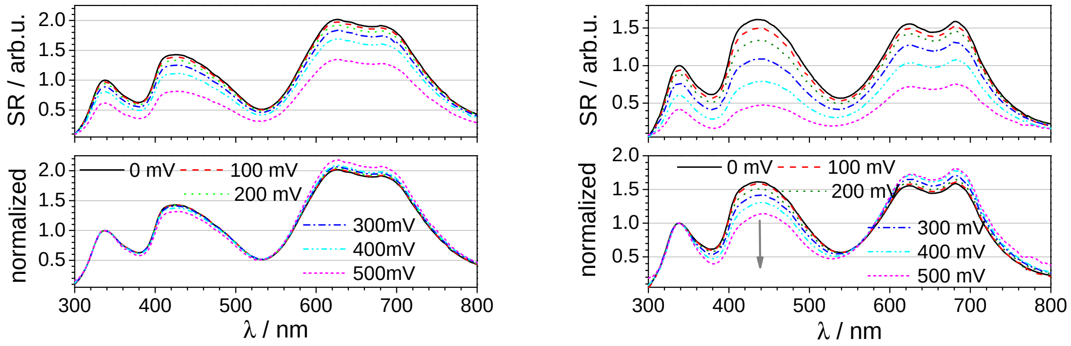

(a) (b)

Figure 5.8: Voltage dependent SR spectra for an organic solar cell with binary C_{60}:ZnPc (a) and the corresponding ternary blend with 15% C6 (b) as absorption layer.

bands which confirms the existence of an extraction barrier.

Performing voltage dependent SR measurements confirmed the impact of the extraction barrier. The corresponding graphs are shown in figure 5.8 for the binary C_{60}:ZnPc (a) and the ternary system (15% C6, b) in the AL. Although the V_{OC} value is lowered from 542 to 514 mV, a reduction of the SR signal with rising applied bias can be neglected at this extent of applied bias. With its increase, the SR signal drops due to the increased recombination probability. Hence, this technique is very sensitive to trapping sites and results in a change of the spectral shape. Therefore, the spectra are also normalized. Whereas the binary reference sample shows almost no change in the curve characteristics except for the recording at 500 mV, which is very close to V_{OC}, the normalized spectra of the ternary system on the other hand are featured by a distict shape variation with the applied bias. Because the hole mobility for blended systems is usually lower than the electron mobility, recombination sites can easily be assigned to the donor molecules. Irradiating the device with blue light will lead to an increased field intensity close to the cathode which means that holes generated by C6 absorption have to cross the longest pathway. Hence, their likelihood to recombine is relatively high. Contrary to the field maximum of blue light, the long wavelength light is concentrated closer to the anode. Hence, holes originating from ZnPc have to overcome on average a shorter distance to reach the HTL and it seems to be easier for them to leave the AL with rising applied bias than for holes related to C6 transitions (*cf.* figure 5.4). Due to normalizing the spectra at the 340 nm peak, it appears that the ZnPc peak rises and less recombination takes place, which is not the case. Finally, it can be concluded that more traps exist in tri-component absorption layers than in binary systems.

For V_{OC}, it is interesting that this parameter fall with the concentration of the C6 donor. With the addition of a second donor, one would expect that (i)

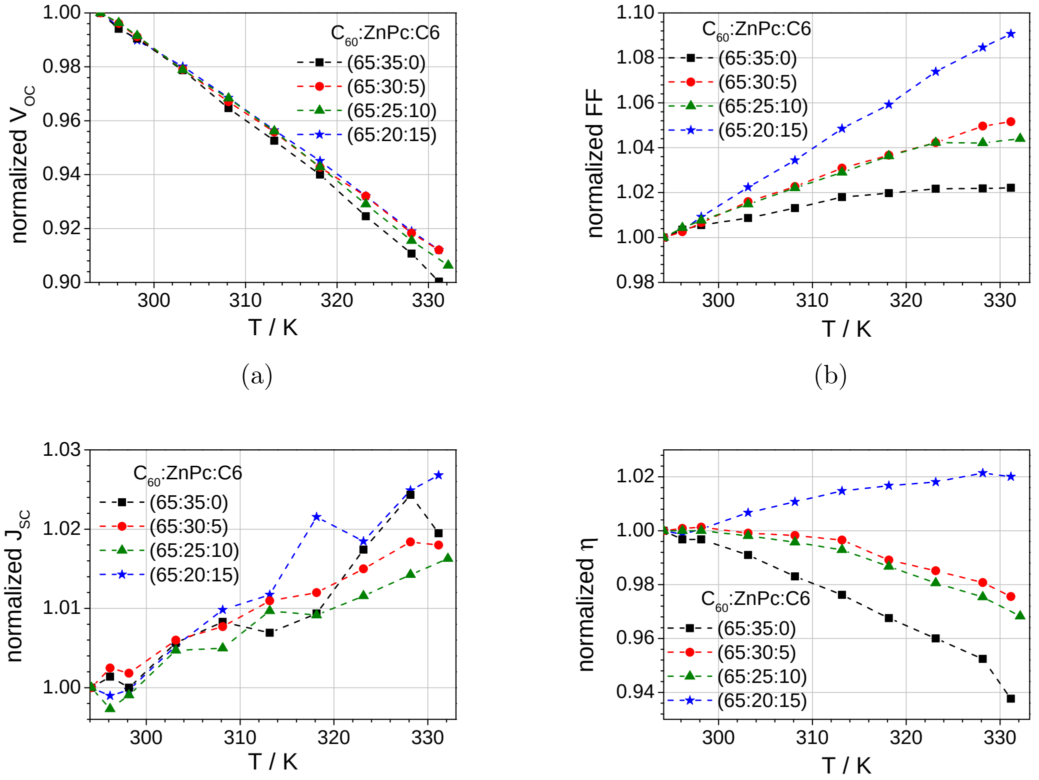

(a) (b)

(c) (d)

Figure 5.9: V_{OC} (a), FF (b), J_{SC} (c) and η (d) in dependence on the measurement temperature. For better comparison, all parameter are normalized to their value recorded at 293 K.

V_{OC} varies between those of binary blended C_{60}:ZnPc (500 mV) and C_{60}:C6 cells (600 mV) or (ii) that the cell parameters are dominated by one donor and behave similarly. With the reduction of the donor in the C_{60}:ZnPc blend, V_{OC} increases (described in Chapter 3 and literature[68]). Furthermore, when increasing the donor concentration in the C_{60}:C6 blend, the cells resulted in higher V_{OC} values. So, one would expect that the ternary composition as chosen here should benefit from the introduction of C6 molecules as the ZnPc concentration is reduced and the C6 amount increased. However, V_{OC} declines. In order to investigate this phenomenon further, the dielectric constants ϵ_r for the different AL mixtures have been determined. Apparently, the V_{OC} decreases with rising ϵ_r, which is in accordance with results from the experiments of binary C_{60}:C6.[144] Surprisingly, ϵ_r increases with rising C6 content in ternary systems, which is in contrast to the binary C_{60}:C6 reference system.[144] Additionally, from the presented temperature dependent measurements, we can assume a minor change of the Fermi level position because of the very similar behavior.

Since it is known that organic solar cells tend to improve their efficiency with rising temperature, the measurement temperature was varied for the devices with the binary AL and the tricomponent systems C_{60}:ZnPc:C6 = 65:30:5 and 65:20:15.

Table 5.3: Comparison of the key values in dependence on the blend composition measured at 25 (white row) and 55 ℃ (grey row).

C_{60}:ZnPc:C6	ϑ / ℃	V_{OC} / mV	J_{SC} / mAcm^{-2}	FF / %	η %
65:35:00	25	536	8.68	59.0	2.77
65:35:00	55	493	8.89	60.0	2.64
65:30:05	25	533	7.71	55.8	2.29
65:30:05	55	491	7.82	58.2	2.25
65:20:15	25	510	6.87	42.7	1.50
65:20:15	55	473	7.00	45.9	1.53

In principle, V_{OC} decreases whereas J_{SC} and FF rise. Depending on the magnitude of the increase in the parameter values, the decreasing V_{OC} can be compensated and thus, the efficiency of a solar cell can improve with rising temperature. The resulting temperature dependency of each key value is depicted in figure 5.9 and for 25 and 55 ℃ summarized in table 5.3. Clearly, the behavior of each key value is similar for all sample types. However, the extent of the temperature dependency is different. As expected, V_{OC} falls linearly with the temperature for all samples. The C6-free sample drops here with -1.43 mVK^{-1} in the strongest extent, and decelerates with rising C6 content to -1.20 mVK^{-1}. J_{SC} tends to rise, however because of the small rise it can hardly be differentiated from the measurement uncertainty. With respect to *FF*, this parameter strongly improves with the applied temperature. The higher the C6 amount was in the sample, the higher was the improvement of *FF*. With rising C6 content, the *FF* increases of 0.04%K^{-1} for the C6-free sample up to 0.11 %K^{-1}. The parallel resistance changes marginally, resulting in equal rectification ratios for each temperature. In contrast, the series resistance seems to improve and to yield better fill factors.

The reduction of R_S originates from the better charge carrier mobility because of the thermally activated hopping transport mechanism. The graphs in figure 5.9 show thermal activation for all samples, but it improves on C6 molecule sites stronger than on ZnPc sites. This improvement is for the ternary blend with 15% C6 so distinct, that it can compensate the V_{OC} loss and give a rising power efficiency with increasing temperature compared to the binary reference blend.

5.1.3 Summary

Coumarin 6 was introduced as a sensitizing dye in the classical C_{60}:ZnPc blend. Although the absorptive range of the cell was extended, the cell performance dropped. This is attributed to both a reduced exciton generation efficiency and a reduced charge collection efficiency. Furthermore, the variation of composition influenced the polarization energies and yielded lower *FF* and V_{OC} values. The existence of an energy barrier to hole extraction has been proven. As predicted by Tress

Table 5.4: Summary of the key values of OSC with C_{60}:PTCBi:ZnPc as absorption layer in dependence on its composition as well as the investigated decay of the SR signal (ΔSR) after applying 400 mV.

C_{60}:PTCBi:ZnPc	V_{OC} / mV	J_{SC} / $mAcm^{-2}$	FF / %	η / %	S	ΔSR / %
67 : 00 : 33	567	7.34	57.9	2.42	1.20	8.8
64 : 03 : 33	554	6.89	55.0	2.11	1.28	16.1
59 : 08 : 33	553	6.41	42.9	1.53	1.59	24.5
50 : 17 : 33	563	5.61	44.3	1.40	1.44	29.1

and co-workers, that an extraction barrier larger than 0.2 eV can lead to massive extraction problems,[15] the value of J_{SC} suffers most with introducing C6 as additive. Although the performances of ternary blended solar cells is worse than the binary reference, they showed a better temperature behavior. Due to the better thermal activation ability of the charge carrier mobility on the C6, the reduction in V_{OC} could be compensated for in the ternary mixture with the highest C6 amount, and the efficiency then increased.

5.2 C_{60}:PTCBi:ZnPc Ternary Blends

5.2.1 PTCBi as Acceptor Material

In contrast to the two systems presented before, here the influence of a third component with acceptor character is investigated. Along with fullerenes, the material class of the perylene derivative represent a further group of acceptors.[168,169] For our experiments, we have chosen 3,4,9,10-perylenetatracarboxylic *bis*-benzimidazole (PTCBi) due to its high absorption coefficient over a broad range and high diffusion length of around 12 nm in the stacking direction.[168] Because of the planar structure of PTCBi, in comparison to C6 it is expected to disturb the aggregation process of ZnPc less.

For this system, the acceptor content was set to 67%. This high concentration was chosen in order to make negligible any possible interruption of the C_{60} percolation path. The content of PTCBi will not exceed the value of 25% of the acceptor material.

5.2.2 Characterization of Ternary OSC

Three tricomponent samples as well as the binary C_{60}:ZnPc reference sample have been fabricated. The measured *J*-*V* curves under illumination and in the dark are depicted in figure 5.10. The achieved key values are summarized in table 5.4. Compared to the other ternary system discussed here, this one behaves differently.

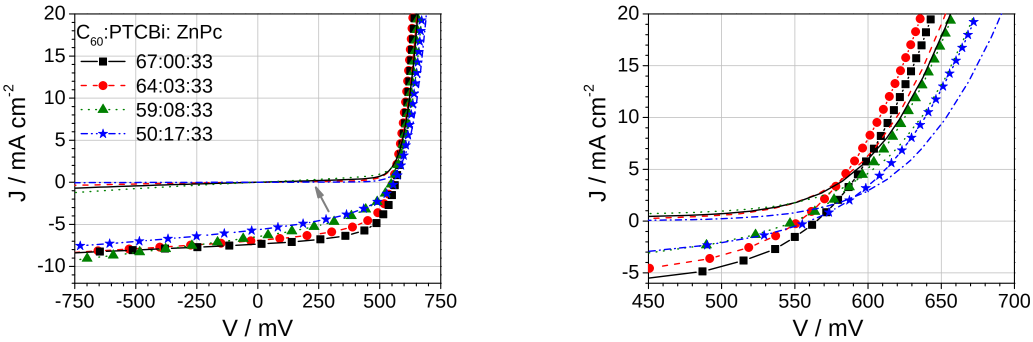

(a)

(b)

Figure 5.10: (a) *J*-*V* characteristics of OSC with C_{60}:PTCBi:ZnPc as absorption layer under illumination (line + symbol) and in the dark (line) in dependence on the blend composition as well as (b) its detail.

Although an initial decrease in the performance with concentration is seen, some of the key values recover and start to increase from a PTCBi content of 17%.

With regard to J_{SC}, this parameter drops with rising PTCBi amount, which correlates mainly with the *FF*. Considering the lower absorption coefficient of PTCBi compared to those of C_{60} and ZnPc, it is surprising that the absorption of the solar cell device did not decrease more. According to the absorption and spectral response spectra (*cf.* figure 5.11 a), a better sensitivity relative to the sun spectrum could be achieved. Due to the absorption band overlap of PTCBi and ZnPc between 500 and 700 nm, the development of the ZnPc Q band has to be discussed as a superposition of these two materials.

For ease of comparison, the normalized ternary SR spectrum (C_{60}:PTCBi:ZnPc = 50:17:33) is subtracted from the normalized binary reference spectrum and is displayed in figure 5.11 b. According to the black curve, the sensitivity increase from 500 to 700 nm can neither be directly assigned to PTCBi nor to ZnPc, moreover still an overlap seems to be present. Because the Q band did not rise compared to the peak at 340 nm, it is assumed that PTCBi had a weaker impact on the ZnPc aggregation behavior than the structurally distored small molecules DCM and C6. This seems reasonable due to the constant ZnPc concentration. Hence, the reduced *FF* is more likely related to recombination processes than to the serial resistance increase.

After initially decreasing with the addition of PTCBi, the V_{OC} eventually reaches almost the reference value of the binary system. No clear trend for V_{OC} can be seen, given the measurement uncertainty. Indeed, the open circuit voltage is expected to be independent of the PTCBi concentration. Comparing the LUMO levels of C_{60} (4.0 ± 0.4 eV) and PTCBi (4.0 ± 0.6 eV) shows that they can be considered as identical within the large uncertainty of the literature values (*cf.* table 2.1). It has also been reported by Tress and co-workers that the LUMO level

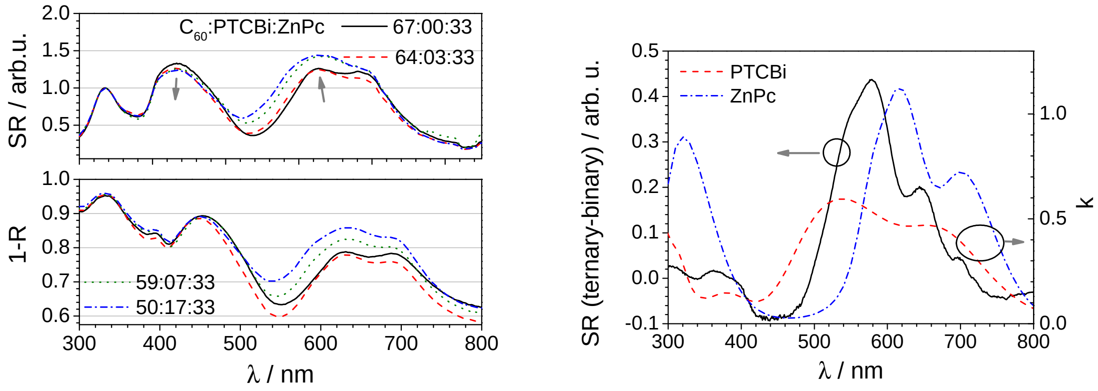

(a) (b)

Figure 5.11: (a) SR and absorption spectra of OSC in dependence on the composition of the C_{60}:PTCBi:ZnPc blended layer. (b) Spectral sensitivity difference between binary and ternary C_{60}:PTCBi:ZnPc solar cells.

of C_{60} is less sensitive to compositional changes within the bulk.[68] Thus, we also assume that a LUMO shift can be neglected and that the resulting effective gap is not affected by the addition of another acceptor material.

In order to investigate recomination effects on *FF* in more detail, voltage-dependent spectral response measurements have been recorded for each sample and are shown in figure 5.12. Adding only a slight amount of PTCBi (3%) had no influence on the recombination behavior, which is in good agreement with the evaluated *FF* of 57.9 and 55.0% for the binary and first ternary sample, respectively. However, when increasing the content from 3 to 6%, not only the *FF* dropped, also the shape of the normalized SR spectra for C_{60} related bands varied significantly, indicating the formation of recombination sites. Interestingly, doubling the amount of PTCBi from 8 to 17% does not lead to a twofold enlargement of recombination; the shape variation with increasing applied bias hardly differs between the 8% and 17% PTCBi samples.

Along with the generation of recombination sites, the PTCBi content also correlates with the serial resistance R_S. The more C_{60} is replaced by PTCBi, the higher is R_S which is not surprising considering the higher charge carrier mobility of C_{60} compared to PTCBi. Less expected is that the tri-component sample with 3% PTCBi resulted in a lower R_S than the binary solar cell. For all samples the resistance reduces under illumination by the same extent, thus PTCBi does not affect the photoconductive behavior of the BHJ blend.

In order to examine the existence of traps, the solar cell samples have been characterized at different measurement temperatures. The impact on the key values is illustrated in figure 5.12. Typically, the open circuit voltage decreases with increasing temperature and there is no discernable difference between the binary and ternary samples. The *FF* and J_{SC} increase with the measurement temperature

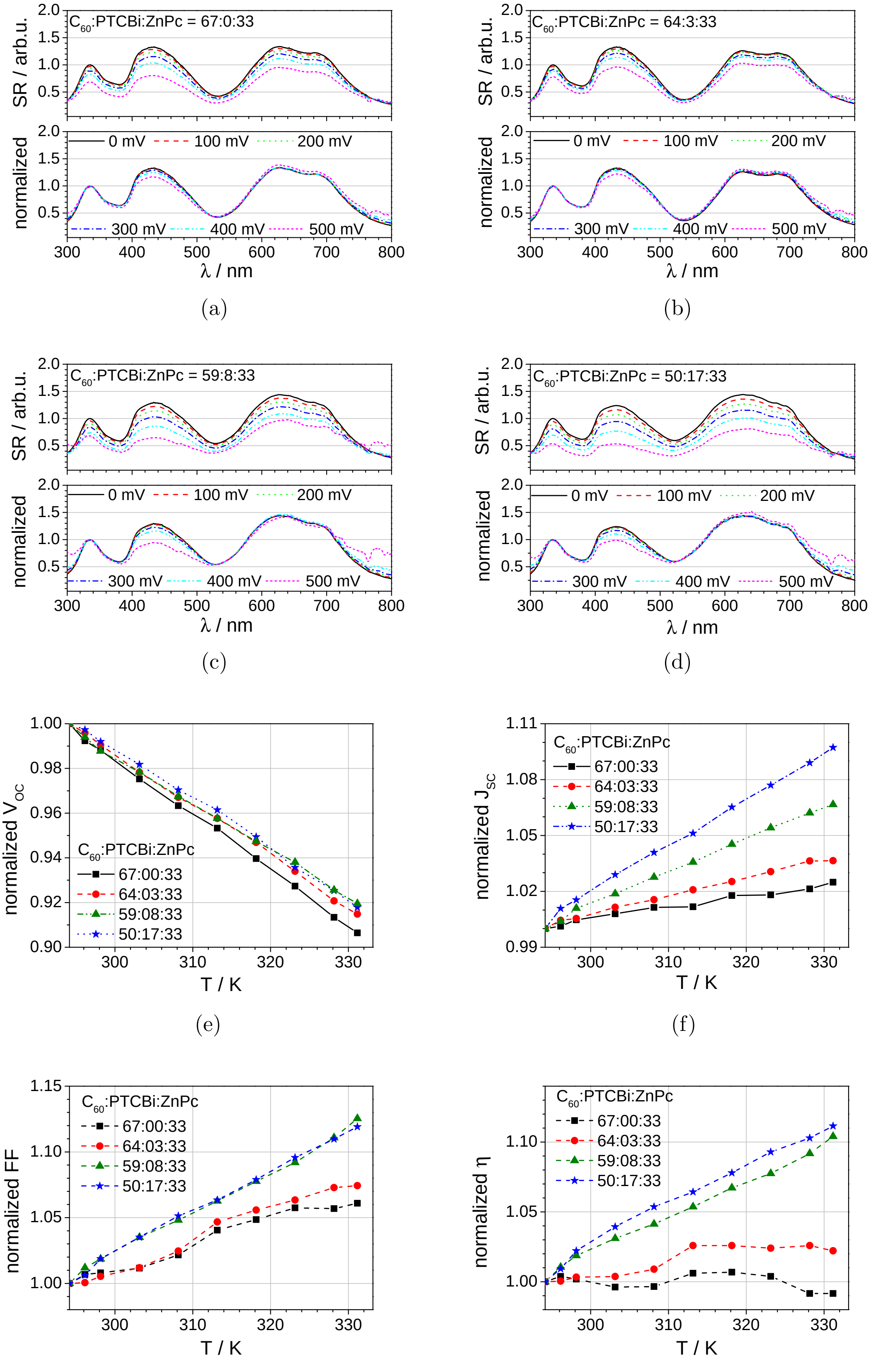

Figure 5.12: Voltage-dependent SR measurements in dependence on the C_{60}:PTCBi:ZnPc composition from 67:0:33 (a), 64:3:33 (b), 59:8:33 (c) to 50:17:33 (d). Temperature dependency of these solar cells for V_{OC} (e), J_{SC} (f), FF (g) and η (h).

due to the charge carrier mobility increase, resulting is a lower serial resistance. Interestingly, the addition of 3% PTCBi seems to show a small impact again considering a similar behavior in *FF* for the binary cell. Furthermore, the improvement of the electrical properties at higher temperature appears similar for 8 and 17% PTCBi. Nevertheless, the best performance improvement exists for the ternary cell with the highest PTCBi content, emphasizing the existence of charge carrier traps.

According to table 2.1, the LUMO levels for PTCBi (4.0 ± 0.6 eV) and C_{60} (4.0 ± 0.4 eV) are identical. However, the uncertainty is very large and, the experiments actually show that the difference between these LUMO levels must be greater than 0.1 eV since a transport barrier this low could have easily been overcome by the electrons.

5.2.3 Summary

Ternary solar cells using two accpetor and one donor material have been fabricated and characterized. Contrary to published values, the energetic mismatch between the C_{60} and PTCBi LUMO was most probably larger than 0.1 eV and led to an continueous increase of recombination sites with addition of a third additive. Thus, the overall performance dropped, although no significant impact was seen for the V_{OC} behavior.

5.3 C_{60}:ZnF_4Pc:ZnPc Ternary Blends

5.3.1 ZnF_4Pc - Fluorination and its Impact on the Electro-optical Properties

Within this material system, the donor materials whose content will be varied are structurally equal in the first approximation and possess similar absorption behaviors, since the optical gap is only slightly different. However, in contrast to ZnPc for which the HOMO and LUMO level are located at around 5.1 and 3.6 eV, these levels are significantly deeper for fluorinated zinc phthalocyanines due to the reduction of electron density in the macrocycle. This lowers the levels by approximately 0.35 eV for ZnF_4Pc in comparison to ZnPc (*cf.* figure 5.13 and literature[43]).

Organic solar cells have been fabricated with compositions of the ternary blend from the binary C_{60}:ZnPc (6:4) to the analog C_{60}:F_4ZnPc (6:4) blended OSC. These samples were characterized under illumination and in the dark and the results are summarized in table 5.5. The corresponding *J*-*V* curves are depicted in figure 5.14. For simplification, V_{OC}, J_{SC}, *FF* and η have been illustrated with variation

Table 5.5: Key values of ternary OSC in dependence on the AL composition of C_{60}:ZnF_4:ZnPc. The acceptor concentration has been kept equal and the donor content has been varied.

C_{60}:ZnF_4Pc:ZnPc	V_{OC} / mV	J_{SC} / mAcm^{-2}	FF / %	η / %	S	ΔSR^a/ %
3.0 : 0.0 : 2.0	539	9.66	58.9	3.08	1.1	18.0
3.0 : 0.2 : 1.8	565	9.64	58.0	3.17	1.1	16.8
3.0 : 0.5 : 1.5	636	8.87	59.3	3.37	1.1	16.2
3.0 : 1.0 : 1.0	681	8.33	51.1	2.93	1.2	24.2
3.0 : 1.5 : 0.5	705	5.12	33.2	1.21	1.6	48.8
3.0 : 1.8 : 0.2	686	3.71	32.9	0.85	1.8	47.8
3.0 : 2.0 : 0.0	615	7.79	55.8	2.69	1.2	19.0

[a] For each sample the SR spetra have been integrated from 300 to 800 nm for 0 and $0.75\times V_{OC}$ mV applied bias. The relative decrease of the resulting area has been determined with $\frac{\int_{300\ nm}^{800\ nm} SR(0\ mV) - \int_{300\ nm}^{800\ nm} SR(0.75\times V_{OC}\ mV)}{\int_{300\ nm}^{800\ nm} SR(0\ mV)} \times 100\%$.

of each zinc phthalocyanine in figure 5.15.

Starting with the binary reference cells, the C_{60}:ZnPc ($\eta = 3.08\%$) related cell outperforms the C_{60}:ZnF_4Pc containing analog ($\eta = 2.69\%$) due to a slightly higher FF and a significantly extended J_{SC}, which can not be compensated by the much higher V_{OC} value of 615.3 mV for C_{60}:ZnF_4Pc compared to 539.4 mV for C_{60}:ZnPc.

C_{60}:ZnF_4Pc-containing BHJ cells using the pin-concept are also known from other publications. Except for the V_{OC} value, the J_{SC} and FF values were in accordance[1] with the work of Meiss and co-workers.[170] At this point it should be noted that the F_4ZnPc used there has the fluorine atoms located at position 3 of the benzene ring, whereas this work used ZnF_4Pc fluorinated at position 4. Further details about its synthesis can be found in the appendix. Semiempirical molecular orbital calculations predict a minor influence of the fluorine atom position on the HOMO level resulting in a difference of around 0.1 eV, as displayed in figure 5.13. The calculated values for the HOMO and LUMO levels of ZnPc and F_4ZnPc are in good agreement with theoretical and experimentally determined values,[15,43] so a slightly lower HOMO level for the ZnF_4Pc used there can be assumed. Further information about the calculation can be found in chapter 7. The key parameters from the model are between those published for the samples using the other fluorinated ZnPc derivative, which used an AL layer thickness of 38 nm. Since both ZnF_4Pc derivatives have similar HOMO levels, our lower V_{OC} of 615 mV, in contrast to the published 730 mV, can be explained by the utilization of different HTL materials with unequal HOMO levels. Meiss *et al.* used *N,N'*-diphenyl-*N,N'*-bis(4'-

---

[1] The following layer sequence was used by Meiss *et al.*: 90 nm ITO, 5 nm n-C_{60}, 10 nm C_{60}, 25 or 45 nm C_{60}:ZnF_4Pc, 50 or 40 nm p-HTL, 100 nm Al. For the 25 nm thin AL thickness key values of J_{SC} = 6.6 mAcm^{-2} and FF = 60% were obtained and for the 45 nm thick AL values of J_{SC} = 9.2 mAcm^{-2} and FF = 50% were achieved. The V_{OC} value were 730 mV in both cases.

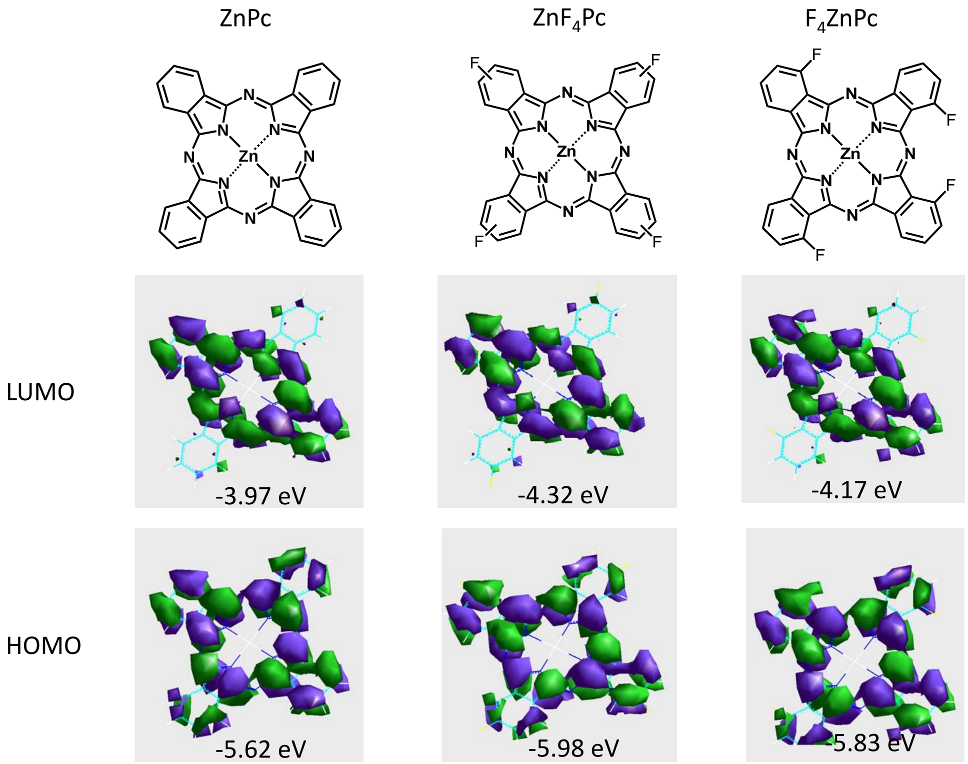

Figure 5.13: The chemical structures of ZnPc, its two tetra-fluorinated derivates and their corresponding molecular orbitals for the highest occupied and lowest unoccupied energy level from semi-empirical calculations. The ZnF_4Pc in the center was used for our studies.

[*N,N'*-bis(naphth-1-yl)-amino]-biphenyl-4-yl)-benzidine (Di-NPB) with a HOMO level of 5.33 eV,[170] which is about 0.2 eV lower than the spiro-TTB used here with 5.1 eV. Since the HOMO level of the HTL tremendously influences the absolute value of V_{OC},[15] the relatively low value of 615 mV can be explained. Thus, the HOMO level of the HTL is more suitable to the HOMO of ZnPc than for ZnF_4Pc. To make comparison easier the HTL material was not changed while varying the composition of the ternary blend.

5.3.2 Ternary Solar Cells with ZnF_4Pc

With variation of the composition of the ternary blend, an interesting behavior was observed. As often seen before, the J_{SC} drops as soon as a third component is added. Astonishingly, the system C_{60}:ZnPc seems to be more resistant against another 'impurity' than the C_{60}:Zn_4Pc system, which drops half the value of the reference value after changing 10% of the donor. Starting from the binary C_{60}:ZnPc blend, J_{SC} falls continuously while increasing the ZnF_4Pc content reaching a minimum at C_{60}:Zn_4Pc:ZnPc = 3:1.8:0.2. But the drop is tremendous after ZnF_4Pc exceeds 50% of the donor material. In order to understand this behavior,

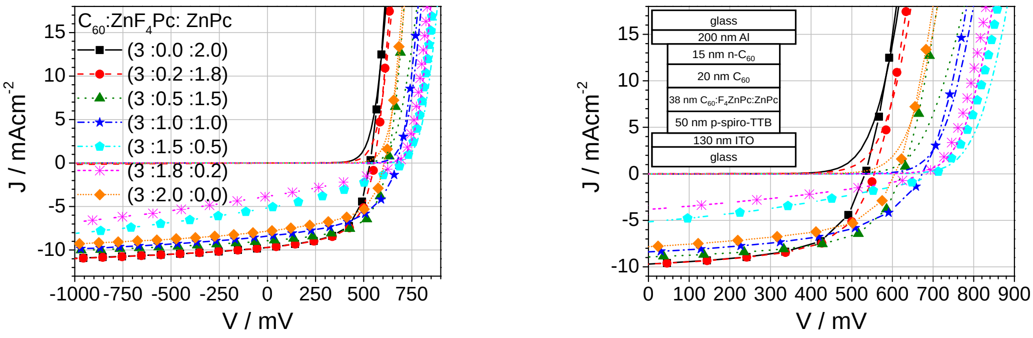

(a) (b)

Figure 5.14: (a) *J*-*V* curves of OCSs with ternary C_{60}:ZnF$_4$Pc:ZnPc absorption layers for variation of the donor material composition under illumination (line + symbol) and in the dark (line) as well as (b) its detailed presentation. The inset in (b) shows the stack architecture used.

absorption spectra as well as spectral response measurements of the devices were recorded and are displayed in figure 5.15 c.

Comparing the absorption spectra, the main variation takes place in the Q-bands where both the fluorinated and unfluorinated ZnPc strongly absorb. Here, the absorption scatters in the range of 7%. According to the SR spectra, there is a significant variation of the C_{60} and zinc phthalocyanine bands. Except for the binary C_{60}:ZnF$_4$Pc sample, the contribution of C_{60} increases with rising ZnF$_4$Pc content, whereas the spectral sensitivity of zinc phthalocyanine bands decreases. In order to understand this further, voltage dependent SR measurements were recorded to isolate the samples with the strongest recombination processes. These spectra are displayed in figure 5.16. For all samples, the SR signal decreases with the value of the applied bias. *I.e.*, it becomes more difficult for charge carriers to leave the device before they recombine. It is possible to isolate the prevailed recombination sites: for a balanced recombination, the normalized SR spectra are supposed to resemble each other. In order to achieve comparable results the applied bias had to be adjusted to the changing composition dependent V_{OC} values. For clarity reasons, the signal intensity decay of the unnormalized spectra is calculated from 0 mV to 75% of the open circuit condition and is summarized in the last column of table 5.5. The decay correlates well with the determined *FF*. Both binary samples and those with C_{60}:ZnF$_4$Pc:ZnPc = 3.0:0.2:1.8 and 3.0:0.5:1.5 exhibit *FF* higher than 50% and a relative SR decay lower than 20%. This means that for these 4 samples the recombination is comparable. A detailed look at the normalized SR spectra of the first four devices shows that the recombination occurs equally for holes and electrons, thus a balanced hole and electron mobility can be proposed on both the phthalocyanine and C_{60} sites. The shape of the decay is nearly equal for these samples and the relative decay varies from 18.0 to 24.2%, so it drops by the

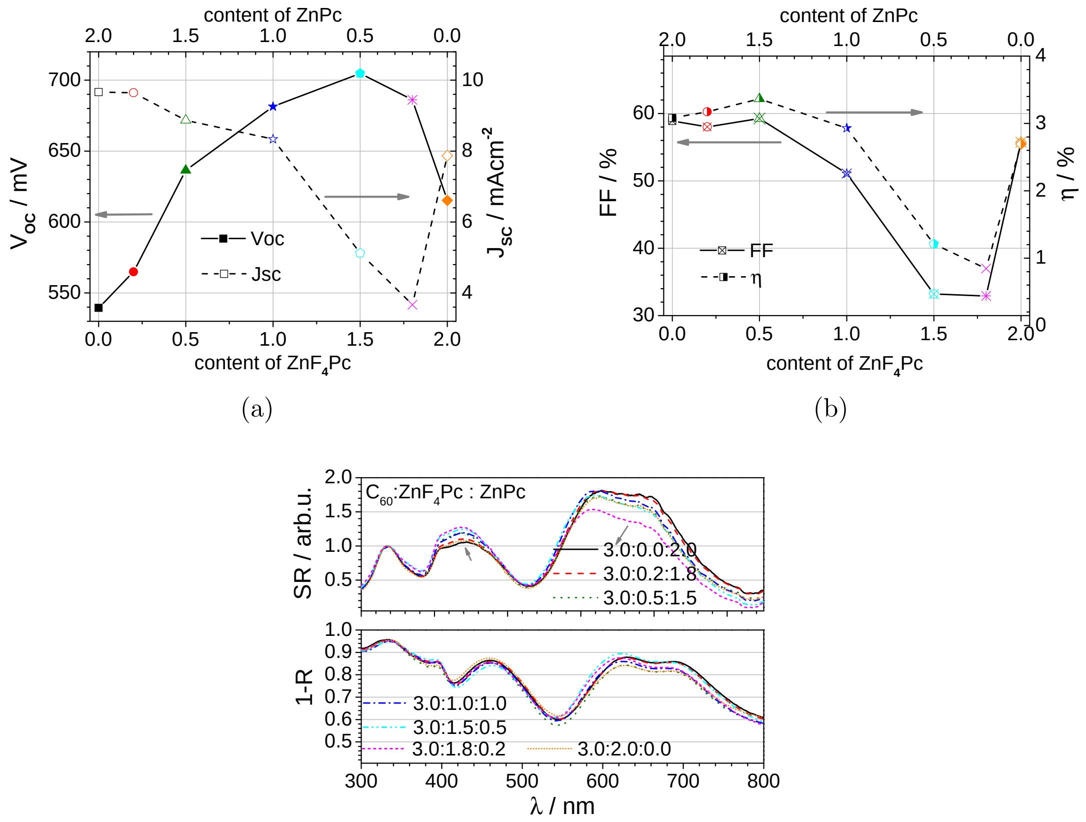

(a)

(b)

(c)

Figure 5.15: Comparative presentation of the behavior of V_{OC}, J_{SC} (a), FF and η (b) *vs.* the ZnPc and ZnF$_4$Pc content.(c) The absorption spectra of the OSC devices (top) as well as their corresponding sensitivity spectra (bottom).

same magnitude. This means as long as the content of ZnF_4Pc does not exceed the amount of ZnPc, a balanced charge carrier transport can be realized.

On the other hand, the SR spectra for the C_{60}:ZnF_4Pc show already that holes originating from C_{60} tend to recombine before they reach the interface. This further supports the idea that the HOMO level of spiro-TTB does not perfectly match the HOMO of ZnF_4Pc. For ternary blends dominated by ZnF_4Pc, the relative decay drops significantly by almost 50% for the samples C_{60}:ZnF_4PcZnPc = 3.0:1.5:0.5 and 3.0:1.8:0.2. Additionally, a clear variation of the normalized SR spectra is apparent for these samples. Charge carriers originating from C_{60} absorption recombine more strongly than those from the phthalocyanine sites. Since the blue region of light is more concentrated close to the cathode, holes separated there have to travel a large distance. If these holes have low mobilities or have to overcome barriers, they will recombine before they reach the transport layers.

The higher the content of ZnF_4Pc becomes, the more probable it is that excitons will be directly formed on ZnF_4Pc and that the closed percolation path of the donor becomes dominated by ZnF_4Pc. After exciton separation, the hole is reliant on this percolation path. However, because ZnPc and ZnF_4Pc are structurally very similar, ZnPc will probably easily insert in a ZnF_4Pc aggregate. This is confirmed by the absorption spectra (*cf.* figure 5.15 c) because no increase of the Q band related to lower aggregation can be observed with variation of the donor composition. Thus, transportation *via* the HOMO level of ZnF_4Pc will be influenced by the HOMO of ZnPc. Whereas a hole transfer from the ZnF_4Pc HOMO to the ZnPc HOMO level can easily be realized, the reverse process is impeded, which results in a hole being trapped on a ZnPc HOMO level eventually recombining. The lower the ZnPc content is, the more isolated ZnPc aggregates are formed.

More evidence for trapped holes on ZnPc sites is given by the temperature dependent measurements of J_{SC} and FF, as presented in figure 5.17 a and b, respectively. Except for the binary cells, all samples show an improvement with increasing temperature, and the strongest enhancement is seen for the samples dominated by ZnF_4Pc. With increasing temperature, the charge carrier mobility improves and thus the serial conductivity, and higher temperatures facilitate overcoming the energy barriers. Hence, samples benefit most from deeply located traps. With regard to the J_{SC} plot, it seems that samples with a ZnF_4Pc content less or equal than 50% seem to have no deep traps, since the improvement with temperature is marginal for them. The FF plot shows that the decrease of the serial resistance is apparent for all samples, however, the improvement becomes more distinct as the ZnF_4Pc content increases. In addition, all samples have been characterized by impedance spectroscopy to isolate the trap states (as described

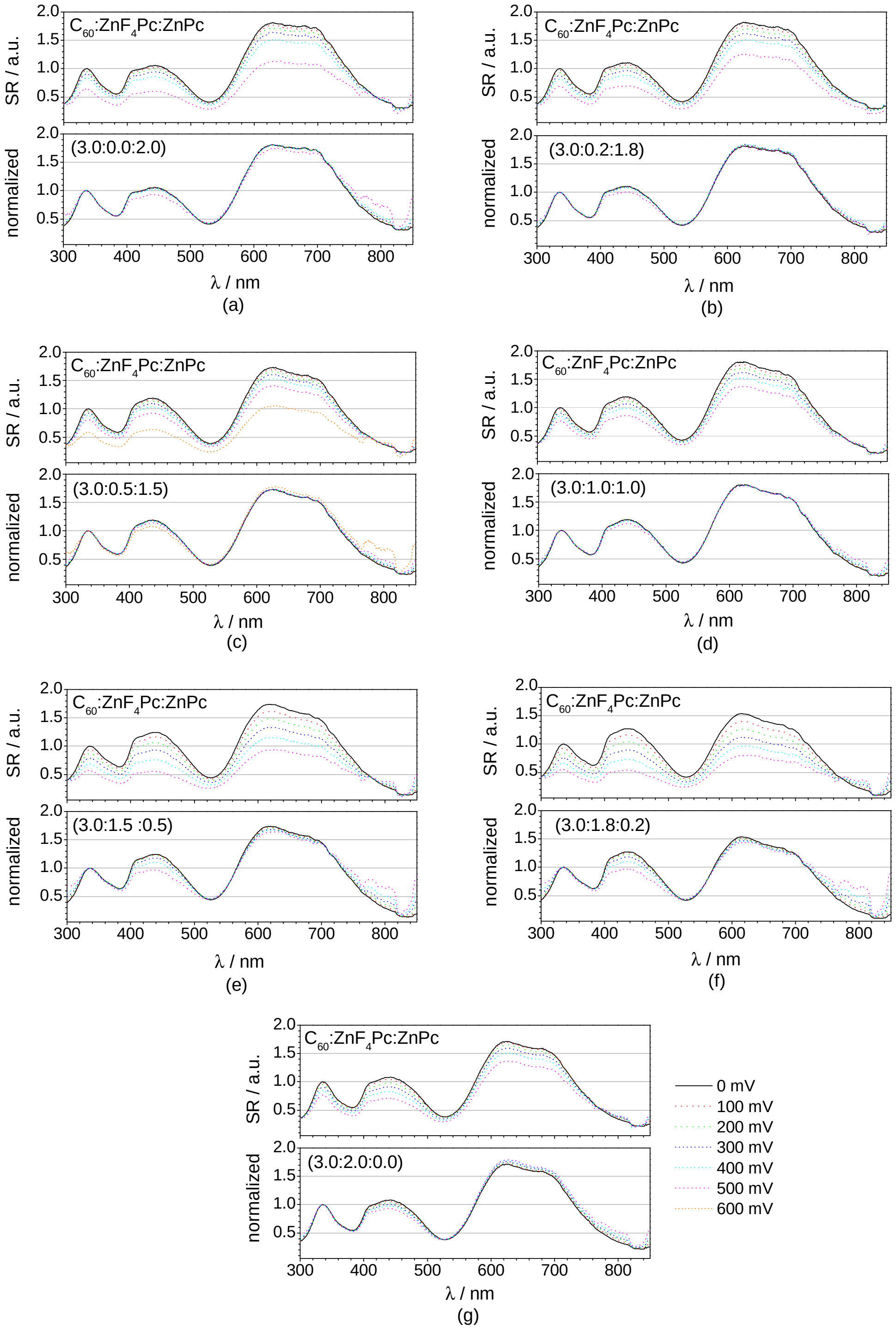

(a) (b) (c) (d) (e) (f) (g)

Figure 5.16: SR spectra of all C_{60}:ZnF_4:PcZnPc samples in dependence on the applied bias as well as their normalized presentation.

by Burtone and co-workers),[171], but the characteristic plateaus in the lower frequency range (*cf.* figure 5.17 f, f $<10^3$ Hz) could not be detected.

In contrast to the other examples investigated, the V_{OC} value increases immediately after a third component has been added. This observation differs from previously discussed ternary systems. One would expect that the V_{OC} can only be tuned between the values obtained for the binary systems as described by Khlyabich and co-workers using P3HT, PCBM and ICBA[2].[166] In that work, a linear V_{OC}–ICBA fraction behavior was investigated for this system and the V_{OC} could be varied from 605 to 844 mV without extensive reduction of the *FF*. Comparable results have also been obtained by Li *et al.* by using the same ternary system, but applying first a pure P3HT layer followed by a PCBM:ICBA mixture.[172] Upon annealing the whole system a mixed ternary blend resulted and the V_{OC} value varied between the binary reference D:A systems. In our case no linear relation for V_{OC} exists from one binary system to the other.

As initially presented in figure 5.15, the V_{OC} variation between the binary reference values has been evaluated. With a composition of C_{60}:ZnF_4Pc:ZnPc = 3:1.5:0.5, the open circuit voltage reaches a maximum of 705 mV, which is significantly higher than the values of the binary references (C_{60}:ZnPc gave 539 mV, C_{60}:ZnF_4Pc gave 615 mV). As already discussed for the *FF* and the temperature dependency of both *FF* and J_{SC}, the existence of trap states is likely, although not detectable by impedance measurements.

High ZnPc Concentrations

Starting from the binary C_{60}:ZnPc reference system, V_{OC} increases when adding ZnF_4Pc. While keeping it as a minority donor material, the *FF* is also not affected by the ZnF_4Pc insertion. For this ternary system, the situation can be described as: (i) the likelihood for exciton generation on ZnPc is higher than for ZnF_4Pc, hence fewer excitons are separated at ZnF_4Pc/C_{60} interfaces than at $ZnPc/C_{60}$. (ii) Once an exciton is separated at ZnF_4Pc/C_{60}, the hole will use the donor transportation paths which are dominated by ZnPc. Thus, holes located at the Zn_4Pc HOMO can reach the HTL HOMO by passing the ZnPc HOMO which is located between these two levels, resulting in an efficient charge carrier transport from Zn_4Pc to the HTL. Because of the low probability of isolated ZnPc aggregates, no barriers have to be overcome and consequently the *FF* remains unaffected by the insertion of ZnF_4Pc.

As often stated in the previous chapters, V_{OC} scales with the effective gap E_g, which is the difference beween the HOMO of the donor and the LUMO of the acceptor. This effective gap correlates as

---

[2] ICBA = indene-C_{60} bisadduct.

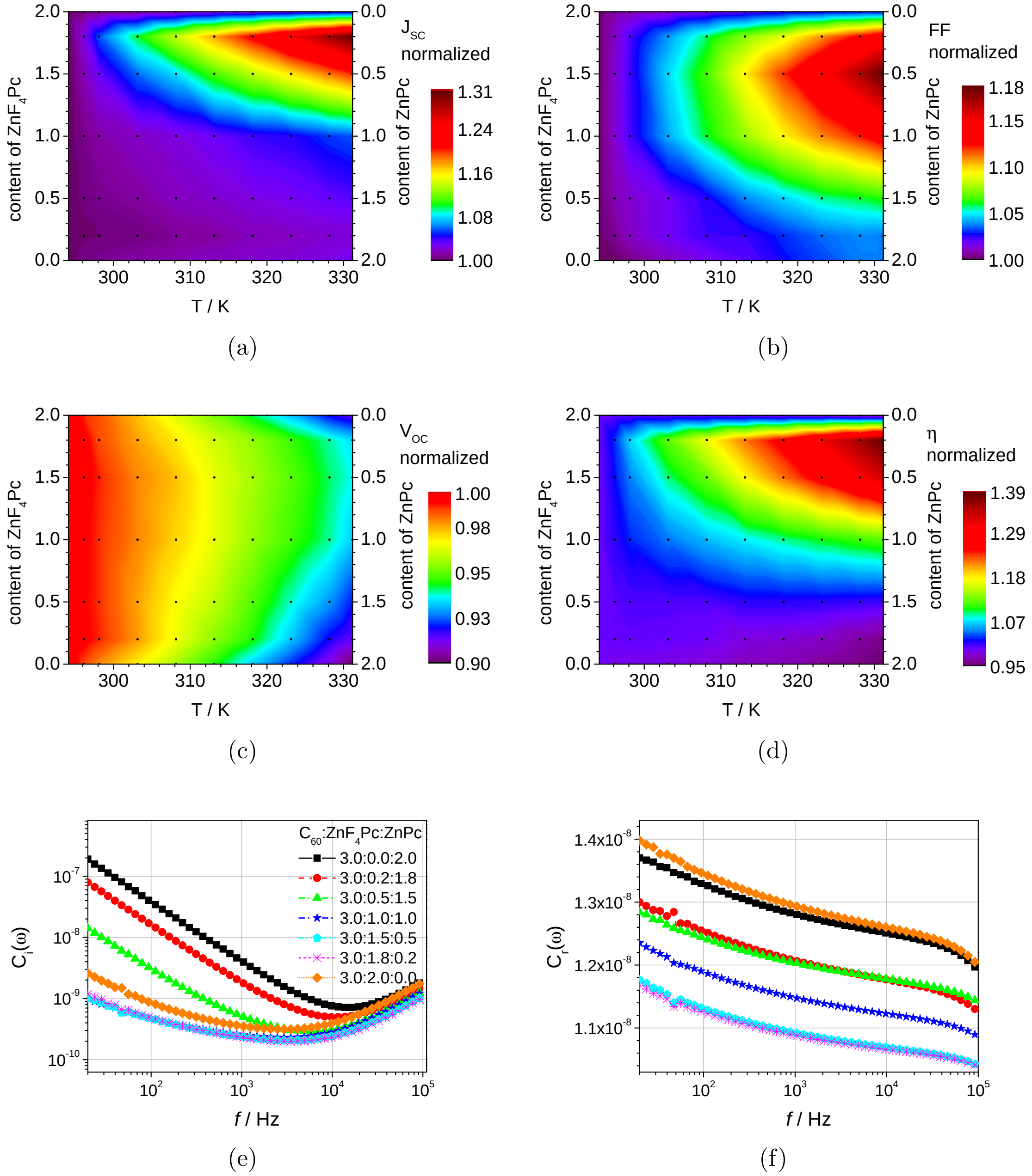

(a) (b)

(c) (d)

(e) (f)

Figure 5.17: Temperature behavior of J_{SC} (a), FF (b), V_{OC} (c) and η (d) for ternary blended OSC for various donor compositions (C_{60}:ZnF$_4$Pc:ZnPc = 3.0:0.0:2.0 → 3.0:2.0:0.0). The quantities have been normalized to their values at 294 K. (e) and (f) show the imaginary and real part of the capacitance of the solar cells as determined by impedance spectroscopy.

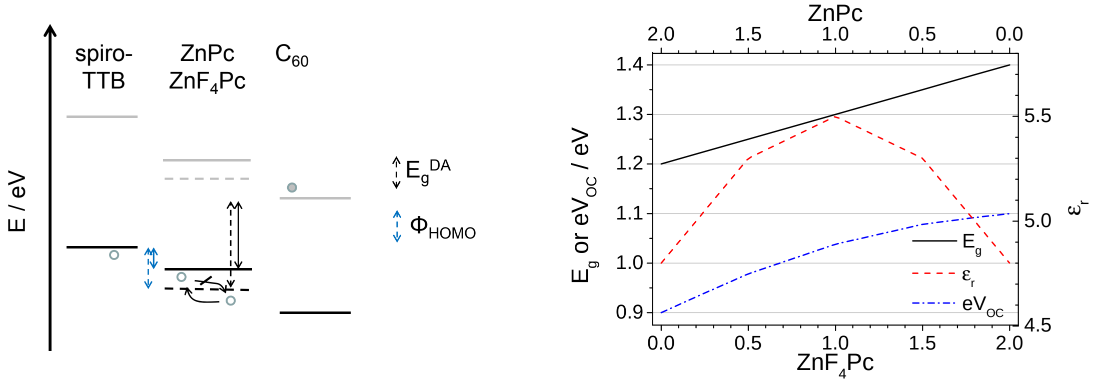

(a)

(b)

Figure 5.18: (a) Schematic of the charge carrier transport via the HOMO (black) and LUMO (grey) level for C_{60}:ZnF_4Pc:ZnPc blends. The energy levels for ZnPc shown as solid lines, those for ZnF_4Pc as dashed lines. (b) Proposed development of the effective energy gap E_g and the dielectric constant ϵ_r to approximate the behavior of V_{OC}.

$$E_g \propto IP_D - EA_A - \frac{e^2}{4\pi\epsilon_0\epsilon_r r_{DA}} \tag{5.1}$$

where the last term correlates with the polarization energy, which changes due to the composition variation. As determined for the C_{60}:ZnPc:C6 series, the measured dielectric constant increased from the binary C_{60}:ZnPc system from 4.9 up to 5.7 after ZnPC and C6 had almost equal fractions. Assuming a similar dielectric constant for the binary system C_{60}:ZnF_4Pc and the highest value of 5.5 for ZnPc:ZnF_4 = 1:1 gives a non-linear behavior of the effective gap[3] as illustrated in figure 5.18 b. The effective gap ranges from 900 to 1100 meV while saturating for high ZnF_4Pc concentrations. The values are higher than the evaluated V_{OC} values, which is not surprising since not all loss mechanisms have been considered here. However, an explanation can be provided for why V_{OC} can reach a maximum for ternary AL while being significantly higher than for the binary reference samples.

High ZnF_4Pc Concentrations

For this case we can assume the following: (i) the likelihood that excitons are generated on ZnF_4Pc is higher than for ZnPc, consequently more excitons are separated at ZnF_4Pc/C_{60} interfaces than at ZnPc/C_{60}. (ii) holes generated on ZnPc have to overcome an extraction barrier of approximately 0.3 eV when passing ZnF_4Pc due to the higher content of ZnF_4Pc, thus ZnPc molecules can be considered as trap sites and thus enhancing the recombination behavior. Under the assumption of relaxed charge carriers and selective contacts (doped transport layers fulfill this

---

[3] $IP_{ZnPc} = 5.1$ eV, $IP_{ZnF_4Pc} = 5.3$ eV, $EA_{C_{60}} = 3.9$ eV. The IP_D has been calculated by the volume fractions of the donor materials.

condition), V_{OC} correlates with the quasi-Fermi level splitting and can reach under illumination without load:[173]

$$eV_{OC} = E_g^{DA} - k_BTln\frac{N_CN_V}{np} \tag{5.2}$$

with (the number of) the electron n and hole p participating in recombination processes and the effective densities of states in the conduction and valence band (N_C and N_V). By replacing np by the expression G/β (generation rate G and recombination constant β), the equation becomes applicable to organic solar cells:[74]

$$eV_{OC} = E_g^{DA} - k_BTln\frac{N_CN_V}{G/\beta}. \tag{5.3}$$

For the ternary compositions C_{60}:ZnF_4PcZnPc = 3.0:1.5:0.5 (ZnPc: 25% as donor) and 3.0:1.8:0.2 (ZnPc: 10% as donor), traps exist whereas the recombination rate should be higherwith the 25% ZnPc as donor than with 10%. Thus, the expression of the term on the right-hand side is smaller for the 25% ZnPc as donor and consequently eV_{OC} is larger. In addition, the very low *FF* is in accordance with this model. The occurence of both mechanisms may qualitatively account for the unusual V_{OC} behavior that was observed.

5.3.3 Summary

The entire ternary bulk heterojunction series from the binary reference systems C_{60}:ZnPc to C_{60}:ZnF_4Pc has been fabricated and charcterized in detail. Due to the similar chemical structure of the zinc phthalocyanines, a negative influence on the charge carrier mobility was not been observed. For the first time, a ternary system based on small molecules has been found which was more efficient than the binary analog (3.08% *vs.* 3.37%), although the total absorptivity of the ternary sample was lower. Despite this fact, the V_{OC} reached a maximum value far beyond that of the binary analogs. This is thought to be due to the change in superposition polarization energy changes and the increase of the charge carrier recombination due to trapped holes on ZnPc sites.

5.4 Impact of a Three-Component Absorption Layer

Organic solar cells containing absoprtion layers with three different tri-component systems have been fabricated considering various aspects. The following conclusions can be drawn:

- The experiments indicate that any transport barrier independent of the size may lead to traps, resulting in a significant drop in J_{SC} and FF.

- The correlation between between the changes in parameters values and the additive concentration is non-linear.
- If the chemical structure of the additive differs too strongly from the compound replaced, the charge carrier mobility decreases due to aggregation inhibition.
- Due to the variation of the chemical structure when using three components instead of two, an increase of the polarization energy can be expected.

From these findings, the following criteria can be proposed for the design of favorable ternary absorption layer blends made from small-molecules:

- The energy levels of the additive must have an appropriate offset with respect to the major donor and acceptor materials.
- The content of the additive with these proposed energy levels should not exceed 50% in order to prevent trap formation.
- The additive should be able to transport electrons and holes as well as the major donor or acceptor material, respectively.
- The additive should not inhibit the crystallization behavior of the major materials, if the major material does not tend to crystallize too strongly. The additive may act as an impurity which results in too small grain sizes. In order to prevent this, structurally similar materials should be used.

Outlook

As outlined in the introduction, a third component is beneficial if the size of aggregates within a binary BHJ is too big and the resulting interfacial area is too small. Because the opposite is generally the case for small molecular OSCs, the successful design of ternary small molecule organic solar cells will be challenging since a similar chemical structure will be required for the additive molecule while a proper offset of the HOMO and LUMO levels from these of the adjacent molecules has to be ensured. However, the increase of the polarization energy shows a good potential to enhance the V_{OC} value. However, since the tailored design of such suggested molecules will be resource consuming, OSC fabricated in the tandem architecture will be the first choice until quantum mechanical calculations allow a more accurate prediction of the molecular and electrooptical properties.

Chapter 6

Conclusions and Outlook

Three different architectural approaches focusing on the absorption layer have been developed and thoroughly evaluated. The first one addressed the absorption layer structure itself by realizing a graded structure, whereas the second approach concentrated on the modification of the light-incoupling layer of top-absorbing solar cells. Finally, a method was explored to broaden the spectral sensitivity of solar cells by depositing tri-component absorption layers.

In chapter 3, starting from the well-studied binary absorption layer model C_{60}:ZnPc, the deposition conditions were modified in order to realize a vertical gradient-like distribution of the acceptor and donor material. Having determined the most suitable deposition temperature to be 85 ℃, the gradient strength and absorption layer thickness were varied and the positive impact of such a graded structure was demonstrated. Although the impact was anticipated to originate only from optical effects, it was shown to also be due to improvements in charge carrier transportation. The main results of that chapter have been published in *J. Phys. Chem. C* **2013**, *117*, 9537-9542.

Based on these results, absorption layers with gradient-like material distribution are a viable approach to fine-tune the efficiency of every bulk heterojunction organic solar cell, significantly contributing to lower production costs per nominal power. However, it is still not clear whether the best gradient is established by a linear or nonlinear change. Since the results determined here indicated an earlier induced aggregation, it is still open how the growth parameters of mass production conditions (such as deposition temperature, pressure and deposition speed) will affect the performance of graded solar cells. When investigating only the electrical effects of gradient-like absorption layers, a donor with similar spectral behavior to the acceptor should be chosen in order be able to neglect the optical benefits of a graded structure; that will allow deeper insights into the physics of this layer architecture. For this purpose, differently fluorinated metal phthalocyanines (e.g.

ZnPc as donor and $ZnF_{16}Pc$ as acceptor) can be used. Various metal phthalocyanines have been synthesized (*cf.* table D.1), but could not have been used for this purpose.

Chapter 4 answers the question of whether highly fluorescent emitter materials can also be useful for solar cell applications. Due to the strong acceptor properties of C_{60}, it has been demonstrated that even the fluorescent dye coumarin 6 is suitable as a donor material (details have also been published in *Thin Solid Films* **2013**, *536*, 206-210). A solar cell architecture has been investigated where efficiently fluorescing layers have been used to increase the photocurrent by increasing the sensitivity in the UV region of light. By implementing a fluorescent light in-coupling layer consisting of Alq_3:DCM in top-absorbing C_{60}:ZnPc solar cells, the UV energy cut off in the light in-coupling layer has been transformed to red emission which significantly contributed to the increase of the short circuit current density. A relation between the emitter dopant concentration and the solar cell performance has been shown, but because of the lack of time the issue of emission quenching at metal surfaces (which was apparent as transparent metal contact) could not be addressed. The first results of this part are in preparation for publication.

These results show that the material class of fluorescent emitters can be utilized to expand the functionality of organic light absorbing devices. Other narrow band absorbing compounds could be investigated to selectively detect photons (depending on the wavelength), allowing the development of lightweight and/ or flexible spectrometer devices. A direct comparison of C_{60}:C6 photoactive cells with a standard silicon based photodiode already showed a higher sensitivity at 480 nm, making these organic diodes attractive for the detection of scintillator irradiation in medical x-ray devices. As it is known that classical HTL compounds act as donors, their implementation as absorbing compound can result in highly UV sensitive photodiodes. Due to the low absorption cross-section of these thin film devices, these designated photodiodes should be less sensitive to energetic particle induced degradation than classical silicon based analogs. Unfortunately, suitable optical simulation tools were not available to consider both the absorption increase in the absorption layer and the efficient incoupling the emission from the light in-coupling layer. The positive effect of emitting light in-coupling layers could probably further be improved by proper optical simulation and layer thickness adjustments. Thus, the development of an optical simulation tool evaluating the absorption and emission behavior of several layers simultaneously within one organic layer sequence would help to further improve the sensitivity of potential photodiodes (*e.g.* with evaporable scintillator materials such as phenyloxazoles in the light in-coupling layer for x-ray detection) and organic solar cells. For these

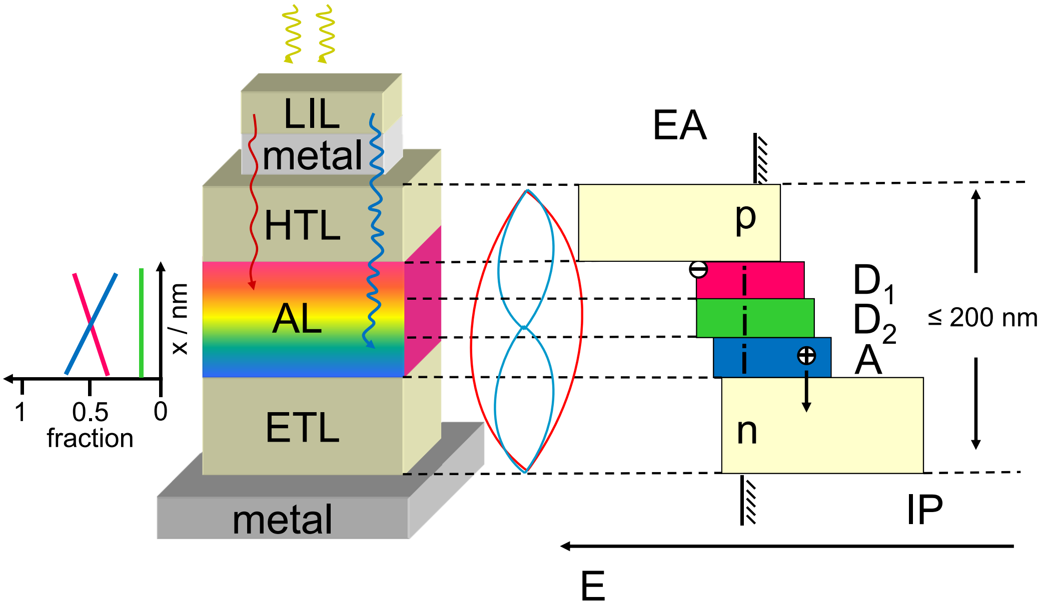

Figure 6.1: Schematic of a potential device architecture implementing all three concepts investigated here. It is proposed that the second donor (D_2) should have its absorption maximum in the spectral range of green light and should be characterized by a lower lying HOMO level than the major donor (D_1) with its absorption maximum in the red to infrared region. For simplificaction it is proposed to keep the concentration of the additional donor (D_2) constant and below the final concentration of D_1. Furthermore, the light incoupling layer can be optically adjusted to best match the absorber material and to down-convert the filtered UV light for charge generation.

purposes, the development and physical characterization of highly efficient emitting materials with strong absorption properties at (very) short wavelengths are necessary.

In chapter 5, ternary absorption layers were explored by investigating three different tricomponent model systems in order to address morphology, sensitivity and energy level issues. After all, the ternary approach increases the complexity of the solar cell architecture and several complementary effects either both lead to a massive performance drop, or to an increase. It has been demonstrated that the spectral sensitivity can be broadened (*cf.* C_{60}:ZnPc:C6), but that the third additive can act as an impurity to inhibit aggregation resulting in a tremendous photocurrent reduction. By minimizing these characteristics for the C_{60}:ZnF_4PcZnPc model system, an overall efficiency increase has been realized. Along with these results, an interesting behavior of the open circuit voltage was observed which could be related to a superposition of two effects: increasing the open circuit voltage by increasing the recombination because of additional trap creation and increasing the open circuit voltage by changing the polarization energies because of the compositional variation. From these results, preparation recommendations have been proposed to create further, novel ternary systems with a broadened spectral sensitivity as anticipated at the beginning of this thesis. Some of the results of this chapter are submitted for publication.

Despite these findings, the reasons for the impact on V_{OC} investigated here are not fully clear, thus requiring further experiments such as:

- the measurement of the CT energies and their relation to the composition of various ternary absorption layers and V_{OC}
- the impact on the crystallization behavior and, if applicable, the performance of XRD measurements
- the influence of the underlying HTL material on the (ternary) absorption layer growth, aggregate size and V_{OC}
- interpretation of the measured data using electric drift-diffusion simulations.

The concept of ternary absorption layers is mainly useful for absorption materials with a strong tendency to crystallize - therefore, their future development will be essential, in particular for the application in small molecular organic solar cells. Once such materials with appropriate electronic properties are isolated, tri-component absorption layers with complementary spectral sensitivity will be a promising concept to increase the device efficiency, in particular by reducing extraction barriers.

Once the ternary absorption layer systems are understood and the resulting key parameters can be accordingly predicted, a combination of all of the concepts investigated in this thesis would make sense, as depicted in figure 6.1. In particular the combination of ternary absorption layers with vertically changing composition appears most promising since it allows both an optimized spectral match and a reduction of recombination sites.

Chapter 7

Materials and Instrumentation

7.1 Organic Compounds

The complete names and corresponding organic structures are presented in table 2.1 and figure 2.1. Spiro-TTB, NPB, MeO-TPD and BPAPF were used as delivered from Luminescence Technology Corporation (Taiwan) or Sensient Imaging Technologies (Wolfen, Germany). Dopant materials NDP-2, NDP-9 and NDN-26 were purchased from Novaled AG (Dresden, Germany). DCM, C6, ZnPc, ZnF_4Pc and C_{60} have been sublimed twice by CreaPhys (Dresden, Germany) prior to utilization and were delivered by Sigma Aldrich (DCM), Lambda Physics (C6), TCI-Europe (ZnPc) and Bucky-USA (C_{60}). ZnF_4Pc was synthesized, further details can be found in the appendix. Aluminum and silver pellets were purchased from Kurt Lesker. Glass substrates for optical characterization were used from Corning International. ITO coated glass substrates were supplied by Luminescence Technology Corporation with an average ITO thickness of 130 nm.

7.2 Organic Molecular Beam Deposition High Vacuum Chamber

For all deposition experiments, a custom-made single chamber high vacuum system (BESTEC GmbH, Germany) was used. As shown in figure 7.1, the vacuum chamber (3) is connected to a glovebox system (2) (MBRAUN). This has the advantage that substrate storage and preparation can be done under a nitrogen atmosphere with water and oxygen concentrations below 0.1 ppm. The plexiglass window of the glovebox was covered with an orange foil to exclude light of shorter wavelengths. The control of the BESTEC tool was done by a computer connected to the server (1), which sends data to the control modules (rate regulation by Inficon, temperature regulation by Eurotherm) and power supplies (TDK Lambda) or receives data from the sensors, respectively. A UV/vis spectrometer (Ocean

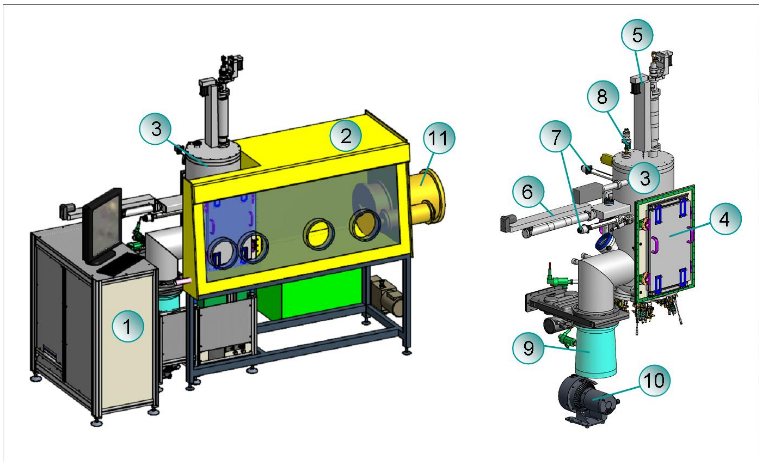

Figure 7.1: Schematic presentation of the BESTEC vacuum chamber.

Optics) was connected via fiber optics through a quartz window the chamber to a tungsten light source (Mikropack). The quality of the vacuum has been monitored by a full range gauge (Pfeiffer Vacuum) suitable for a interval from 5×10^{-10} to 1000 mbar. Vacuum was achieved having by a two-pump system (Oerlikon Leybold Vacuum). A scroll pump (10) evacuates the chamber until a basic pressure of 1.0 mbar is reached. After that the turbomolecular pump (9) provides a pressure of 10^{-7} mbar within 30 min. A residual gas analyzer (SRS RGA300) can be used for characterization of species with mass to charge (m/z) ratio up to 300.

The vacuum chamber itself can be devided into three parts, as shown in figure 7.2 a. The first one (I, also shown in detail in figure 7.2 b) is located at the base of the chamber and consists of the 12 organic molecular evaporators (CreaPhys) filled with alumina crucibles, one metal evaporator with a ceramic heater (CreaPhys) and a high-temperature evaporator (Lesker). A quartz crystal micro balance is located over each pair of the organic and metal evaporators .

The second part (II) is the process position, which is located 64 cm above the evaporation level and does not rotate. Below the substrate attachment, wedge masks from the x- and y-direction (7) can be placed. The substrate and the wedge masks are protected from undesired deposition by the substrate shutter. For substrate heating and cooling experiments (-10 to 190 ℃) a copper block can be placed on the substrate back side, which is fully covered by a metal plate. After the setpoint of the temperature has been reached by the temperature regulation system, the equilibrium state for the substrate is reached after a further 30 min.

The third part (III) of the chamber comprises the storage with 8 storage levels for either mask or substrate trays. This space is protected from depostion by several shields.

For exchanging mask and substrate trays in the closed chamber, an automatic transfer-system including the manipulator (z-direction, (5)) and the fork (x-direction, (6)) can be controlled. The mask-to-substrate mis-alignment is known

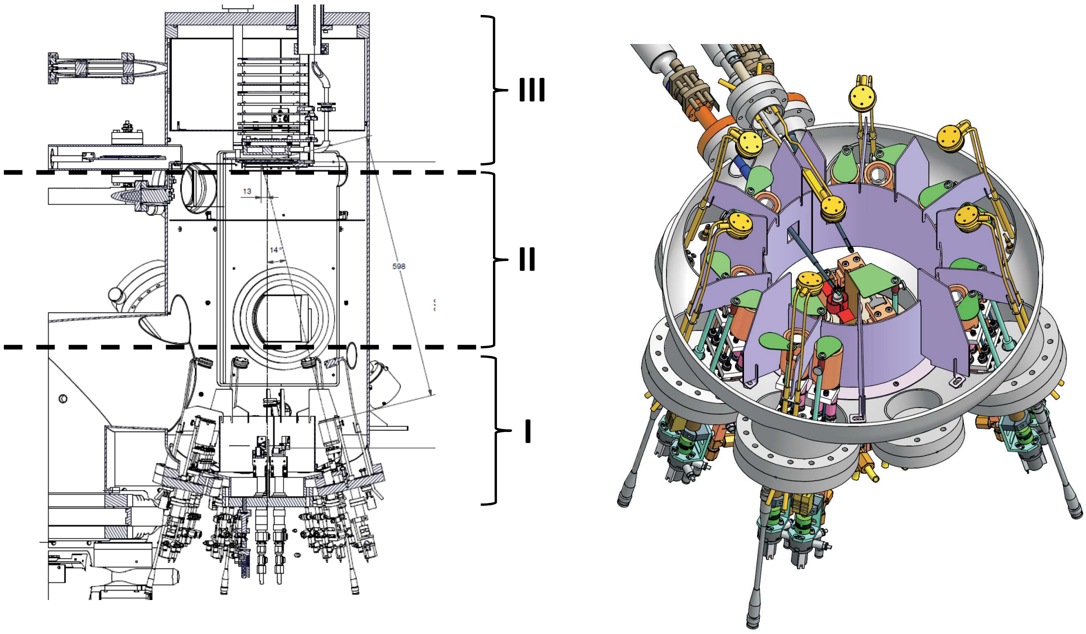

(a) (b)

Figure 7.2: (a) Detailed presentation of the vacuum chamber cross section with its labeled parts and (b) the chamber bottom of the Bestec tool.

to be less than 500 µm. The inhomogenity of organic layers has been determined to be lower than ±3% for an area of 80×80 (mm)^2.

All process sequences are controlled by the Bestec-software which includes the transfer moves, the heating profile of the tempering tool and the deposition itself. All evaporations can be accomplished in either the current or rate regulation mode. Additionally, the deposition of organic material can be controlled by the temperature. All data that are measured with the sensors in the Bestec tool can be logged, normally every second. In order to perform long or complex process steps, a macro-recipe can be written to facilitate the process time management.

7.3 Sample Substrates

Different sample layouts have been used during the execution of this thesis for the fabrication of the OSCs and are shown in figure 7.3. All substrates were 35×50 mm^2 and contain four cell pixels. The cathode C addresses two (OM1211) or all four pixels (OM0013 and OM0016). Each pixel can be actuated *via* the anode pads A in each corner. The OM0013 layout was fabricated by Optrex using lithographic techniques to structure the anodes, the passivation and the electrode pads. Here, the substrate comprises 4 active areas with different sizes of 1.2, 5.0, 19.9 and 79.7 (mm)^2. The OM0016 substrate was fabricated at the COMEDD facilities. Here the anode, the passivation layer and the contact pads

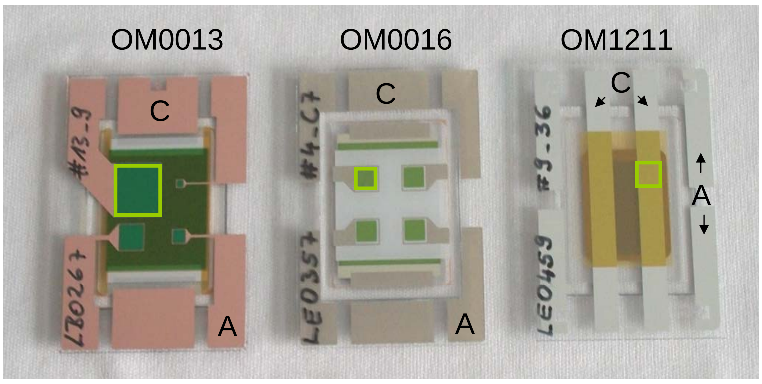

Figure 7.3: Overview of the used sample layouts. The active area is bordered with green.*A* corresponds to the anode and *C* to the cathode.

were structured by screen printing techniques. All four quadrants have the same active area size of 14.9 $(\mathrm{mm})^2$. The OM1211 substrates were also produced at COMEDD and do not have any passivation layer. The ITO covered glass was structured by laser ablation. The active area of 22.2 $(\mathrm{mm})^2$ is defined by the cross section of the striped anode and the cathode, but linearly shaped by shadow masks.

All substrates were cleaned prior to deposition. They were treated with acetone as well as *i*-propanol and have been cleaned in a detergent bath (2% Deconex FPD 211) at 40 ℃ with ultrasound for 7 minutes. After that, they were rinsed with water and *i*-propanol and were dried under a nitrogen flow. Afterwards, the substrates were heated for 20 min on a hotplate at 110 ℃ under nitrogen atmosphere. The cover glasses have been treated with an equivalent cleaning procedure, but they have been dried 120 minutes at 250 ℃. After deposition of the OSC samples, the substrates were encapsulated under a nitrogen atmosphere with a cavity glass (covered with a CaO getter) using UV sensitive glue from Nagase.

7.4 Device Characterization

Solar Measurements

Solar cells were characterized with a characterization tool supplied by AECU-SOFT. It consists of a solar simulator, power supplies and a temperature control tool. *J*-*V* characteristics were recorded using a source measurement unit including a digital multimeter (Keithley 2000 DMM), a Kepco power supply and a test cell (Si solar cell) connected *via* a shuntbox. A metal halide lamp was used to simulate the solar spectrum for global irradiation according to CIE (AM1.5). The illumination intensity was controlled by an EPS module and was kept constant at 100 mWcm^{-2}. The temperature was controlled by a water cooled peltier element and if not otherwise noted fixed at 25 ℃. For temperature dependent measurements, the range was varied between 19 and 58 ℃. Moreover, the measurements were checked for reversibility and reproducibility.

In order to evaluate the measurement accuracy from the illumination source, the contacting and the personal error, illuminated J-V curves of an OSC sample were recorded twenty times every 2 min; contacting was always repeated. A measurement uncertainty (2σ) was estimated for the following parameters: J_{SC} with 0.08 mAcm^{-2}, V_{OC} with 4.4 mV, FF with 0.98% and consequently η with 0.06%. The determination of these data is described in more detail in the appendix.

Conductivity Measurements

The electric doping was monitored using silicon based FET substrates by means of the following relation

$$\sigma = \frac{I \cdot W}{V \cdot d \cdot L} \tag{7.1}$$

where d and I are the measured thickness and current at the voltage V. The length L and the width W of the organic film between the transistor fingers were fixed at 312 mm and 10 µm. The error in the thickness dominates the uncertainty of the evaluated conductivity σ, which is approximately 10%. Typically, the current has been measured at 5 V.

Impedance spectroscopy

Relative permittivity ϵ_r data were determined by C-V measurements with an impedance analyzer (Wayne Kerr 6520B) placing the organic layers between two 100 nm thick aluminium electrodes[1] fabricated on silicon substrates (covered by a native SiO_2 film). The thickness of the organic layers was greater than 350 nm and the roughness of the Al electrode was determined from 3 to 5 nm with a maximum height of 10 nm. The capacity C and the series resistance R were measured from 10^2 to 10^6 Hz and have been plotted. In order to extract the resistance and the capacitance, the curves were simulated considering a capacitor, a resistance and inductor parallel to the measuring instrument. The equivalent circuit diagram and one set of measured and simulated curves are presented in figure 7.4 a. Using the relation

$$C = \epsilon_r \epsilon_0 \frac{A}{d} \tag{7.2}$$

gave ϵ_r.

---

[1] For the preparation of the first electrode the substrate was cooled to -10 ℃ while deposited at a rate of 0.2 Å/s. The diameter of the electrode was 7 mm.

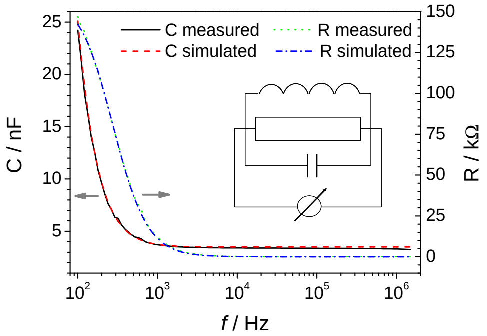

Figure 7.4: Impedance measurement with the resulting dielectric spectra obtained from a sample C6:C_{60} = 40:60 with a thickness of 421 nm. The inset shows the equivalent circuit diagram used for these fits.

In order to analyze the trap states an approach adapted from Burtone and coworkers has been used.[171] The impedance Z and the phase ϕ were measured from 20 to 10^5 Hz. For the trap analysis the determination of the complex capacitance is necessary. This quantity is derived from

$$C(\omega) = \frac{Y(\omega)}{j\omega} \tag{7.3}$$

where $Y(\omega)$ is the complex admittance, defined as the inverse of the impedance $Z(\omega)$. The detailed transformations for the isolation of the real and imaginary part of the capacitance are described in the appendix.

7.5 Optical Characterization

UV/vis spectroscopy

The reflection and transmission measurements were made using a Shimadzu SolidSpec 3700 UV/vis spectrophotometer, a double beam spectrometer, in which reference and sample beam are measured almost simultaneously. Absolute reflection and transmission measurements can be performed. The spectrometer allows several measurement setups for reflection and transmission measurements. Transmission can be obtained either directly or through an integrating sphere. Reflection measurements are conducted using the Absolute Specular Reflection (ASR) attachment. The ASR attachment allows reference and sample measurements by rearranging a mirror configuration without changing the light path. The reflection measurements are conducted at an angle of incidence of 5° using the integrating sphere. The spectrometer is equipped with three detectors in order to guarantee a high sensitivity in the whole range of interest: a photomultiplier tube (PMT) detector for the ultraviolet and visible range, and InGaAs and PbS detectors for the near-infrared region. The SolidSpec spectrometer is equipped with two light sources: a deuterium lamp for wavelengths below 320 nm and a halogen lamp for visible and infrared light. A monochromator filters the wavelength for the sample and reference beam which is directed at the sample. All measurements in this thesis were carried out in the wavelength range of λ = 200-1200 nm with a resolution of 1 nm for transmission and reflection measurements. The optical constants of the organic layer were extracted by means of iterative fitting in the software WVASE32 (J. A. Woollam Co., Inc.).

Ellipsometry

Ellipsometry is a method to determine the complex dielectric constant $\epsilon = \epsilon_1 + i\epsilon_2 = (n+ik)^2$ of a given material. ϵ, ϵ_1 and ϵ_2 are the dielectric constants, and n and k are the refractive index and extinction coefficient, respectively. They are all functions of the wavelength. The refractive index is used for optics in the Fresnel equations and Snell's law, while the dielectric constant is used in Maxwell's equations and electronics. The ellipsometer measures the change in polarization of light upon non-normal reflection on the surface of a sample. Hence, a highly reflecting surface is recommended in order to acquire a sufficient amount of the reflected light. The incident light is linearly polarized with finite field components E_p and E_s in the directions parallel and perpendicular to the plane of the incident light. Upon reflection, the s- and p-components experience a different attenuation and phase shift according to the Fresnel equations. The reflected light therefore is elliptically polarized. The ellipse of polarization of the reflected light is then measured with a second polarizer (analyzer). The complex dielectric constant can be obtained directly from the ellipticity of the reflected light by an inversion of the Fresnel equations. In this study, the ellipsometer (DUV-Vase, J. A. Wollam Co., Inc) was implemented in various methods to obtain optical constants of organic materials and electrodes. The optical constants of the organic layer were extracted by means of iterative fitting in the software WVASE32 (J. A. Woollam Co., Inc.).

Infrared Spectroscoy

Fourier transform infrared (FTIR) spectra were recorded with a FTIR spectrometer from Thermo Fisher Scientific (Continuµm). Thin films with a thickness of at least 300 nm have been prepared on a reflective aluminium layer deposited on silicon. IR transmission was recorded using a nitrogen cooled MCT detector and a Nicolet microscope in the ATR reflection mode. The spot size was set to 10 µm and the spectral resolution to 2 cm^{-1}. 100 scans were averaged for each spectrum.

Photoluminescence Spectroscopy

Luminescence measurements and wavelength dependent spectral response measurements were made with a FluoroMax-4 spectrofluorometer from Horiba Jobin Yvon. The continuous light source was a 150 W xenon arc-lamp and is split into single wavelengths by Czerny-Turner monochromators for excitation and emission. 8% of the excitation is split off for the reference beam detection by a UV enhanced silicon photodiode. Luminescence is collected and directed to the emission detector (R928P photomultiplier tube) which sends the signal to a photon counting module. The detector's response ranges from 180-850 nm, with dark counts below 1000 counts per second (cps). The linear range for photon counting is 1-2 million cps. Both the reference and signal detectors have correction-function files to correct wavelength dependencies of each optical component (250-850 nm). For SR-measurement, the excitation light source was used to illuminate the photodiodes with monochromatic light. During illumination, the reference signal intensity was detected and the short circuit output recorded with a Keithley power supply. Since the setup geometry changes with each new measurement, SR spectra with absolute values could not be obtained.

7.6 Thickness Control

Independently of optical properties, a profilometer can be used to determine the thickness of a deposited layer. Prior to deposition, a piece of Kapton tape was placed onto the substrate. When removed after preparation, the edge of the organic material could be measured with the Tencor Alpha Step 500 profilometer. During the measurement a diamond stylus is moved laterally across the sample while remaining in contact. The edge of the optical film causes a vertical displacement of the stylus. From the monitored height position of the stylus the film thickness can be derived. Therefore, from the height profile of the measurement, areas are chosen which can be assigned as substrate and layer height and the height difference determines the film thickness. For each sample three profilometer measurements were conducted and the mean value was taken as the result. Since organic materials are comparatively soft, the stylus may penetrate into the layer and thus cause incorrect results. The precision of the profilometer measurements was estimated by conducting multiple repetitive profilometer measurements and calculating the standard deviation. Error values between 2 nm and 5 nm were obtained.

For monitoring the layer thickness during deposition, quartz crystal microbalances from Inficon (gold, 6 MHz) have been used till reaching either a lifetime higher than 5% (starting from 0%) or an activity lower than 500 (starting from around 600). In order to calibrate the micobalances, reference layers were deposited and their thickness was determined either by profilometry, UV/vis spectrometry or ellipsometry.

7.7 Morphology Investigations

Atomic Force Microscopy

Atomic force microscopy (AFM) images were recorded with a Dimension 3100 Scanning Probe Microscope from Veeco Inc.. An area of 3 µm × 3 µm was measured with a resolution of 512 × 512 pixels. The surface roughness is characterized by two parameters, namely the root mean squared roughness (R_{RMS})[2] and the height difference between the highest and lowest measured value (peak to valley).

Differential Scanning Calometry

Differential scanning calorimetry (DSC) measurements were carried out with a Mettler Toledo DSC 1 tool, referenced against Zn (T_m = 419.5 °C) as well as In (T_m = 156.6 °C), using standard Al-crucibles (40 µl) and a nitrogen flow of 50 mL/min.

7.8 Simulations

Quantum Mechanical Calculations

Quantum mechanical calculations were performed with the computing software *HyperChem*. In oder to gain reliable molecule geometries, structures were pre-optimized in the force-field mode AMBER. For final geometry optimization, the PM3 (Parameterized Method 3; a reparameterization of AM1 = Austin Model 1) parameter set has been used.

Based on this structure single, point calculations were performed by applying the PM3 method[3] to yield the appropriate positions of the highest occupied molecular orbitals (HOMO) and the lowest unoccupied molecular orbitals (LUMO).

Optical Simulations for Optoelectronic Devices

In order to investigate the field distribution in optoelectronic devices, the simulation software Setfos 3.2 (Fluxim, Switzerland) was used assuming a coherence limit of 3000 nm. Optical constants were determined by transmission and reflection spectroscopy. The field amplitudes and the energy fluxes for each wavelength, at

---

[2] $R_{RMS} = \sqrt{\frac{1}{N}\sum_{i=0}^{N} x_i^2}$

[3] total charge = 0, spin multiplicity = 1 (singlet), convergence limit = 0.001 kcal/(Åmol), iteration limit = 150, no accelerated convergence, spin pairing RHF with the next lowest state.

each position within the stack were calculated by using a transfer matrix formalism implementing the optical constants of each layer as described in literature.[78] For optimization of the transport layer thicknesses, the absorptivity of the absorption layer was maximized for the AM1.5 solar spectrum.

Bibliography

[1] B. Piccard, B. Jones, *Mit dem Wind um die Welt - Die erste Erdumkreisung im Ballon*, Piper München, **2009**.

[2] Breitling Orbiter 3, http://www.orbiterballoon.com/Gallery/Gallery-image.aspx?fileid=18, last accessed on 30.09.2012.

[3] Solar Impulse, http://solarimpulse.com/en/multimedia/pictures/, last accessed on 30.09.2012.

[4] B. Kippelen, J.-L. Brédas, *Energy Environ. Sci.* **2009**, *2*, 251–261.

[5] Konarka module specification, http://www.konarka.com/media/pdf/konarka_40series.pdf, last accessed on 08.05.2012.

[6] N. Espinosa, M. Hösel, D. Angmo, F. C. Krebs, *Energy Environ. Sci.* **2012**, *5*, 5117–5132.

[7] G. Dennler, K. Forberich, M. C. Scharber, C. J. Brabec, I. Tomiš, *J. Appl. Phys.* **2007**, *102*, 054516 pp.

[8] D. Chirvase, Z. Chiuvare, M. Knipper, J. Parisi, V. Dyakonov, J. C. Hummelen, *J. Appl. Phys.* **2003**, *93*, 3376–3383.

[9] E. A. Katz, D. Faiman, S. M. Tuladhar, J. M. Kroon, M. Wienk, T. Fromherz, F. Padinger, C. J. Brabec, N. S. Sariciftci, *J. Appl. Phys.* **2001**, *90*, 5343–5350.

[10] B. P. Rand, J. Genoe, P. Heremans, J. Poortmans, *Prog. Photovolt: Res. Appl.* **2007**, *15*, 659–676.

[11] M. Riede, T. Mueller, R. Schueppel, K. Leo, *Nanotechnology* **2008**, *19*, 424001 pp.

[12] A. H. Lipkus, Q. Yuan, K. A. Lucas, S. A. Funk, W. F. Bartelt, R. J. Schenck, A. J. Trippe, *J. Org. Chem.* **2008**, *73*, 4443–4451.

[13] C. Deibel, V. Dyakonov, *Rep. Prog. Phys.* **2010**, *73*, 096401 pp.

[14] S. Braun, W. R. Salaneck, M. Fahlman, *Adv. Mater.* **2009**, *21*, 1450–1472.

[15] W. Tress, K. Leo, M. Riede, *Adv. Funct. Mater.* **2011**, *21*, 2140–2149.

[16] C. Uhrich, D. Wynands, S. Olthof, M. K. Riede, K. Leo, S. Sonntag, B. Maennig, M. Pfeiffer, *J. Appl. Phys.* **2008**, *104*, 043107 pp.

[17] K. Walzer, B. Maennig, M. Pfeiffer, K. Leo, *Chem. Rev.* **2007**, *107*, 1233–1271.

[18] F. Ante, D. Kälblein, U. Zschieschang, T. W. Canzler, A. Werner, K. Takimiya, M. Ikeda, T. Sekitani, T. Someya, H. Klauk, *Small* **2011**, *7*, 1186–1191.

[19] B. P. Rand, D. P. Purk, S. R. Forrest, *Phys. Rev. B* **2007**, *75*, 115327 pp.

[20] F. T. Reis, D. Mencaraglia, S. O. Saad, I. Séguy, M. Oukachmih, P. Jolinat, P. Destruel, *Synth. Met.* **2003**, *138*, 33–37.

[21] W. Zeng, K. S. Yong, Z. M. Kam, F. Zhu, Y. Li, *Appl. Phys. Lett.* **2010**, *97*, 133304 pp.

[22] Y. Ohmori, E. Itoh, K. Miyairi, *Thin Solid Films* **2006**, *499*, 369–373.

[23] T. Kietzke, *Advances in OptoElectronics, doi:10.1155/2007/40285* **2007**.

[24] N. Li, B. E. Lassiter, R. R. Lunt, G. Wei, S. R. Forrest, *Appl. Phys. Lett.* **2009**, *94*, 023307 pp.

[25] J. C. Bernéde, L. Cattin, S. O. Djobo, M. Morsli, S. R. B. Kanth, S. Patil, P. Leriche, J. Roncali, A. Godoy, F. R. Diaz, M. A. del Valle, *Phys. Status Solidi A* **2011**, *208*, 1989–1994.

[26] L. Shen, G. Zhu, W. Guo, C. Tao, X. Zhang, C. Liu, W. Chen, S. Ruan, Z. Zhong, *Appl. Phys. Lett.* **2008**, *92*, 073307 pp.

[27] R. Schueppel, K. Schmidt, C. Uhrich, K. Schulze, D. Wynands, J. L. Brédas, E. Brier, E. Reinold, H.-B. Bu, P. Baeuerle, B. Maennig, M. Pfeiffer, K. Leo, *Phys. Rev. B* **2008**, *77*, 085311 pp.

[28] T. D. Heidel, D. Hochbaum, J. M. Sussman, V. Singh, M. E. Bahlke, *J. Appl. Phys.* **2011**, *109*, 104502 pp.

[29] K. Triyana, T. Yasuda, K. Fujita, T. Tsutsui, *Jpn. J. Appl. Phys.* **2004**, *43*, 2353–2358.

[30] J. C. Ho, A. Arango, V. Bulovic, *Appl. Phys. Lett.* **2008**, *93*, 063305 pp.

[31] S. Wang, E. I. Mayo, M. D. Perez, L. Griffe, G. Wei, P. I. Djurovich, S. R. Forrest, M. E. Thompson, *Appl. Phys. Lett.* **2009**, *94*, 233304 pp.

[32] S. Pfuetzner, J. Meiss, A. Petrich, M. Riede, K. Leo, *Appl. Phys. Lett.* **2009**, *94*, 223307 pp.

[33] W. Zhao, A. Kahn, *J. Appl. Phys.* **2009**, *105*, 123711 pp.

[34] J. Huang, J. Blochwitz-Nimoth, M. Pfeiffer, K. Leo, *J. Appl. Phys.* **2003**, *93*, 838–844.

[35] S. Wang, Z. Bian, X. Xia, C. Huang, *Org. Electron.* **2010**, *11*, 1909–1915.

[36] Y.-S. Yao, J. Xiao, X.-S. Wang, Z.-B. Deng, B.-W. Zhang, *Adv. Funct. Mater.* **2006**, *16*, 709–718.

[37] Y. Kim, S. A. Choulis, J. Nelson, D. C. Bradley, S. Cook, J. R. Durrant, *Appl. Phys. Lett.* **2005**, *86*, 063502 pp.

[38] M. C. Scharber, D. Mühlbacher, M. Koppe, P. Denk, C. Waldauf, A. J. Heeger, C. J. Brabec, *Adv. Mater.* **2006**, *18*, 789–794.

[39] Y. Li, Y. Cao, J. Gao, D. Wang, G. Yu, A. J. Heeger, *Synth. Met.* **1999**, *99*, 243–248.

[40] J. Drechsel, M. Pfeiffer, X. Zhou, A. Nollau, K. Leo, *Synth. Met.* **2002**, *127*, 201–205.

[41] S. Senthilarasu, Y. B. Hahn, S.-H. Lee, *J. Appl. Phys.* **2007**, *102*, 043512 pp.

[42] S. Senthilarasu, Y. B. Hahn, S.-H. Lee, *J. Mater. Sci.: Mater. Electron.* **2008**, *19*, 482–486.

[43] H. Brinkmann, C. Kelting, S. Makarov, O. Tsaryova, G. Schnurpfeil, D. Woehrle, D. Schlettwein, *Phys. Stat. Sol. (a)* **2008**, *205*, 409–420.

[44] H. W. Kroto, J. R. Heath, S. C. O'Brien, R. F. Curl, R. E. Smalley, *Nature* **1985**, *318*, 162–163.

[45] H. W. Kroto, *Angew. Chem. Int. Ed.* **1992**, *91*, 111–129.

[46] M. Pope, C. E. Swenberg, *Electronic Processes in Organic Crystals and Polymers*, Oxford University Press, New York, **1999**.

[47] B. Kessler, *Appl. Phys. A* **1998**, *67*, 125–133.

[48] P. G. Nicholson, F. A. Castro, *Nanotechnology* **2010**, *21*, 492001 pp.

[49] NREL, Reference Solar Spectral Irradiance: Air Mass 1.5, URL: http://rredc.nrel.gov/solar/spectra/am1.5, last accessed on 03.08.2010.

[50] T. Ameri, G. Dennler, C. Lungenschmied, C. J. Brabec, *Energy Environ. Sci.* **2009**, *2*, 347–363.

[51] M. Riede, C. Uhrich, J. Widmer, R. Timmreck, D. Wynands, G. Schwartz, W.-M. Gnehr, D. Hildebrandt, A. Weiss, J. Hwang, S. Sundarraj, P. Erk, M. Pfeiffer, K. Leo, *Adv. Funct. Mater.* **2011**, *21*, 3019–3028.

[52] J.-L. Brédas, J. E. Norton, J. Cornil, V. Coropceanu, *Acc. Chem. Res.* **2009**, *11*, 1691–1699.

[53] dielectric constant of Si, http://en.wikipedia.org/wiki/Relative_permittivity, last accessed on 30.05.2012.

[54] D. Natali, M. Sampietro, *Nuc. Instrum. Methods* **2003**, *512*, 419–426.

[55] J. Nelson, *Curr. Opin. Solid State Mater.* **2002**, *6*, 87–95.

[56] Y. Shao, Y. Yang, *Adv. Mater.* **2005**, *17*, 2841–2844.

[57] P. Peumans, A. Yakimov, S. R. Forrest, *J. Appl. Phys.* **2003**, *93*, 3693–3723.

[58] P. Sullivan, S. Heutz, S. M. Schultes, T. S. Jones, *Appl. Phys. Lett.* **2004**, *84*, 1210–1212.

[59] K. Schulze, C. Uhrich, R. Schüppel, K. Leo, M. Pfeiffer, E. Brier, E. Reinold, P. Bäuerle, *Adv. Mater.* **2006**, *18*, 2872–2875.

[60] T.-Y. Chu, O.-K. Song, *Appl. Phys. Lett.* **2007**, *90*, 203512 pp.

[61] Z. B. Wang, M. G. Helander, M. T. Greiner, J. Qiu, Z. H. Lu, *J. Appl. Phys.* **2010**, *107*, 034506 pp.

[62] P. W. M. Blom, M. J. M. de Jong, M. G. van Munster, *Phys. Rev. B* **1997**, *55*, R656–R659.

[63] B. R. Rand, J. Xue, S. Uchida, S. R. Forrest, *J. Appl. Phys.* **2005**, *98*, 124902 pp.

[64] P. N. Murgatroyd, *J. Phys. D: Appl. Phys.* **1970**, *3*, 151–156.

[65] N. Karl, Čápek, I. Muzikante, R. W. Munn, P. Petelez, *Organic Electronic Materials*, (editors: R. Farchioni, G. Grosso), Springer, Berlin, **2001**.

[66] M. Pfeiffer, K. Leo, X. Zhou, J. S. Huang, M. Hofmann, A. Werner, J. Blochwitz-Nimoth, *Org. Electron.* **2003**, *4*, 89–103.

[67] W. Brütting, *Physics of Organic Semiconductors*, (editor: W. Brütting), WILEY-VCH, **2005**.

[68] W. Tress, S. Pfützner, M. Riede, K. Leo, *J. Photonics Energy Environ. Sci.* **2011**, *1*, 011114 pp.

[69] D. Gupta, S. Mukhopadhyay, K. S. Narayan, *Sol. Energy Mater. Sol. Cells* **2010**, *94*, 1309–1313.

[70] C. J. Brabec, A. Cravino, D. Meissner, N. S. Sariciftci, T. Fromherz, M. T. Rispens, L. Sanchez, J. C. Hummelen, *Adv. Funct. Mater.* **2001**, *11*, 374–380.

[71] I. Bruder, A. Ojala, C. Lennartz, S. Sundarraj, J. Schoeneboom, S. R., J. Hwang, P. Erk, J. Weis, *Sol. Energy Mater. Sol. Cells* **2010**, *94*, 310–316.

[72] A. K. Thakur, G. Wantz, G. Garcia-Belmonte, J. Bisquert, L. Hirsch, *Sol. Energy Mater. Sol. Cells* **2011**, *95*, 2131–2135.

[73] J. Sakai, T. Taima, K. Saito, *Org. Electron.* **2008**, *9*, 582–590.

[74] W. Tress, K. Leo, M. Riede, *Phys. Rev. B* **2012**, *85*, 155201 pp.

[75] T. Kirchartz, U. Rau, *Phys. Stat. Sol. (a)* **2008**, *205*, 2737–2751.

[76] I. Riedel, J. Parisi, V. Dyakonov, L. Lutsen, D. Vanderzande, J. C. Hummelen, *Adv. Funct. Mater.* **2004**, *14*, 38–44.

[77] R. Häusermann, E. Knapp, M. Moos, N. A. Reinke, T. Flatz, B. Ruhstaller, *J. Appl. Phys.* **2009**, *106*, 104507 pp.

[78] F. AG, *Setfos 3.2 User Manual*, **2011**.

[79] R. Koeppe, O. Bossart, G. Galzaferri, N. S. Sariciftci, *Sol. Energy Mater. Sol. Cells* **2007**, *91*, 986–995.

[80] J. I. Basham, G. K. Mor, C. A. Grimes, *ACS Nano* **2010**, *4*, 1253–1258.

[81] H. Wiesenhofer, D. Beljonne, G. D. Scholes, E. Hennebicq, J.-L. Brédas, E. Zojer, *Adv. Funct. Mater.* **2005**, *15*, 155–160.

[82] C. W. Tang, *Appl. Phys. Lett.* **1985**, *48*, 183–185.

[83] M. Hiramoto, H. Fujiwara, M. Yokoyama, *Appl. Phys. Lett.* **1991**, *58*, 1062–1064.

[84] B. Maennig, J. Drechsel, D. Gebeyehu, P. Simon, F. Kozlowski, A. Werner, F. Li, S. Grundmann, S. Sonntag, M. Koch, K. Leo, M. Pfeiffer, H. Hoppe, D. Meissner, N. S. Sariciftci, I. Riedel, J. Parisi, *Appl. Phys. A* **2004**, *79*, 1–14.

[85] Heliatek, Tandem solar cell by Heliatek with an efficiency of 12.0% on an area of 1.1 cm^2, press release, **2013**, http://www.heliatek.com/wp-content/uploads/2013/01/130116_PM_Heliatek-erzielt-Weltrekordeffizienz-fuer-OPV.pdf, last accessed on 22.04.13.

[86] A. Kumar, G. Li, Z. Hong, Y. Yang, *Nanotechnology* **2009**, *20*, 165202 pp.

[87] S. Pfuetzner, J. Meiss, A. Petrich, M. Riede, K. Leo, *Appl. Phys. Lett.* **2009**, *94*, 253303 pp.

[88] S. Heutz, P. Sullivan, B. M. Sanderson, S. M. Schultes, T. S. Jones, *Sol. Energy Mater. Sol. Cells* **2004**, *83*, 229–245.

[89] P. Peumans, V. Bulović, S. R. Forrest, *Appl. Phys. Lett.* **2000**, *76*, 2650–2652.

[90] J. Drechsel, B. Maennig, F. Kozlowski, M. Pfeiffer, K. Leo, *Appl. Phys. Lett.* **2005**, *86*, 244102 pp.

[91] A. Mishra, P. Bäuerle, *Angew. Chem.* **2012**, *124*, 2060–2109.

[92] D. H. Wang, H. K. Lee, D.-G. Choi, J. H. Park, O. Park, *Appl. Phys. Lett.* **2009**, *95*, 043505 pp.

[93] M. Kaur, A. Gopal, R. M. Davis, J. R. Heflin, *Sol. Energy Mater. Sol. Cells* **2009**, *83*, 1779–1784.

[94] K. Yoshino, K. Tada, A. Fujii, E. M. Conwell, A. A. Zakhidov, *IEEE Trans. Electron Dev.* **1997**, *44*, 1315–1324.

[95] L. Chen, Y. Tang, X. Fan, C. Zhang, Z. Chu, D. Wang, D. Zou, *Org. Electron.* **2009**, *10*, 724–728.

[96] W. Tress, K. Leo, M. Riede, *Sol. Energy Mater. Sol. Cells* **2011**, *95*, 2981.

[97] S. H. Park, J. G. Jeong, H.-J. Kim, S.-H. Park, M.-H. Cho, S. W. Cho, Y. Yi, M. Y. Heo, H. Sohn, *Appl. Phys. Lett.* **2010**, *96*, 013302 pp.

[98] C. Hein, E. Mankel, T. Mayer, W. Jaegermann, *Sol. Energy Mater. Sol. Cells* **2010**, *94*, 662–667.

[99] H. Y. Mao, F. Bussolotti, D.-C. Qi, R. Wang, S. Kera, N. Ueno, A. T. S. Wee, W. Chen, *Org. Electron.* **2011**, *12*, 534–540.

[100] M. M. El-Nahass, H. M. Zezada, M. S. Aziz, N. A. El-Ghamaz, *Opt. Mater.* **2004**, *27*, 491–498.

[101] M. Wojdyla, B. Derkowska, Y. Lukasiak, W. Bala, *Mat. Lett.* **2006**, *60*, 3441–3446.

[102] D. Ray, M. Furno, E. Siebert-Henze, K. Leo, M. Riede, *Phys. Rev. B* **2011**, *84*, 075214 pp.

[103] R. Seoudi, G. S. El-Bahy, Z. A. El Sayed, *Opt. Mater.* **2006**, *29*, 304–312.

[104] C. C. Leznoff, A. B. P. Lever, *Phthalocyanines: Properties and Applications*, (editors: C. C. Leznoff, A. B. P. Lever), VHC Publishers, Inc., **1996**.

[105] S. Kment, P. Kluson, M. Drobek, R. Kuzel, I. Gregora, M. Kohout, Z. Hubicka, *Thin Solid Films* **2009**, *517*, 5274–5279.

[106] S. Senthilarasu, R. Sathyamoorthy, S. Lalitha, A. Subbarayan, K. Natarajan, *Sol. Energy Mater. Sol. Cells* **2004**, *82*, 179–186.

[107] C. Keil, O. Tsaryova, L. Lapok, C. Himcinschi, D. Wöhrle, O. R. Hild, D. R. T. Zahn, S. M. Gorun, D. Schlettwein, *Thin Solid Films* **2009**, *517*, 4379–4384.

[108] A. A. Zanfolim, D. Volpati, C. A. Olivati, A. E. Job, C. J. L. Constantino, *J. Phys. Chem. C* **2010**, *114*, 12290–12299.

[109] A. Haug, S. Harbeck, D. Dini, M. Hanack, M. J. Cook, H. Peisert, Chassé, *Appl. Surf. Sci.* **2005**, *252*, 139–142.

[110] L. Gaffo, M. R. Cordeira, A. R. Freitas, W. C. Moreira, E. M. Girotto, V. Zucolotto, *J. Mater. Sci.* **2010**, *45*, 1366–1370.

[111] F. Padinger, R. S. Rittberger, N. S. Sariciftci, *Adv. Funct. Mater.* **2003**, *13*, 85–88.

[112] W. Ma, C. Yang, X. Gong, K. Lee, A. J. Heeger, *Adv. Funct. Mater.* **2005**, *15*, 1617–1622.

[113] B. Yu, L. Huang, H. Wang, D. Yan, *Adv. Mater.* **2010**, *22*, 1017–1020.

[114] G. Y. Park, Y. Ha, *Synth. Met.* **2008**, *158*, 120–124.

[115] T. J. K. Brenner, Z. Li, C. R. McNeill, *J. Phys. Chem. C* **2011**, *115*, 22075–22083.

[116] A. K. Satpati, M. Kumbhakar, D. K. Maity, H. Pal, *Chem. Phys. Lett.* **2005**, *407*, 114–118.

[117] V. Sholin, J. D. Olson, S. A. Carter, *J. Appl. Phys.* **2007**, *101*, 123114 pp.

[118] G. A. Reynolds, K. H. Drexhage, *Opt. Commun.* **1975**, *13*, 222–225.

[119] M. S. A. Abdel-Mottaleb, M. S. Antonius, M. M. Abo-Ali, L. F. M. Ismail, B. A. El-Sayed, A. M. K. Sherief, *Proc. Indian Acad. Sci. (Chem. Sci.)* **1992**, *104*, 185–196.

[120] G. Y. Zhong, Z. Xu, S. T. Zhang, Y. Q. Zhan, X. J. Wang, Z. H. Xiong, H. Z. Shi, X. M. Ding, *Appl. Phys. Lett.* **2002**, *81*, 1122–1124.

[121] M. Lesiecki, F. Asmar, *J. Lumin.* **1984**, *31*, 546–548.

[122] M. J. Currie, J. K. Mapel, T. D. Heidel, S. Goffri, M. A. Baldo, *Science* **2008**, *321*, 226–228.

[123] H. Suzuki, H. Meyer, S. Hoshino, D. Haarer, *J. Appl. Phys.* **1995**, *78*, 2684–2690.

[124] Y. Terao, H. Sasabe, C. Adachi, *Appl. Phys. Lett.* **2007**, *90*, 103515 pp.

[125] C. H. Chen, J. Shi, C. W. Tang, *Macromol. Symp.* **1998**, *125*, 1–48.

[126] C. W. Tang, S. A. van Slyke, C. H. Chen, *J. Appl. Phys.* **1989**, *65*, 3610–3616.

[127] J. Li, Z. Hong, S. Tong, P. Wang, C. Ma, O. Lengyel, C.-S. Lee, H.-L. Kwong, S. Lee, *Chem. Mater.* **2003**, *15*, 1486–1490.

[128] F. Pschenitzka, J. C. Sturm, *Appl. Phys. Lett.* **2001**, *79*, 4354–4356.

[129] Z.-S. Wang, Y. Cui, K. Hara, Y. Dan-oh, C. Kasada, A. Shinpo, *Adv. Mater.* **2007**, *19*, 1138–1141.

[130] K. D. Seo, H. M. Song, M. J. Lee, M. Pastore, C. Anselmi, F. De Angelis, K. Nazeeruddin, M. Grätzel, H. K. Kim, *Dyes Pigments* **2011**, *90*, 304–310.

[131] A. Ltaief, R. B. Chaâbane, A. Bouazizi, J. Davenas, *Mater. Sci. Eng., C* **2006**, *26*, 344–347.

[132] Y. A. M. Ismail, T. Soga, T. Jimbo, *Jpn. J. Appl. Phys.* **2010**, *49*, 052301 pp.

[133] Y. A. M. Ismail, T. Soga, T. Jimbo, *J. Appl Phys.* **2011**, *109*, 103109 pp.

[134] S. Iijima, F. Mizutani, Y. Tanaka, *Bull. Chem. Soc. Jpn.* **1985**, *58*, 1585–1586.

[135] R. M. Meixner, H. Göbel, F. A. Yildirim, W. Bauhofer, W. Krautschneider, *Appl. Phys. Lett.* **2006**, *89*, 092110 pp.

[136] M. Adachi, S. Nakamura, *J. Phys. Chem.* **1994**, *98*, 1796–1801.

[137] P. E. Shaw, A. Ruseckas, J. Peet, C. Bazan, I. D. W. Samuel, *Adv. Funct. Mater.* **2010**, *20*, 155–161.

[138] W. A. Luhmann, R. J. Holmes, *Adv. Funct. Mater.* **2011**, *21*, 764–771.

[139] C. Deibel, T. Strobel, V. Dyakonov, *Adv. Mater.* **2010**, *22*, 4097–4111.

[140] D. Veldman, O. Ipek, S. C. J. Meskers, J. Sweelssen, M. M. Koetse, S. C. Veenstra, J. M. Kroon, S. S. van Bavel, J. Loos, R. A. J. Janssen, *J. Am. Chem. Soc.* **2008**, *130*, 7721–7735.

[141] G. Jones, S. F. Griffin, C. Choi, W. R. Bergmark, *J. Org. Chem.* **1984**, *49*, 2705–2708.

[142] I. Noviandri, R. D. Bolskar, P. A. Lay, C. A. Reed, *J. Phys. Chem. B* **1997**, *101*, 6350–6358.

[143] A. Shalav, B. S. Richards, M. A. Green, *Sol. Energy Mater. Sol. Cells* **2007**, *91*, 829–842.

[144] B. Beyer, D. Griese, C. Schirrmann, R. Pfeifer, S. Kahmann, O. R. Hild, K. Leo, *Thin Solid Films* **2013**, *536*, 206–210.

[145] A. S. Riad, S. M. Khalil, S. Darwish, *Thin Solid Films* **1994**, *249*, 219–223.

[146] V. Bulovic, A. Shoustikov, M. A. Baldo, E. Bose, V. G. Kozlov, M. E. Thompson, S. R. Forrest, *Chem. Phys. Lett.* **1998**, *287*, 455–460.

[147] J. Meiss, M. Furno, S. Pfuetzner, K. Leo, M. Riede, *J. Appl. Phys.* **2010**, *107*, 053117 pp.

[148] S. R. Forrest, P. E. Burrows, Z. D. Garbuzov, V. Bulović, Organische Lumineszenzbeschichtung für Lichtdetektoren, DE 697 29 754 T2, **2004**.

[149] M. Hermenau, M. Riede, K. Leo, *Stability and Degradation of Organic and Polymer Solar Cells*, (editor: F. C. Krebs), WILEY-VCH, **2012**.

[150] J. D. Kotlarski, P. W. M. Blom, *Appl. Phys. Lett.* **2011**, *98*, 053301 pp.

[151] W. J. Belcher, K. I. Wagner, P. C. Dastoor, *Sol. Energy Mater. Sol. Cells* **2007**, *91*, 447–452.

[152] P. C. Dastoor, C. R. McNeill, H. Frohne, C. J. Foster, B. Dean, C. J. Fell, W. J. Belcher, W. M. Campbell, D. L. Officer, I. M. Blake, P. Thordarson, M. J. Crossley, N. S. Hush, J. R. Reimers, *J. Phys. Chem. C* **2007**, *111*, 15415–15426.

[153] S. Honda, T. Nogami, H. Ohkita, H. Benten, S. Ito, *ACS Appl. Mater. Interfaces* **2009**, *1*, 804–810.

[154] J. Cabanillas-Gonzalez, S. Yeates, D. D. C. Bradley, *Synth. Met.* **2003**, *139*, 637–641.

[155] P. Suresh, P. Balraju, G. D. Sharma, J. A. Mikroyannidis, M. M. Stylianakis, *ACS Appl. Mater. Interfaces* **2009**, *1*, 1370–1374.

[156] G. Adam, A. Pivrikas, A. M. Ramil, S. Tadesse, T. Yohannes, N. S. Sariciftci, D. A. M. Egbe, *J. Mater. Chem.* **2011**, *21*, 2594–2600.

[157] M. Koppe, H.-J. Egelhaaf, G. Dennler, M. C. Scharber, C. J. Brabec, P. Schilinsky, C. N. Hoth, *Adv. Funct. Mater.* **2010**, *20*, 338–346.

[158] C.-H. Chen, C.-H. Hsieh, M. Dubosc, Y.-J. Cheng, C.-S. Hsu, *Macromolecules* **2010**, *43*, 697–708.

[159] M. C. Chen, D. J. Liaw, Y. C. Huang, Y. Tai, *Sol. Energy Mater. Sol. Cells* **2011**, *95*, 2621–2627.

[160] J.-H. Huang, M. Velusamy, K.-C. Ho, J.-T. Lin, C.-W. Chu, *J. Mater. Chem.* **2010**, *20*, 2820–2825.

[161] D. Qin, W. Quan, J. Liu, G. Li, L. Chen, J. Zhang, D. Yan, *Phys. Status Solidi A* **2012**, *209*, 1150–1156.

[162] M. Campoy-Quiles, Y. Kanai, a. El-Basaty, H. Sakai, H. Murata, *Org. Electron.* **2009**, *10*, 1120–1132.

[163] K. B. Burke, W. J. Belcher, L. Thomson, B. Watts, C. R. McNeill, H. Ade, P. C. Dastoor, *Macromolecules* **2009**, *42*, 3098–3103.

[164] J. Peet, A. B. Tamayo, X.-D. Dang, J. H. Seo, T.-Q. Nguyen, *Appl. Phys. Lett.* **2008**, *93*, 163306 pp.

[165] Z. Tian-Hui, Z. Su-Ling, P. Ling-Yu, X. Zheng, J. Si-Ting, L. Xiao-Dong, K. Chao, X. Xu-Rong, *Chin. Phys. B* **2011**, *20*, 038401 pp.

[166] P. P. Khlyabich, B. Burkhart, B. C. Thompson, *J. Am. Chem. Soc.* **2011**, *133*, 14534–14537.

[167] H. Kim, M. Shin, Y. Kim, *J. Phys. Chem. C* **2009**, *113*, 1620–1623.

[168] S.-B. Rim, R. F. Fink, J. C. Schöneboom, P. Erk, P. Peumans, *Appl. Phys. Lett.* **2007**, *91*, 173504 pp.

[169] K. Triyana, T. Yasuda, K. Fujita, T. Tsutsui, *Thin Solid Films* **2005**, *477*, 198–202.

[170] J. Meiss, A. Merten, M. Hein, C. Schuenemann, S. Schäfer, M. Tietze, C. Uhrich, M. Pfeiffer, K. Leo, M. Riede, *Adv. Funct. Mater.* **2012**, *22*, 405–414.

[171] L. Burtone, D. Ray, K. Leo, M. Riede, *J. Appl. Phys.* **2012**, *111*, 064503 pp.

[172] H. Li, Z.-G. Zhang, Y. F. Li, J. Wang, *Appl. Phys. Lett.* **2012**, *101*, 163302 pp.

[173] P. Würfel, *Physics of Solar Cells: From Basic Principles to Advanced Concepts*, Wiley-VCH, Weinheim, **2009**.

[174] A. de la Holz, A. Díaz-Ortiz, A. Moreno, *Chem. Soc. Rev.* **2005**, *34*, 164–178.

[175] C. Gabriel, S. Gabriel, E. H. Grant, B. S. J. Halstead, D. M. P. Mingos, *Chem. Soc. Rev.* **1998**, *27*, 213–223.

[176] C. O. Kappe, A. Stadler, *Mircowaves in Organic and Medicinal Chemistry*, WILEY-VHC, **2005**.

[177] J. P. Tierney, Lidström, *Microwave Assisted Organic Synthesis*, Blackwell Publishing Ltd Oxford, **2005**.

[178] D. Stuerga, P. Gaillard, *J. Microwave Power Electromagn. Energy* **1996**, *31*, 101–131.

[179] M. A. Herrero, J. M. Kremsner, C. O. Kappe, *J. Org. Chem.* **2008**, *73*, 36–47.

Appendix A

Fluorescent Emitters and their Application in OSCs

A.1 Optical Properties

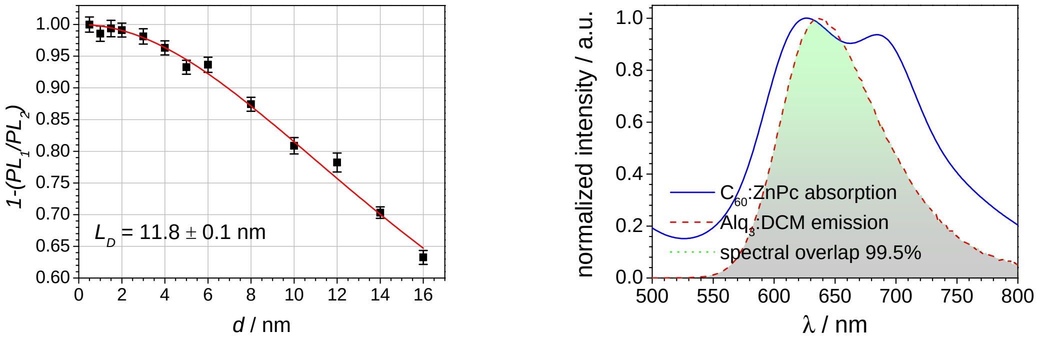

(a) (b)

Figure A.1: (a) Fitting result for L_D in C6 obtained by using equation 4.1. (b) Overlap of the emission spectrum originating from Alq$_3$:DCM and the absorption spectrum of C$_{60}$:ZnPc blends.

Appendix B

Gradient C_{60}:ZnPc Absorption Layers in Small Molecule Solar Cells

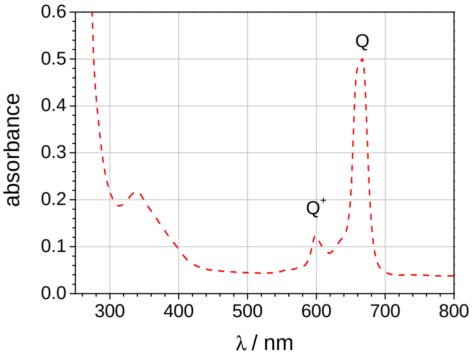

(a)

Figure B.1: Absorbance spectrum of ZnPc dissolved in THF at a concentration of 10^{-6} molL^{-1}.

Appendix C

Organic Solar Cells with Ternary Absorption Layers

C.1 C_{60}:ZnPc:C_6

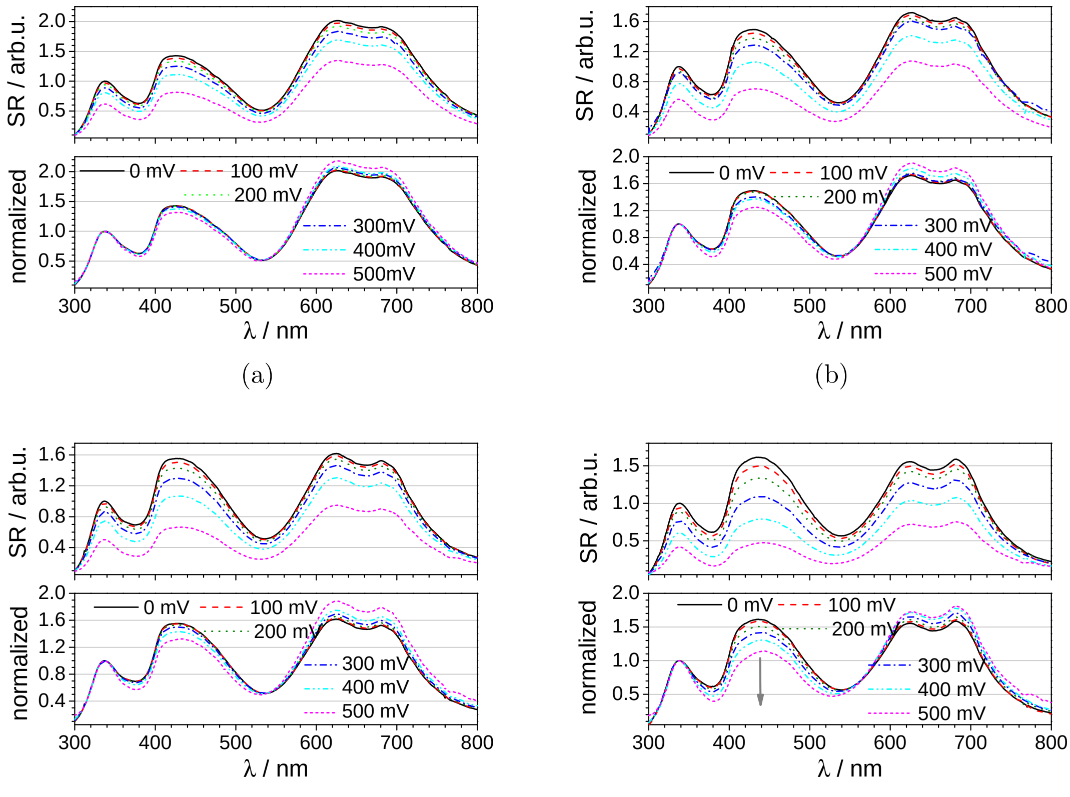

(a)

(b)

(c)

(d)

Figure C.1: Voltage dependent SR spectra for different C_{60}:ZnPc:C6 combinations starting with 0% C6 (a), 5% C6 (b), 10% C6 (c) to 15% C6 (d).

Table C.1: Relative absorptivity of ternary C_{60}:ZnPc:C6 absorption layers and the short circuit density of the corresponding solar cells for several layer compositions.

C_{60}:ZnPc:C6	J_{SC} / mAcm^{-1}	A × 10^{21} m^{-2}s^{-1}	$J_{SC}/J_{SC_{binary}}$	A/A_{binary}
65:35:00	8.72	4.13	1.00	1.00
65:30:05	7.45	3.93	0.85	0.95
65:25:10	7.27	3.77	0.83	0.91
65:20:15	6.65	3.66	0.77	0.87

Appendix D

Materials and Instrumentation

D.1 Microwave assisted synthesis of Metal Phthalocyanines

Heating under microwave irradiation is an attractive chemical application and has become a widely accepted, non-conventional energy source for performing organic synthesis, especially since it has been discovered that the time scale of several reactions can be reduced dramatically compared to conventional conditions. Microwave heating uses the ability of molecules to transform electromagnetic energy into heat. The energy transmission occurs by dielectric losses, in contrast to the conduction and convection processes observed in conventional heating. Microwave irradiation is rapid and volumetric; the whole volume of the solution is heated simultaneously. The magnitude of the microwave absorption, and so the heating rate, depends on the dielectric properties of the molecules, so heating is selectively.[174] A dielectric material contains either permanent or induced dipoles so, when placed between two electrodes, acts as a capacitor. The polarization of dielectrics arises either from the finite displacement of charges or the rotation of dipoles in an electric field. Microwave electric heating is a result of polarization processes at the molecular level. The higher the permanent dipole moment, the more these dipoles able to reorientate in an applied electrical field. If this field is switched off, the molecules go back to their thermodynamically most stable state, the randomised state. However, they do not immediately adopt this random orientation - the time for this is the relaxation time τ. It is controlled by the radius r of a spherical molecule rotating in a viscous continuum and the viscosity η of the medium. The relaxation time is strongly related to the intermolecular forces. Moreover, it is also temperature-dependent (*vide* equation D.1).[175]

$$\tau = \frac{4\pi r^3 \eta}{kT} \tag{D.1}$$

The ability of a specific substance to convert electromagnetic energy into heat at a given frequency and temperature is determined by the so-called loss tangent, tanδ.

$$tan\delta = \frac{\epsilon''}{\epsilon'} \tag{D.2}$$

This loss factor is expressed as a quotient (equation D.2), where ϵ'' is the dielectric loss, indicative of the efficiency with which electromagnetic radiation is converted and ϵ' is the dielectric constant describing the polarizability of the molecules in the electric field. A reaction medium with a high tanδ is required for efficient absorption and consequently for rapid heating.[176] The loss tangent values are both frequency- and temperature-dependent, as can be seen in equation D.3 and D.4 by means of the relation between the relaxation and ϵ', ϵ'' respectively. ϵ_S is here the permittivity in a static field, so $\epsilon_S \ll \frac{1}{\tau}$. ϵ_∞ is the permittivity at very high frequencies, $\gg \frac{1}{\tau}$ and ω is the angular frequency ($\omega = 2\pi\nu$).[177]

$$\epsilon' = \epsilon_\infty + \frac{\epsilon_S - \epsilon_\infty}{1 + \omega^2\tau^2} \tag{D.3}$$

$$\epsilon'' = \frac{(\epsilon_S - \epsilon_\infty\omega\tau)}{1 + \omega^2\tau^2} \tag{D.4}$$

The effect of microwave irradiation in chemical reactions is a combination of thermal and non-thermal effects.[178] The thermal effects, also called 'specific microwave effects', include the selective heating of specific reaction compounds, rapid heating rates, temperature gradients, the elimination of wall effects and the superheating of solvents at atmospheric pressure.[179] The non-thermal effects comprise unusual observations which cannot be explained so easily. These effects are thought not to require the transfer of microwave energy into thermal energy. Instead, the microwave energy itself directly couples to energy modes within the molecule or lattice.

Since microwave assisted synthesis offers an attractive approach to rapidly achieve compounds in high yield, this method was applied to the synthesis of metal phthalocyanines. 2.0-2.5 g of the phthalic acid nitrile derivative (slight excess to suppress the formation of subphthalocyanines, 4.2 equivalent) and a metal source (1.0 equivalent) were mixed in a crystallizing dish. *N,N'*-Dimethylformamide (DMF, 0.5 to 1.0 mL) was added until the mixture was a paste. Afterwards, some droplets of water were used to thicken slightly the dough. The dish was covered by a second crystallizing dish, put again in a bigger one and finally everything was covered with a Petri dish. Depending on the reaction behavior, the reactor was irradiated for 2-5 min with microwaves at different power levels. The reaction was finished after a colorful biscuit-like solid was obtained. This solid was then pulverized. This process was repeated several times and the batches were unified for further purification with different solvents by Soxhlet extraction equipment and sublimation.

Table D.1: Overview of the synthesis conditions with the irradiation power (P_{irr}) the irradiation time (t_{irr}), the yields after extraction (y_{ini}) and after sublimation (y_{subl}).

compound[a]	P_{irr} / W	t_{irr} / min	extracted with	y_{ini}	y_{subl}
CuF_4Pc[a]	210	2	H_20 (18 h), MeOH (18 h)	7.7 g (71%)	4.6 g (43%)
CuF_8Pc[b]	350	3	H_20 (18 h), MeOH (10 h)	6.0 g (67%)	1.1 g (12%)
$CuF_{16}Pc$[c]	210	4	H_20 (18 h), MeOH (5 h)	6.2 g (58%)	3.7 g (35%)
ZnF_4Pc[d]	210	5	H_20 (18 h), MeOH (5 h)	7.0 g (72%)	4.0 g (41%)
$ZnF_{16}Pc$[e]	350	3	H_20 (18 h), $CHCl_3$ (5 h)	8.7 g (78%)	0.8 g (7%)

[a] CuF_4Pc = 2,2’,2”, 2”’-tetrafluorophthalocyaninato copper(II).

[b] CuF_8Pc = 2,2’,2”,2”’,3,3’,3”,3”’-Octafluorophthalocyaninato copper(II).

[c] $CuF_{16}Pc$ = 1,1’,1”,1”’,2,2’,2”,2”’,3,3’,3”,3”’,4,4’,4”,4”’-hexadecafluorophthalocyaninato copper(II).

[d] ZnF_4Pc = 2,2’,2”, 2”’-tetrafluorophthalocyaninato zinc(II).

[e] $ZnF_{16}Pc$ = 1,1’,1”,1”’,2,2’,2”,2”’,3,3’,3”,3”’,4,4’,4”,4”’-hexadecafluorophthalocyaninato zinc(II).

D.2 J-V Measurements under AM1.5 Illumination

The fill factor is defined as

$$FF = \frac{P_{mpp}}{V_{OC} \cdot I_{SC}} = \frac{P_{mpp}}{V_{OC} \cdot J_{SC} \cdot A} = \frac{V_{mpp} \cdot J_{mpp}}{V_{OC} \cdot J_{SC}} \tag{D.5}$$

with P_{mpp} as the maximum achievable power, the open circuit V_{OC}, the short current I_{SC} and the short current density J_{SC}. The partial derivatives of the single measures are

$$\frac{\partial FF}{\partial V_{mpp}} = \frac{J_{mpp}}{V_{OC} \cdot J_{SC}} \tag{D.6}$$

$$\frac{\partial FF}{\partial J_{mpp}} = \frac{V_{mpp}}{V_{OC} \cdot J_{SC}} \tag{D.7}$$

$$\frac{\partial FF}{\partial V_{OC}} = -\frac{V_{mpp} \cdot J_{mpp}}{{V_{OC}}^2 \cdot J_{SC}} \tag{D.8}$$

$$\frac{\partial FF}{\partial J_{SC}} = -\frac{V_{mpp} \cdot J_{mpp}}{V_{OC} \cdot {J_{SC}}^2} \tag{D.9}$$

The equation for the error propagation of ΔFF results in ±0,49% (1σ) according to

$$\Delta FF = \sqrt{\left(\frac{\partial FF}{\partial V_{mpp}}\Delta V_{mpp}\right)^2 + \left(\frac{\partial FF}{\partial J_{mpp}}\Delta J_{mpp}\right)^2 + \left(\frac{\partial FF}{\partial V_{OC}}\Delta V_{OC}\right)^2 + \left(\frac{\partial FF}{\partial J_{SC}}\Delta J_{SC}\right)^2} \tag{D.10}$$

The deviations Δx have been calculated from the standard deviations of each measured value.

The expression for the efficiency η derives from

$$\eta = \frac{FF \cdot V_{OC} \cdot J_{SC}}{\frac{P_{light}}{A}} = \frac{V_{mpp} \cdot J_{mpp}}{\frac{P_{light}}{A}} = \frac{V_{mpp} \cdot J_{mpp}}{P_0} \tag{D.11}$$

with P_{light} as the power of the incident light and A as the illuminated area, often summarized to P_0, the illumination intensity. The supplier of the lighting source specifies the error to $\Delta P_0 = \pm 1$ mWcm^{-2}. The partial derivatives give the error of η with $\Delta\eta$=±0,032% (1σ) according to

$$\Delta\eta = \sqrt{\left(\frac{\partial\eta}{\partial V_{mpp}} \cdot \Delta V_{mpp}\right)^2 + \left(\frac{\partial\eta}{\partial J_{mpp}} \cdot \Delta J_{mpp}\right)^2 + \left(\frac{\partial\eta}{\partial P_0} \cdot \Delta P_0\right)^2} \tag{D.12}$$

using the relations

$$\frac{\partial\eta}{\partial V_{mpp}} = \frac{J_{mpp}}{E_e} \tag{D.13}$$

$$\frac{\partial\eta}{\partial J_{mpp}} = \frac{V_{mpp}}{E_e} \tag{D.14}$$

$$\frac{\partial\eta}{\partial P_0} = -\frac{V_{mpp} \cdot J_{mpp}}{{P_0}^2}. \tag{D.15}$$

The errors determined for each measured value and those resulting from error propagation are summarized in table D.2.

Table D.2: Mean values and standard variation of various parameters calculated from table D.3 as well as the propagation error for FF and η.

Parameter	MW	Δ s (1σ)	Δ s (2σ)
V_{OC} / mV	543.9	±2.2	±4.4
J_{SC} / mAcm^{-2}	8.68	±0.04	±0.08
V_{mpp} / mV	413.9	±1.0	±2.0
J_{mpp} / mAcm^{-2}	6.69	±0.03	±0.07
FF / %	58.38	±0.07	±0.13
η / %	2.77	±0.01	±0.02
FF (propagation)/ %	-	±0.49	±0.98
η (propagation) / %	-	±0.03	±0.06

D.3 Complex Capacitance

The impedance Z can be written as

$$Z = |Z|\, cos\phi + j\, |Z|\, sin\phi \tag{D.16}$$

with the real ($Z_r = |Z|\, cos\phi$) and imaginary part ($Z_i = |Z|\, sin\phi$). ϕ is the phase. Furthermore, the capacitance is also C(ω) = $\frac{1}{Zj\omega}$, with ω as the angular frequency[1]. Using $Z = Z_r + jZ_i$ gives

$$C(\omega) = \frac{1}{Z_r j\omega - Z_i\omega} = \frac{Z_r j\omega + Z_i\omega}{(Z_r j\omega + Z_i\omega)(Z_r j\omega - Z_i\omega)} \tag{D.17}$$

$$C(\omega) = \frac{Z_r j\omega + Z_i\omega}{(Z_r^2 j^2\omega^2 - Z_i^2\omega^2)} = \frac{Z_r j\omega + Z_i\omega}{-(Z_r^2\omega^2 + Z_i^2\omega^2)} \tag{D.18}$$

$$C(\omega) = -\frac{Z_i\omega}{(Z_r^2\omega^2 + Z_i^2\omega^2)} - j\frac{Z_r\omega}{(Z_r^2\omega^2 + Z_i^2\omega^2)}, \tag{D.19}$$

thus, the real and imaginary capacitance is given by $C_r = -\frac{Z_i\omega}{(Z_r^2\omega^2+Z_i^2\omega^2)}$ and $C_i = -\frac{Z_r\omega}{(Z_r^2\omega^2+Z_i^2\omega^2)}$.

---

[1] $\omega = 2\pi f$

Table D.3: Measurement values for the determination of the uncertainty of the measurements using the solar simulator.

t / min	V_{OC} / mV	J_{SC} / mAcm^{-2}	FF / %	η / %	V_{mpp} / mV	J_{mpp} / mAcm^{-2}
0	544.642	8.683	58.291	2.77	415.108	6.672
2	542.904	8.706	58.364	2.781	413.507	6.725
4	547.652	8.618	58.275	2.76	415.356	6.646
6	546.779	8.707	58.344	2.785	415.168	6.709
8	543.946	8.684	58.378	2.767	414.081	6.682
10	541.965	8.671	58.427	2.763	413.757	6.678
12	541.202	8.744	58.48	2.788	412.895	6.752
14	545.684	8.723	58.389	2.788	414.31	6.73
16	540.741	8.735	58.418	2.78	412.904	6.732
18	545.106	8.638	58.375	2.763	414.295	6.669
20	545.364	8.662	58.367	2.768	414.684	6.675
22	543.355	8.683	58.327	2.766	414.022	6.68
24	544.351	8.627	58.402	2.755	414.377	6.648
26	545.195	8.66	58.395	2.766	414.333	6.675
28	541.597	8.689	58.404	2.771	413.032	6.708
30	546.241	8.692	58.295	2.772	414.407	6.69
32	542.785	8.713	58.4	2.778	413.268	6.722
34	543.233	8.661	58.405	2.764	413.548	6.682
36	540.185	8.659	58.487	2.757	412.14	6.689
38	542.985	8.682	58.583	2.768	412.928	6.704
40	540.963	8.71	58.441	2.771	412.702	6.714
42	544.903	8.676	58.355	2.767	414.68	6.672
44	539.913	8.673	58.426	2.757	411.968	6.692
46	545.962	8.723	58.312	2.788	414.929	6.719
48	543.855	8.717	58.413	2.782	413.125	6.734
50	548.136	8.664	58.275	2.77	415.857	6.661
52	547.41	8.634	58.299	2.764	414.795	6.664
54	544.858	8.681	58.346	2.768	414.478	6.678
56	543.249	8.632	58.393	2.754	413.606	6.659
58	540.89	8.817	58.411	2.801	412.126	6.798
60	544.304	8.623	58.341	2.757	413.756	6.663

Acknowledgements

The realization of this thesis would not have been possible without the contribution of many people. I thank all these persons by mentioning several names hereafter and ask for forgiveness in case I forgot some names.

I want to express my gratitude to all who have supported me with this work. I want to thank my supervisor Prof. Dr. Karl Leo for the possibility to prepare this thesis at the Fraunhofer institution COMEDD in parallel to my other duties. Prof. Dieter Wöhrle is thanked for his willingness to act as additional expert.

Special thanks is directed to my group leader Dr. Olaf Hild for giving me time and financial support for carrying out my experiments as well as acting as critical reviever of this thesis. Particularly worth mentioning is his persuasion for going back to my roots as synthetic chemist in Bremen.

I want to thank all my present and former office colleagues Christiane Trepte, Frank Finger, Lars Ahlrichs, Thomas Weicht, Jörg Arnold, Sebastian Franke, Claudia Keibler, and Falk Schütze for the nice atmosphere, and in particularly André Philipp who conscientously took care of my plants and degrading tea cans. I have always enjoyed the company with you there.

Special thanks to the technicians, in particular to Thomas Mertz and Olaf Willner - although the Bestec machine was sometimes like a moody lady, eventually she always worked in a superior status. I do not want to forget the whole operator team, who took care of the substrate preparation and the encapsulation of all my samples.

Particularly I want to thank the following friends and colleagues for contributing, discussing and carefully checking some parts of this work:

- Sebastian Franke, especially for getting the new Bestec tool running together with me.

- Richard Pfeifer, in particular for his assistance in optical simulations and discussing physical problems.

- Christian Schirrmann, in particular for performing the impedance measurements and assisting with the FTIR set-up.

- Dr. Bolko Schöneich for extracting the optical constants of the organic thin films from my transmission and reflection spectra.
- Johannes Zettler, especially for optical modeling of graded and homogenous absorption layers.
- Dr. Michael Hoffmann for introducing me to the UV/vis photospectrometer and fluorometer.
- Dr. Wolfgang Tress, in particular for fruitful discussions related to the ternary systems and jointly collaboration for publication.
- Dr. Michael Thomschke and Matthias Schober for fruitful discussions about semiconductor physics at the coffee table.
- Dr. James Whitby for his support to deal with plain English.
- my students Simon Kahmann, Daniel Griese, Jasper Westphalen and Lieselotte Ilg who helped me out in busy moments to carefully perform the characterization measurements of the samples. They never hesitated to try any of my challenging ideas. I wish you all the best for your future!
- Christian Rahnfeld, especially for sharing his sweets, DVDs and giving me a ride back home at rainy days.

Finally I want to thank my family for their support during the last years and Christoph for the fact that he is here!

Erklärung

Diese Dissertation wurde an der Fraunhofer Einrichtung für Organik, Materialien und Elektronische Bauelemente Dresden (COMEDD) und an der Fakultät Mathematik und Naturwissenschaften der Technischen Universität Dresden unter wissenschaftlicher Betreuung von Prof. Dr. Karl Leo angefertigt.

Hiermit versichere ich, dass ich die vorliegende Arbeit ohne unzulässige Hilfe Dritter und ohne Benutzung anderer als der angegebenen Hilfsmittel angefertigt habe; die aus fremden Quellen direkt oder indirekt übernommenen Gedanken sind als solche kenntlich gemacht. Die Arbeit wurde bisher weder im Inland noch im Ausland in gleicher oder ähnlicher Form einer anderen Prüfungsbehörde vorgelegt. Weiterhin versichere ich, dass bisher keine Promotionsverfahren stattgefunden haben. Ich erkenne die Promotionsordnung der Fakultät Mathematik und Naturwissenschaften an der Technischen Universität Dresden vom 23.02.2011 an.

Dresden, den 05.09.2013

Beatrice Beyer